# LINEAR MODEL AND DYNAMIC ANALYSIS OF MULTI-TERMINAL DIRECT CURRENT SYSTEMS

**JIAPENG LI**

**PhD**

**The Hong Kong Polytechnic University**

**This programme is jointly offered by The Hong Kong Polytechnic University and Xi'an Jiaotong University**

**2023**

**The Hong Kong Polytechnic University**

**Department of Electrical and Electronic Engineering**

**Xi'an Jiaotong University**

**School of Electrical Engineering**

# Linear Model and Dynamic Analysis of Multi-Terminal Direct Current Systems

**Jiapeng Li**

**A thesis submitted in partial fulfilment of the requirements for the degree of Doctor of Philosophy**

**June 2023**

# CERTIFICATE OF ORIGINALITY

I hereby declare that this thesis is my own work and that, to the best of my knowledge and belief, it reproduces no material previously published or written, nor material that has been accepted for the award of any other degree or diploma, except where due acknowledgement has been made in the text.

_____(Signed)

LI Jiapeng (Name of student)

# ABSTRACT

Multi-terminal direct current (MTDC) systems maximise the economic and flexible advantages of DC transmission, thereby showing broad application prospects in high renewables penetrated power systems. Nevertheless, the dynamic properties of MTDC systems are rather complicated. Under severe DC faults, the DC network may experience intense current surges, which may damage the vulnerable converters. Under small disturbances, the DC-link current may oscillate divergently with poor control parameters, which may cause the converter to block and even disrupt the power transmission. Consequently, it is essential to study the dynamic characteristics for ensuring the safe and stable operation of MTDC systems. This thesis mainly focuses on the DC-side dynamic behaviours of MTDC systems, including the converter modelling, fault analysis, and stability analysis of MTDC systems, stated as follows.

1. Reduced linear models of the line-commutated converter (LCC) and voltage source converter (VSC) with control effects are established, respectively. As per the DC-link voltage deviation, the least squares approximation or small-signal analysis is utilised to derive the linear models of different converters. It is indicated that converters can be equivalent to simple RLC circuits for dynamic analysis from the DC side.

2. An analytical DC fault calculation method for generic MTDC systems is proposed. Combining the derived converter models with the network model and eliminating the operating variables, the state-space equation of the fault network is obtained. Accordingly, the mathematical expression of the short-circuit current of the entire network can be derived.

3. A simple DC fault calculation method of VSC-MTDC systems is proposed based on the high-frequency equivalent (HFE) model. In this model, the low-frequency components in the Laplace fault component network are omitted for the initial fault analysis. Accordingly, an analytical expression of fault current of the whole network is derived. It is unveiled that in the initial fault stage, the short-circuit current of the fault line increases approximately linearly, while that of other lines increases approximately cubically.

4. The DC-side instability mechanism is explored by investigating the small-signal stability of two-terminal DC links. The DC-side damping properties of various converters are first studied based on the system characteristic functions. For facilitating stability analysis, the original model can be reduced by retaining the dynamic characteristics in the vicinity of the dominant frequency, which is called dominant frequency analysis (DFA). Based on DFA, an analytical DC-side stabilising condition of the point-to-point VSC-HVDC link is derived.

5. Analytical DC-side stabilising conditions of MTDC systems are derived. The frequency domain model of a generic MTDC system is established. By using DFA, the analytical expressions of the system damping under each dominant frequency can be obtained. It is found that when the positive damping generated from constant-power-controlled rectifier(s), constant-DC-voltage-controlled converter(s), and transmission resistance cannot compensate for the negative damping introduced by constant-power-controlled inverter(s), divergent oscillation will appear in the DC network.

**KEY WORDS**: Multi-terminal direct current system; Converter modelling; Fault calculation; Stability analysis

**TYPE OF DISSERTATION**: Theoretical Research

# ACKNOWLEDGEMENT

It is my great pleasure and honour to express my heartfelt appreciation to my supervisors, Prof. Zhao Xu and Prof. Guobing Song. Prof. Xu impressed me with his broad knowledge base and strong interest in research. His creative thinking always stimulates me, and his dedication and optimism encourage me to overcome difficulties. Every conversation with him is memorable, and I will never forget his help in revising my thesis late at night. His help and encouragement enabled me to broaden my research direction and keep exploring. Prof. Song is a constant source of inspiration for me, with his curiosity and exploration spirit toward the essence of problems. He generously shares his knowledge and experience with me, and his unique and profound insights always enlighten me. I am deeply grateful for his patience and tolerance throughout my postgraduate study. His guidance, support, and encouragement enabled me to pursue my research in depth continuously.

I would also like to express my sincere gratitude to Prof. Yujun Li for his support and help during my Ph.D. study. He infects me with his passion for academic research and his critical thinking spirit. He can always capture the key issues and propose brand-new ideas. Every discussion with him is exciting and stimulating. He generously shares with me his insights on research as well as work and life, which gives me lifelong benefits. In addition, I would like to thank Prof. Minghao Wang, Prof. Zhongxue Chang, and Prof. Chenhao Zhang, as well as every partner in the research groups, for the time we worked hard and played together, for their kind consideration and support to me.

I owe a special debt of gratitude to my parents Mr. Weinan Li, and Mrs. Dongli Li, who have given me the most selfless and unconditional love since I was born. Their care and love warm my life and encourage me to keep moving on. I want to also give my special thanks to my girlfriend, Dr. Jiajie Song. We have encouraged each other through difficult times, shared the joy of life, and witnessed many happy moments together. Her tolerance, understanding, trust, support, and companionship make me a better man.

Last but not least, I would like to thank Prof. Zhengchun Du, Prof. Xiaoning Kang, and others who gave valuable comments and assistants on my thesis. I would also like to thank The Hong Kong Polytechnic University and Xi'an Jiaotong University for the scholarship and stipend support, which enabled me to focus on completing my Ph.D. study.

# CONTENTS

# 1 Introduction

## 1.1 Background and Significance

Exploring and utilising renewable energy sources, such as wind and photovoltaic power, is a critical approach to dealing with the energy and environmental issues [1]. Since wind and solar energy resources are often inversely distributed with load centres [2], long-distance, large-capacity high-voltage transmission is required to achieve large-scale intensive development of renewables [3]. Direct current (DC) transmission has a larger transmission capacity, lower loss, higher control flexibility, and better economy in long-distance, large-capacity transmission scenarios than its alternative current(AC) counterpart [4]. Therefore, DC transmission is regarded as a preferred choice for integrating renewable sources [5].

Currently, the line-commutated-converter-based (LCC-based) high-voltage DC (HVDC) transmission technique has matured and has become the mainstream scheme for large-capacity long-distance DC transmission [6], [7]. However, several inherent drawbacks impede its further development. Firstly, the LCC cannot establish AC voltage independently, and thus synchronous generators (SGs) are required at the sending-end AC grid [8]. Secondly, there is a high commutation failure risk if severe faults occur at the receiving-end AC grid, resulting in transmission interruption [9], [10]. Thirdly, LCC-HVDC transmission requires large-sized reactive power compensation devices and complex filters, which increases the difficulty in site selection with the large area occupied [11].

On the basis of the full-controllable electric semiconductor device and pulse width modulation, the voltage-source-converter-based (VSC-based) HVDC revolutionised the power industry [12], [13]. Despite the higher cost, the VSC outperforms the LCC for its independent voltage buildup capability[14], fast and decoupled active and reactive power modulation [15], and elimination of commutation failure [16], and enhancement in the stability and flexibility of the power grid.

Recently, developing the multi-terminal DC (MTDC) network has gathered extensive attention [17]. Compared with AC interconnection, DC interconnection has many prominent advantages, stated as follows. Since renewable sources can directly integrate into the grid through DC boost converters, power delivery via the DC network can enhance the utilisation efficiency of renewable energy [18]. In addition, DC interconnection gets rid of the power-angle stability and frequency stability issues [19]. Moreover, the mutual supply of several AC

systems can be achieved via DC interconnection due to its fast and flexible power regulation capability [20]. At present, MTDC systems fall into two categories: the VSC-MTDC system [21] and the hybrid MTDC system containing both LCC(s) and VSC(s) [22]. MTDC systems maximise the economic and flexible advantages of DC transmission with multi-point power supply and reception, which have wide applications in the future high renewables penetrated power system, e.g. offshore wind energy integration [23], asynchronous interconnection of multi-region AC grids [24], as illustrated by Fig. 1-1.

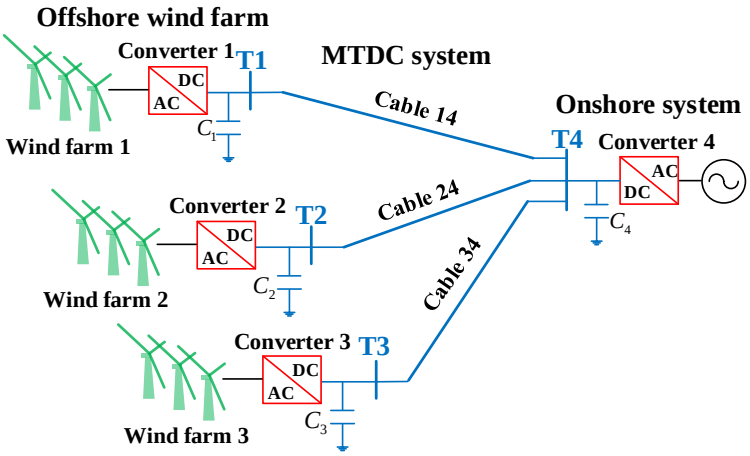


**(a) Offshore wind farm integration**

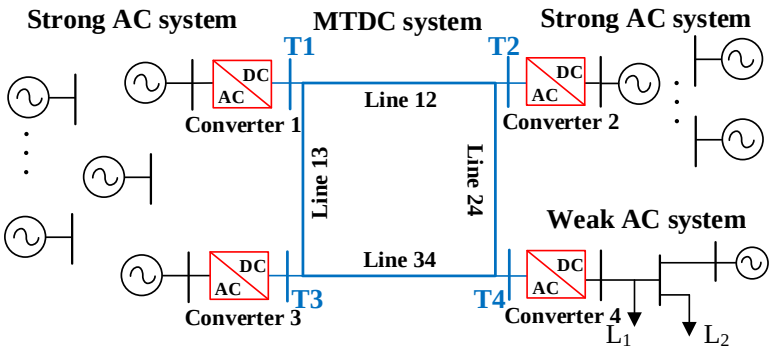


**(b) Asynchronous interconnection of multi-region AC grids**

Fig. 1-1 Applications of MTDC systems.

Converter control has significant impacts on the dynamic process of MTDC systems. Since multiple converters with different control modes are coupled via the DC network, the dynamic behaviour of MTDC systems is rather complicated [25]. On the one hand, once a DC short-circuit fault occurs, the ground capacitors of VSCs discharge to the fault point, which leads to a DC-link current surge in the DC line and brings huge impacts to the system [26]. To avoid the fault overcurrent damaging the vulnerable power electronic switches, the fault line should be cut off accurately within a few milliseconds after the fault. Otherwise, the converter will be blocked, and the power transfer in the MTDC system must be interrupted [27]. On the

other hand, during normal operation, converter control may amplify the resonance between the inductance and capacitance components in the DC network, leading to oscillations of the DC-link voltage and current [28]. In many DC transmission systems projects, oscillation instability risks have appeared under certain operating conditions with poor control parameters. For example, the Xiamen ±320 kV VSC-HVDC transmission project exhibited DC-link current oscillations of 23.6 Hz and 25.2 Hz under the single-pole sending mode with the transfer power of 100 MW and 500 MW, individually [29]. Oscillations in DC-side electrical quantities may trigger the alarm of monitoring equipment or even cause converter shutdown.

The short-circuit current calculation of MTDC systems can guide the typing of protection equipment, such as circuit breakers, limiting reactors, and the design of protection schemes. In addition, based on the stability analysis of MTDC systems, the mathematical relationship between control parameters and system stability can be built up, which provides essential guidance for the control parameter tuning and stabilisation control design. Therefore, the dynamic analysis is of significant for the safe and stable operation of MTDC systems.

## 1.2 Literature Review

A generic dynamic system can be expressed by differential-algebraic equations (DAEs), and its dynamic process can be obtained by solving the DAEs with the initial condition. Investigation of the dynamic properties under fault and normal conditions is the foundation for controlling the dynamic system. Existing works mainly study the dynamic properties of MTDC systems from their modelling, fault current calculation, and stability.

### 1.2.1 Modelling of MTDC Systems

The mathematical model of MTDC systems is the foundation of dynamic analysis. MTDC systems mainly consist of converters, DC transmission lines, filters, and so on, among which converters are the most critical components in MTDC systems. So far, there are three types of converters commonly used in MTDC systems, namely, the LCC, the two-level VSC (TLVSC), and the modular multilevel converter (MMC).

To accurately represent the converters' dynamic behaviours, many researchers have made great efforts on the switching model of various converters. The circuit and control systems of the converter are described by a series of DAEs, and the dynamic responses are obtained by solving the DAEs with some numerical integration methods. The switching model mainly orients to the electromagnetic transient program (EMTP), and existing works focus on

enhancing the calculation accuracy with a reduced computational burden. In [30], a co-simulation method based on multi-rate and mixed solver is proposed to boost the simulation efficiency of LCC-HVDC systems. Using the switch-state representation, a fast electromagnetic transient simulation model of VSC with different topologies is proposed in [31]. Without the iterative computation to determine the feasible switch-state combination, the proposed model can significantly enhance the simulation efficiency. In [32], the TLVSC with different PWM techniques is established in the extended harmonic domain, which can represent the harmonic interactions in the converter. The electromechanical transient model of the MMC is reported in [33], which takes the effects of the inner and outer controllers, and the modulation strategies into account. In [34], the valves in each arm of the MMC are equivalent to interpolation-enabled IGBT and diodes to enable the transient simulation after converter blocking. Despite the high accuracy, the switching model can only generate the dynamic response curves under studied scenarios rather than the general rules of the dynamic behaviours of converters.

For the convenience of analysis, the average value model is proposed, which neglects the switching processes of valves and only reflects the low-frequency dynamics of the converter. In [35], the TLVSC is equivalent to a grounded capacitor to calculate the short-circuit current after several milliseconds after DC faults. In [36], a resistor, inductor, and capacitor (RLC) series circuit model is proposed to study the dynamic responses of the MMC under DC faults. On the basis of the RLC model, the analytical expression of fault current can be easily derived. However, the RLC model omits the control dynamics of the converter, which may result in relatively large errors in the dynamic analysis.

To address this issue, the small-signal analysis is adopted to derive the linear converter model considering the control effects. In [37], the circuit and control equations of LCC are linearized around the equilibrium, and an LCC is expressed by 21-order differential equations for the small-signal analysis of LCC-HVDC systems. On the basis of the concept of the motion equation, a small-signal model of LCC is proposed in [38] to reflect the external properties of the LCC. Similarly, a DC-side equivalent impedance model of the TLVSC is proposed in [39], which considers the inner and outer loops of the VSC vector control. In [40], a small-signal model of the MMC is proposed, and the balanced realization theory is used to reduce the order of the converter model. To investigate the harmonic dynamics of converters, the harmonic state space and the dynamic phasor are utilised in the modelling. On the basis of the dynamic phasor theory, an average-value model of the LCC is proposed in [41], which can represent

the low-frequency dynamics of the LCC with a low computational burden. In [42], the harmonically coupled impedance matrix is used to represent the dynamic behaviours of the TLVSC at the harmonic frequencies, which lays a foundation for the harmonic analysis of the converter-embedded power systems. In [43], the harmonic state-space representation of the MMC is derived, which can reflect the internal harmonic dynamics of the converter. A modified average value model of the MMC is reported in [44], which not only increases the accuracy in evaluating the power loss but also enables the dynamic response calculation after the converter blocking. Due to the complexity of the control system of converters, the order of the small-signal converter model is relatively high, which may hinder the analytical solution of the dynamic responses of the converter.

To sum up, the switching model can hardly render the general rules of the dynamic properties of converters, while existing average-value-based models with the consideration of control effects are relatively complex such that the order of the entire MTDC system can be rather high. Consequently, it is urgent to derive simplified converter models for the analytical dynamic analysis of MTDC systems.

### 1.2.2 Fault Calculation of MTDC Systems

Fault current calculation is the foundation of power device typing and protection scheme designing. Transient simulation is widely used to determine the short-circuit current level in a faulted MTDC system. The DAEs of the studied system are first formulated. Then, the time-domain responses of the system are calculated by solving the DAEs numerically. The transient simulation model of a back-to-back LCC-HVDC system is established in [45], and the dynamics of the short-circuit current in the HVDC link under various fault scenarios can be obtained. In [46], a two-terminal TLVSC-HVDC link is established based on Matlab/Simulation, and the system responses under DC faults can be obtained. To enhance the simulation efficiency, the average value model of TLVSCs under different control modes is used in [47], and the transient model of the DC microgrid is proposed for DC fault analysis. Similarly, the fault characteristics of the multi-infeed AC/DC modernized microgrid are investigated in [48], where the balancing equation of the VSC is linearized, and the TLVSC is described by the state-phasor representation. In [49], Thevenin's theorem is adopted to derive the DC-side impedance model of the TLVSC. By neglecting the switching process of the converter, the dynamics of the DC fault current can be fast obtained via numerical simulation. In [50], the transient simulation model of the MMC-MTDC system is built to determine the system responses under DC faults. However, it could be rather time-consuming due to the

large number of sub-modules (SMs) of the MMC. To address that, the average value model of the MMC is adopted in [51], and the companion-circuit-based model of the MMC-MTDC system is proposed. In [52], the fault characteristics of the MMC-MTDC system are investigated based on the companion circuirt method, which significantly enhances the efficiency of the transient simulation. Apart from the high accuracy, the fault current calculation based on transient simulation is compatible with various converters. In [53], the transient model of the China Wudongde HVDC project, a hybrid LCC-MMC three-terminal DC system, is established to study its dynamic properties. The transient simulation model of the same project is also reported in [54], which has been verified via the on-site experiment. To reduce the computational complexity of the electromagnetic transient simulation, the average models of the LCC and the MMC are utilised to form the dynamic-phasor-based model of the hybrid LCC-MMC system [55], which accurately reflect the low-frequency behaviours of the system. Despite the high accuracy, the transient simulation cannot render the general fault properties of the studied system.

Recently, researchers have resolved the RLC circuit analysis to deduce the analytical expression of the fault current. In [56], the TLVSC is represented by a grounded DC-link capacitor for the DC fault analysis, and the discharging power of the capacitor is assessed. The analytical expression of the initial travelling wave in the MMC-HVDC link under pole-to-ground DC faults is deduced in [57] based on Perterson's law in the modal domain. In [58], the mathematical expression of the fault current considering all refractions and reflections of the travelling wave is proposed, which is rather complicated due to the complexity of the travelling wave propagation process. Since the travelling wave process can induce oscillations in the DC-link voltage and current, the fault calculation results on the basis of the lumped parameter line model can represent the average behaviours of those with the distributed parameter line model. For the simplicity of analysis, the travelling wave process is usually overlooked in most works on the analytical fault calculation of MTDC systems. In [59], the fault characteristics of the DC distribution network containing different TLVSC-integrated distributed generators are investigated. Based on the RLC circuit analysis, the closed-form mathematical expressions of the short-circuit current during the three fault stages are deduced. Analogously, the decoupled equivalent circuit of each distributed generator is established, and the short-circuit current flowing through each branch can be obtained by solving each RLC circuit separately [60]. However, these two works can only apply to DC distribution networks with one common DC bus rather than generic MTDC systems with arbitrary topology. An

analytical fault current calculation method of the symmetrical monopole MMC-HVDC link under pole-to-ground faults is proposed in [61]. The frequency-domain expression of the fault current is first deduced, and its time-domain expression is then obtained via the inverse Laplace transformation. It is found that the fault current in a two-terminal MMC-HVDC link can be regarded as a linear combination of four oscillation modes. Although the RLC circuit analysis can provide a clear expression of the fault current, the expression is usually based on specified network topology and neglects the control effects of converters.

To address the demerits of the RLC circuit analysis method, the state space method is adopted for the more general and accurate fault calculation of MTDC systems. The dynamic phasor model of the LCC-MMC HVDC link is proposed in [62], and the system dynamics under asymmetrical faults and commutation failure are obtained by solving the state-space equations. In [63], the half-bridge MMC is equivalent to an RLC series circuit, and the state-space equations of the three-terminal MMC-HVDC system incorporating a pole-to-pole fault are formulated. In [64], the common and differential mode networks of the DC grid are proposed to study the fault characteristics of the monopolar MMC-MTDC system. In [65], the control effects of MMCs are described by algebraic equations, which implies the dynamic process of MMCs is neglected. Subsequently, the state-space equations of the MMC-MTDC system are linearized so that the superposition principle can be used to facilitate the calculation. The state-space model of the MMC-MTDC system considering the control effects is reported in [66]. However, the proposed model only takes into the relatively slower outer loop of VSCs, while the fast inner loop is overlooked. So far, the state-space-based fault calculation of MTDC systems has not considered different converters with various control modes.

In short, the fault analysis of MTDC systems mainly relies on numerical simulation. Although the analytical expression of the short-circuit of MTDC systems can be derived based on RLC circuit analysis and state space method, existing works concentrate on specified network topology or converter control modes. It is necessary to investigate universal fault calculation methods for generic MTDC systems with arbitrary topology and various converters under different control modes.

### 1.2.3 Stability Analysis of MTDC Systems

Stability is a necessary condition of the operation of the MTDC system. The stability of the studied system can be determined by conducting the transient simulation. In [67], the transient simulation model of the VSC-HVDC system is formulated for the stability assessment, which adopts the average value model of the TLVSC and the hybrid simulation

technique to increase the calculation speed. However, stability analysis based on transient simulation can only offer judgment under certain selected scenarios. Consequently, researchers have explored direct stability analysis methods without solving the time-domain responses of the studied system.

Modal analysis is a classic methods to determine the small-signal stability of a dynamic system. The small-signal model of the LCC-HVDC link is formulated in [68]. According to modal analysis, it is found that the instability is mainly caused by the inappropriate parameters of the phase-locked loop (PLL). The small-signal model of the AC-MTDC system is built in [69], and the system damping is enhanced by modulating the active power of VSCs. The small-signal stability of the MTDC system connecting several asynchronous AC systems is studied in [70]. The impacts of the inertia and the primary frequency control on the system stability are revealed on the basis of modal analysis. [71] investigates the influences of the interactions of VSCs on the stability of the AC-MTDC system, which is proven to degrade the small-signal stability. [72] reveals that the instability risks of the AC-MTDC system can be increased when the open-loop modes of the AC and DC networks are close in the complex plane. Based on modal analysis, it is found that the power-voltage droop gain of VSCs significantly influences on the small-signal stability of the VSC-MTDC system [73]. A selection criterion of the droop gain is further proposed for ensuring stability. Similarly, the stability of the VSC-MTDC system is investigated in [74] under converter outage events. Based on the trajectory sensitivity analysis, a stability-constrained model is proposed to achieve automatic power-sharing while guaranteeing system stability. [75] points out system the interactions of the droop control dynamics and the converter-tied AC grid with weak strength may degrade the stability of the VSC-MTDC system. [76] further reveals that the negative damping generated from the $q$-$q$ channel of the PLL can lead to oscillatory instability at the AC side. The above works mainly explore the influence of the DC system integration on the stability of the AC system. Actually, the interactions of the converters and the inductance and capacitance components in the DC network may also result in small-signal instability, which is called DC-side stability and is the focus of this thesis.

In [77], the small-signal model of the VSC-MTDC system connecting to asynchronous AC systems is established. On the basis of modal analysis, it is revealed that some oscillation modes with a small damping ratio are merely associated with the DC-link electrical quantities. By calculating the participation factors, it is unveiled in [78] that the interactions between VSCs in an MTDC system are closely related to the dynamics of the DC-link voltage. In [79],

the small-signal model of the MMC-HVDC system is formulated. It is indicated that the inner dynamics of the MMC could cause instability if the parameters of the circulating current suppression control are inappropriate. This stability issue is referred to as harmonic stability. In [80], it is assumed that the harmonics are effectively restrained by the inner control of MMCs. The contribution of each MMC on the DC-side stability is assessed based on participation factor analysis. The inequality constraints of the MMC-MTDC system are derived in [81], where the second-order Taylor expansion is applied to the eigenvalues to determine the maximum value of the droop gain of each MMC for ensuring stability. Although the modal analysis can accurately determine the system stability, it relies on numerical calculations to obtain the eigenvalues of the system. As a result, analytical expressions bridging the relationship between system stability and parameters of physical and control systems cannot be derived.

To provide more physical interpretations of the instability mechanism, the impedance-based method focusing on the external behaviours of the subsystems is widely used in the small-signal stability analysis of converter-embedded systems. In [82], the AC-side impedance of the LCC is derived so that the interactions between the LCC, the wind farm, and the weak AC grid can be evaluated. The impedance-based method can provide an accurate phase margin of the doubly fed induction generator (DFIG) integrated system via the LCC-HVDC link. In [83], the AC-side impedance of the TLVSC is deduced to evaluate the impacts of the converter on the AC system stability. In contrast, the DC-side impedance of the TLVSC is formed in [84] to investigate the DC-side stability of the two-terminal VSC-HVDC link. In [85], the modularized model of the TLVSC is built. Based on the analysis in the frequency domain, it is found that the constant power load (CPL) can bring about negative damping to the low-voltage MTDC system. The separating point of source subsystem and load subsystem in a point-to-point VSC-HVDC link is discussed in [86], and the contribution of each VSC on the DC-side stability is assessed. On the basis of the impedance-based method, it is unveiled in [87] that the nonpassive behaviour coinciding with the DC network resonance is the reason for the DC-side instability. In [88], the DC-side impedance of the MMC is derived, and it is indicated that the interactions between the MMC and the DC network may induce high-frequency resonance. [89] reveals that the increase in the proportional gain of the constant voltage control of the MMC may degrade the stability performance, yet the feasible range of the proportional gain is not determined. By using the general Nyquist criterion, the harmonic stability of the VSC-MTDC system is studied in [90]. The impedance-based method can be

conducted via online measurement. Unfortunately, the order of the subsystems can be relatively high such that the analytical stability criterion is absent.

Passivity analysis is another popular method for stability analysis and control. In [91], the control parameters of the grid-connected VSC are tuned to make sure the converter itself is passive under arbitrary frequency. From the passivity aspect, it is unveiled in [92] that the negative equivalent conductance of VSCs will amplify the DC-side resonance. The passivity analysis requires that the energy is non-decreasing under any frequency. Consequently, it cannot render an analytical relationship between system parameters and the stability boundary. In contrast, the damping torque analysis only concentrates on the system behaviours near the dominant oscillation frequency. The DC-side stability of a radial MTDC system containing one source subsystem and one load subsystem connecting with the same common DC bus is explored in [93]. With this specified network topology, the analytical expression of the damping ratio of the DC-side oscillation mode can be obtained. It is assumed in [94] that all VSCs in the MTDC system are identical. Nearby the dominant frequency, the characteristic function of the VSC-MTDC system is reduced to a second-order function. Similarly, [95] also assumes that all VSCs in the VSC-MTDC system are the same, which is certainly unrealistic. By using damping analysis, it is found that there is only one dominant frequency in the master-slave MTDC system, while multiple dominant frequencies may appear in the droop-based MTDC system [96]. The current flow controllers are incorporated into the DC-side stability model of the VSC-MTDC system in [97], and a parameter tuning method for ensuring the DC-side stability is proposed. The assumption of identical VSCs is first removed in [98]. The definition of the VSC differences is first put forward, whose influences on the DC-side stability of the VSC-MTDC system are then evaluated based on the damping torque. In [99], the properties of the DC-link voltage oscillation mode are investigated based on damping torque analysis and modal analysis. Damping torque analysis can reduce the order of the studied system such that analytical stability conditions can be obtained. However, the existing works assume that the natural oscillation mode is induced by the inner and outer loops of the converter. Actually, the DC-side oscillations are usually caused by the resonance between the inductance and capacitance components in the DC network, provided that the DC-link voltage control is well-tuned, which cannot be reflected in the existing studies based on damping torque analysis.

In conclusion, existing works on the stability of MTDC systems fail to provide clear mathematical relationships between the stability boundary and parameters of physical and

control systems. There is a need for analytical stabilising conditions to reveal the DC-side instability mechanism of MTDC systems.

## 1.3 Primary Contributions

1. Existing converter models for DC fault analysis usually neglect the control effects, while those for stability analysis are relatively complicated. Focusing on the DC-side dynamic behaviours of converters, the reduced linear models of various converters considering the control effects are derived for the fault and stability analysis in this thesis. According to the DC-link voltage derivations of the converter, the small-signal analysis and the least squares approximation are utilised to deduce the linear model of the LCC, TLVSC, and MMC. It is indicated that the LCC, TLVSC, and MMC can be equivalent to simple RLC circuits from the DC side. The derived converters models consider the control effects with relatively low computational complexity, which lay foundation for the dynamic analysis of MTDC systems.

2. Existing state-space-based fault calculation methods can only apply to MTDC systems containing a single type of converter with a fixed control mode. This thesis proposes a state-space-based fault calculation method for generic MTDC systems. Using the superposition principle, the state-space equation of the fault component network is derived so that the analytical expression of the fault current in the whole network is obtained by solving the initial value problem of ordinary differential equations. The proposed method can not only deal with converters with different topologies and control modes but also achieves higher accuracy than existing state-space-based fault analysis methods.

3. To deduce concise expressions of the fault current in VSC-MTDC systems, a high-frequency equivalent (HFE) model is put forward in this thesis. Since the high-frequency electrical quantities dominate in the Laplace circuit within the first milliseconds after faults, the low-frequency components are neglected for the initial fault calculation of VSC-MTDC systems. According to the HFE model, analytical time-domain expressions of the fault current of the entire network are derived, indicating that the fault component current of the fault line grows linearly, while that of the healthy line rises cubically within several milliseconds after the DC fault. Compared with the existing method, the proposed one can achieve a more straightforward DC fault analysis with simple calculations and little loss of accuracy.

4. Existing methods based on eigenvalue calculation or Nyquist plot only provide numerical results rather than the general rules of the small-signal stability. This thesis investigates the DC-side damping properties of various converters to develop insight into the

DC-side instability in MTDC systems. Focusing on the dynamic behaviours nearby the dominant oscillation frequency, which is referred to as dominant frequency analysis (DFA), the impacts of control parameters on the DC-side damping of the converter can be evaluated via simple and direct calculation. Based on DFA, the DC-side stability of the two-terminal VSC-HVDC link is studied, which reveals the instability mechanism of the DC link under joint actions of different VSCs.

5. This thesis proposes a DC-side stability analysis method for generic MTDC systems based on DFA. The frequency domain model of generic MTDC systems is established. Using DFA, the analytical stabilising condition of the MTDC system is derived, which reveals that DC-side instability appears once the positive damping of the CPC-based rectifier, the CDVC-based inverter, and the transmission resistance cannot compensate for the negative damping of the CPC-based inverter. Compared with existing stability analysis methods, the proposed one can provide concise and analytical relationships between the stability boundary and parameters of physical and control systems.

## 1.4 Thesis Layout

The rest of the thesis is composed of six chapters. Chapter 2 derives the DC-side equivalent model of the LCC, the TLVSC, and the MMC considering the control effects. Chapter 3 proposes a universal and efficient fault calculation method for generic MTDC systems with arbitrary network topology and various converters. Chapter 4 proposes a simple fault calculation method for VSC-MTDC systems based on the HFE. Chapter 5 investigates the DC-side damping properties of various converters and the joint influences of different converters on the system damping. Chapter 6 proposes a DC-side stability analysis method for generic MTDC systems based on DFA. Chapter 7 summarizes this thesis and clarifies future work.

## 1.5 List of Publications

[1] Li JP, Li YJ, Xiong LS, et al. DC fault analysis and transient average current based fault detection for radial MTDC system[J]. IEEE Transactions on Power Delivery, 2020, 35(3): 1310~1320 (SCI: 000537949900024; EI: 20202208765941).

[2] Li JP, Song GB, Yan JF, et al. Data-driven fault detection and classification for MTDC systems by integrating HCTSA and softmax regression[J]. IEEE Transactions on Power Delivery, 2022, 37(2): 893~904 (SCI: 000772463500025; EI: 20211710258172).

[3] Li JP, Li YJ, Zhang Xu, et al. Design-oriented DC-side stability analysis of VSC-HVDC systems based

on dominant frequency analysis[J]. International Journal of Electrical Power & Energy Systems, 2023, 149(109060): 1~10 (SCI: 000949485400001; EI: 20231013679305).

[4] Li JP, Li YJ, Wang MH, et al. DC fault detection in hybrid MTDC systems using transient average of DC reactor voltage[J]. International Journal of Electrical Power & Energy Systems, 2023, 150(109093): 1~10 (SCI: 000971354000001; EI: 20231213750876).

[5] Li JP, Li YJ, Zhang Xu, et al. Fault analysis of converter interfaced generator embedded power system considering control mode switching[J]. IET Generation Transmission & Distribution, 2023, 17(7): 1525~1537 (SCI: 000928514800001; EI: 20230613561809).

[6] Li JP, Li YJ, Du ZC, et al. Damping turning rule of virtual synchronous generator for global stability[J]. IEEE Transactions on Power Delivery, doi: 10.1109/TPWRD.2023.3250769 (EI: 20231013687472).

[7] Li JP, Li YJ, Wang MH, et al. Analytical DC-side stabilizing conditions for hybrid HVDC links based on dominant frequency model reduction[J]. Energy Reports, 2023, 9: 806~818 (EI: 20231713947910).

[8] Li JP, Li YJ, Yuan XT, et al. DC fault analysis and detection for offshore wind farms integration via MTDC[J]. Electric Power Automation Equipment, 2020, 40(12): 119~128 (EI: 20205209681841, in Chinese).

[9] Li YJ, Li JP, Xiong LS, et al. DC fault detection in meshed MTDC systems based on transient average value of current[J]. IEEE Transactions on Industrial Electronics, 2020, 67(3): 1932~1943 (SCI: 000498553200026; EI: 20194607671450).

[10] Li YJ, Li JP, Wu GH, et al. DC fault analysis models of three converter topologies considering control effects[J]. IEEE Transactions on Industrial Electronics, 2020, 67(11): 9480-9491 (SCI: 000552206000042; EI: 20203309041553).

[11] Li YJ, Li JP, Xiao HQ, et al. Stability analysis of droop-based converter using SISO method from DC side perturbation[J]. IEEE Transactions on Power Delivery, 2021, 36(5): 3150~3161 (SCI: 000698898900061; EI: 20214010966129).

[12] Li YJ, Wu L, Li JP, et al. DC fault detection in MTDC systems based on transient high-frequency of current[J]. IEEE Transactions on Power Delivery, 2019, 34(3): 950~962 (SCI: 000469337200017; EI: 20184906208111).

[13] Li YJ, Yuan XT, Li JP, et al. Novel grid-forming control of PMSG based wind turbine for integrating weak AC grid without sacrificing MPPT[J]. IET Generation Transmission & Distribution, 2021, 15(10): 1613-1625 (SCI: 000619980000001; EI: 20210809945471).

[14] Li JP, Li YJ, Xiong LS, et al. DC fault analysis and transient average current based fault detection for radial MTDC system[C]. 2021 IEEE Power & Energy Society General Meeting (PESGM 2021), Washington DC, USA, Jul. 2021 (SCI: 000821942400362).

[15] Li Y, Li JP, Cao RB, et al. Non-unit protection algorithm for MTDC systems based on transient variance of current[C]. 31st Australasian Universities Power Engineering Conference (AUPEC 2021), Curtin, Australia, Sep. 2022 (SCI: 000848257500015; EI: 20220411524795).

[16] Yang YN, Li JP, Li YJ. Damping torque analysis of a power system integrated with PMSG-based wind farm for low-frequency oscillation mitigation[C]. 2022 IEEE International Conference on Power

Systems and Electrical Technology (PSET 2022), Aalborg, Denmark, Oct. 2022 (EI: 20231914062056).

[17] Liu YH, Li JP, Xu Z, et al. A distributed architecture and virtual synchronous machine control of onboard charger for the electric vehicle[C]. The 9th International Conference on Power Electronics Systems and Applications (PESA 2022), Hong Kong, Sep. 2022 (SCI: 000972202300036; EI: 20231013661302).

[18] Tang Z, Hao LH, Li JP, et al. Power system inertia estimation based on long short term memory network[C]. 2021 IEEE Sustainable Power and Energy Conference (iSPEC 2021), Nanjing, China, Dec. 2021 (EI: 20221611967474).

# 2 DC-Side Equivalent Models of Different Types of Converters for Dynamic Analysis

## 2.1 Introduction

Power electronic converters are the key devices in MTDC systems, which interconnect the AC and DC grids. Born in the 1960s, the line-commutated converter (LCC) has been widely used in HVDC projects because of its low cost and large capacity [6]. However, the LCC demands relatively large reactive power compensation and is unable to supply weak AC systems. Most seriously, there are high risks of commutation failure when the voltage of the point of common coupling (PCC) of the LCC-based inverter dips [9]. In recent decades, voltage-source converters (VSCs) have developed rapidly, especially with the emerging of the modular multilevel converter (MMC). Due to the use of full-controlled switching devices, e.g., the gate turn-off (GTO) thyristor or the insulated gate bipolar transistor (IGBT), the VSCs distinguish themselves with needless of AC system supports, commutation failure elimination, and decoupling control of active and reactive power [13]. Compared with the classic two-level VSC (TLVSC), the MMC has many series-connected submodules (SMs) in each arm. This enhances the reliability of MMC-based converters and significantly reduces the switching frequency, as each SM can switch on or off independently. Establishing the mathematical models of these three types of converters is the most fundamental step for the dynamic analysis of MTDC systems.

The electromagnetic transient program (EMTP) is one of the most common tools to obtain the dynamic process of power electronic converters. The converter is first formulated by a series of differential-algebraic equations (DAEs). Then, the EMTP calculates the time response of the converter via numerical integration. The detailed switching models of the LCC, TLVSC, and MMC are reported in [30], [31], [33]. Despite the high accuracy, the EMTP-based simulation is timing confusing, especially for large-scale MTDC systems with several converters. Furthermore, it only provides information for selected scenarios rather than the general rule of dynamic responses.

For the convenience of analysis, great efforts have been paid on deriving the reduced mathematical converter models. It is reported in [35] that the TLVSC is reduced as a parallel-connected DC-link capacitor during the capacitor discharging stage of DC fault. Similarly, the MMC is simplified to an RLC series circuit for the initial fault analysis in [36]. Although these

models significantly simplify the fault analysis, the effects of the controllers of the converter are omitted. The DC-side impedance model of the TLVSC considering control effects is proposed in [39]. The average value model of the MMC is derived in [44], which neglects the switching process and reflects only the average terminal behaviour of the converter in a relatively long timescale. However, the complexity and the computational burden of the model increase with the consideration of various control loops. Moreover, the nonlinearity of the converter model can hinder the analytical analysis of the dynamics of MTDC systems.

For one thing, some of the converter models overlook the dynamics of controllers, which may introduce significant errors in the solution of the converter dynamics. For another, the existing converters models considering control effects usually have relatively high complexity, which may not be convenient for the analysis of large MTDC systems. This chapter derives the linear models of the LCC, TLVSC, and MMC, with the consideration of control effects. Based on the change of the DC-link terminal voltage of the converter, the least squares approximation and the small-signal analysis are utilised in the model reduction The derived converters models lay foundation for the dynamic analysis of MTDC systems.

## 2.2 Modelling of the Line Commutated Converter

### 2.2.1 Dynamic Equations of the LCC-Based Rectifier

In MTDC systems, the LCCs usually serve as rectifiers to avoid commutation failure. Therefore, this thesis only considers the LCC-based rectifier. Fig. 2-1 depicts the sketch and equivalent circuit of the LCC-based rectifier. $i_{dc}$ and $u_{dc}$ are the DC-link current and voltage, separately. $V_o$ is the ideal no-load voltage of the LCC satisfying $V_o = 3\sqrt{2}E/\pi$, and $E$ is the AC-side root-mean-square (RMS) line voltage. $L_d$ is the inductance of the smoothing reactor. $d_\gamma$ is the equivalent commutation resistance.

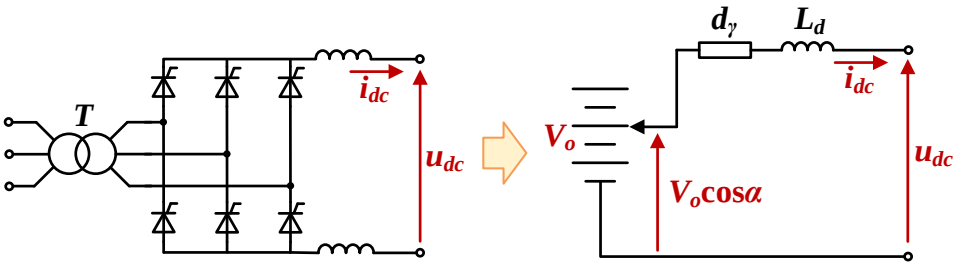


Fig. 2-1 Sketch and equivalent circuit of the LCC.

The dynamics of the LCC-based rectifier are written as,

$$u_{dc} = V_o \cos\alpha - d_\gamma i_{dc} - L_d \frac{\mathrm{d}i_{dc}}{\mathrm{d}t} \tag{2-1}$$

where $\alpha$ is the firing angle of the rectifier. The equivalent commutation resistance $d_\gamma$ is calculated as,

$$d_\gamma = \frac{3\omega_s L_\gamma}{\pi} \tag{2-2}$$

where $\omega_s$ denotes the frequency of the AC system; $L_\gamma$ denotes the equivalent inductance between AC system and the LCC.

Usually, the LCC-based rectifier regulates constant DC-link current by a proportional-integral (PI) controller, as illustrated by Fig. 2-2. The dynamics of the constant current controller can be written as,

$$\alpha = \pi - K_{Pc}\left(i_{dc}^{ref} - i_{dc}\right) - K_{Ic}\int\left(i_{dc}^{ref} - i_{dc}\right)\mathrm{d}t \tag{2-3}$$

where the superscript *ref* denotes the reference value. $K_{Pc}$ and $K_{Ic}$ are the proportional and integral gains of the constant current controller. It is assumed that the PI controller will not saturate to its limiting values under disturbances.

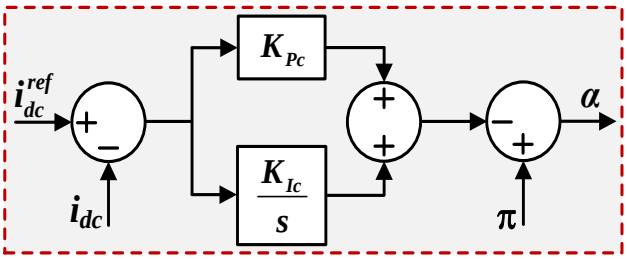


Fig. 2-2 Control diagram of the constant current control.

As this thesis concentrates on the dynamics of MTDC systems under DC-side disturbances, it is assumed that an ideal AC connects to the LCC, and the dynamics of the PLL can be overlooked.

### 2.2.2 Small-Signal Model of the LCC-Based Rectifier

When a small perturbation occurs at the DC link, the terminal voltage of the LCC slightly deviates from the nominal value. Accordingly, the classic small-signal analysis is adopted to simplify the LCC model. Linearizing (2-1) and (2-3) around one equilibrium and applying the Laplace transform, it yields that,

$$\Delta u_{dc} = -V_o \sin\alpha_0 \Delta\alpha - d_\gamma \Delta i_{dc} - sL_d \Delta i_{dc} \tag{2-4}$$

$$\Delta\alpha = \left( K_{Pc} + \frac{K_{Ic}}{s} \right) \Delta i_{dc} \tag{2-5}$$

where the subscript 0 denotes the initial steady-state value; Δ denotes a general deviation from the equilibrium.

Combined with (2-4) and (2-5), we have,

$$\Delta i_{dc} = -\frac{\Delta u_{dc}}{sL_d + \left( d_\gamma + V_0 \sin\alpha_0 K_{Pc} \right) + \dfrac{V_0 \sin\alpha_0 K_{Ic}}{s}} \tag{2-6}$$

(2-6) is the small-signal model of the LCC-based rectifier, which describes the DC-link current responses with the change of the DC-link voltage.

### 2.2.3 Linearized Model of the LCC-Based Rectifier for DC Fault Analysis

When a DC fault occurs, the DC-link voltage of the LCC fast drops by the constant current control to suppress the surge of the DC-link current. In this scenario, the LCC can deviate far from the steady-state point, and thus the small-signal model expressed by (2-6) cannot hold for the fault analysis. Due to the nonlinearity brought by $\cos\alpha$ in (2-1), it requires numerical calculation to obtain the dynamic responses of the LCC. Therefore, the key step in deriving the reduced LCC model for DC fault analysis is to find a proper linearization of $\cos\alpha$. A linear approximation function of $\cos\alpha$ denoted by $f_l(\alpha)$ can be constructed as,

$$\cos\alpha \approx f_l(\alpha) = \cos\alpha_0 - k_\alpha (\alpha - \alpha_0) \tag{2-7}$$

where $k_\alpha$ is the slope of the linear approximation function $f_l(\alpha)$. Based on (2-7), both $f_l(\alpha)$ and $\cos\alpha$ cross the same point $(\alpha_0, \cos\alpha_0)$, which ensures the approximation does not change the pre-fault condition of the LCC. The optimal slope $k_\alpha$ is determined in the sense of least squares, i.e., by minimizing the integral error between the original function $\cos\alpha$ and the approximation function $f_l(\alpha)$ over the interval $[\alpha_0, \alpha_1]$.

$$\min_{k_\alpha} J = \min_{k_\alpha} \int_{\alpha_0}^{\alpha_1} \left( f_l(\alpha) - \cos\alpha \right)^2 \mathrm{d}\alpha \tag{2-8}$$

where $J$ denotes the objective function. The optimal slope $k_\alpha$ is achieved when the derivative of $J$ with respect to $k_\alpha$ equals 0. Based on (2-7) and (2-8), we have,

$$\begin{aligned} &\frac{\mathrm{d}J}{\mathrm{d}k_\alpha} = 0 \quad \Rightarrow \\ &\int_{\alpha_0}^{\alpha_1} \left( \cos\alpha_0 - k_\alpha (\alpha - \alpha_0) \right)^2 \mathrm{d}\alpha - 2\int_{\alpha_0}^{\alpha_1} \left( \cos\alpha_0 - k_\alpha (\alpha - \alpha_0) \right) \cos\alpha \mathrm{d}\alpha + \int_{\alpha_0}^{\alpha} \cos^2\alpha \mathrm{d}\alpha = 0 \end{aligned} \tag{2-9}$$

Rearranging (2-9), it provides the expression of $k_\alpha$.

$$
\begin{aligned}
k_\alpha &= -\frac{\int_{\alpha_0}^{\alpha_1}(\alpha-\alpha_0)(\cos\alpha-\cos\alpha_0)\,\mathrm{d}\alpha}{\int_{\alpha_0}^{\alpha_1}(\alpha-\alpha_0)^2\,\mathrm{d}\alpha} \\
&= \frac{3\cos\alpha_0}{2(\alpha_1-\alpha_0)} - \frac{3\left((\alpha_1-\alpha_0)\sin\alpha_1+\cos\alpha_1-\cos\alpha_0\right)}{(\alpha_1-\alpha_0)^3}
\end{aligned} \tag{2-10}
$$

On the one hand, $\alpha_0$ normally falls into [π/36, π/12] for the LCC-based rectifier to make a tradeoff between the transmission power factor and the DC-link voltage regulation capability. On the other hand, the firing angle surges to around π/2 after the DC fault by the constant current controller. Therefore, $\alpha_1$ is selected as π/2 in this thesis.

Replace $\cos\alpha$ with $f_l(\alpha)$, (2-1) can be rewritten as,

$$
\begin{aligned}
&u_{dc} = V_o\left(\cos\alpha_0 - k_\alpha\left(\alpha-\alpha_0\right)\right) - d_\gamma i_{dc} - L_d\frac{\mathrm{d}i_{dc}}{\mathrm{d}t} \quad \Rightarrow \\
&u_{dc0} + \Delta u_{dc} = V_o\left(\cos\alpha_0 - k_\alpha\Delta\alpha\right) - d_\gamma\left(i_{dc0}+\Delta i_{dc}\right) - L_d\frac{\mathrm{d}\Delta i_{dc}}{\mathrm{d}t}
\end{aligned} \tag{2-11}
$$

Notice the steady-state relation of (2-1),

$$
u_{dc0} = V_o\cos\alpha_0 - d_\gamma i_{dc0} \tag{2-12}
$$

Substitute (2-12) into (2-11),

$$
\Delta u_{dc} = -V_o k_\alpha\Delta\alpha - d_\gamma\Delta i_{dc} - L_d\frac{\mathrm{d}\Delta i_{dc}}{\mathrm{d}t} \tag{2-13}
$$

Similarly, the relation between $\Delta\alpha$ and $\Delta i_d$ can be obtained based on (2-3),

$$
\Delta\alpha = K_{Ic}\Delta i_{dc} + K_{Ic}\int\Delta i_{dc}\mathrm{d}t \tag{2-14}
$$

As (2-13) and (2-14) are linear equations, the Laplace transform can be applied to them, yielding the linearized model of the LCC-based rectifier under DC faults.

$$
\Delta i_{dc} = -\frac{\Delta u_{dc}}{sL_d + \left(d_\gamma + V_o k_\alpha K_{Pc}\right) + \dfrac{V_o k_\alpha K_{Ic}}{s}} \tag{2-15}
$$

### 2.2.4 DC-Side Equivalent Circuit of the LCC-Based Rectifier

Compared with (2-6) and (2-15), the LCC-based rectifier under different sizes of disturbances can be equivalent to a uniform RLC series circuit, as illustrated by Fig. 2-3. $R_{eq}^{LCC}$ and $C_{eq}^{LCC}$ are the equivalent resistance and capacitance of the LCC, which incorporate the impacts of the constant current control. The equivalent parameters under small perturbations and DC faults are expressed by (2-16) and (2-17), respectively.

$$\begin{cases} R_{eq}^{LCC} = d_{\gamma} + V_o \sin\alpha_0 K_{Pc} \\ C_{eq}^{LCC} = \dfrac{1}{V_o \sin\alpha_0 K_{Ic}} \end{cases} \tag{2-16}$$

$$\begin{cases} R_{eq}^{LCC} = d_{\gamma} + V_o k_{\alpha} K_{Pc} \\ C_{eq}^{LCC} = \dfrac{1}{V_o k_{\alpha} K_{Ic}} \end{cases} \tag{2-17}$$

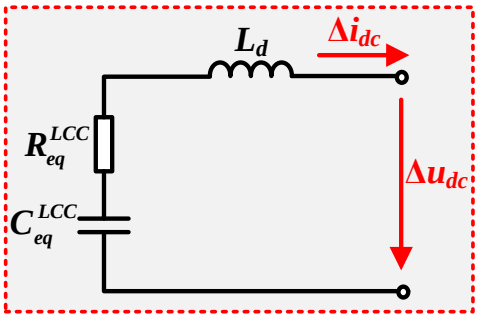


Fig. 2-3 Equivalent circuit of the LCC-based rectifier under DC-side disturbances.

In practical engineering, the LCC-based rectifier can also adopt other control modes, such as constant active power control. It should be noted that the proposed method is also applicable to LCCs with other control modes. Taking the constant active power control as an example, under normal-condition perturbations, the small-signal analysis is utilised as the variations of the DC-link terminal voltage of the LCC are relatively small. By substituting the constant current control equation with the constant active power control equation, the small-signal model of the LCC with the constant active power can be obtained. Under DC faults, the DC-link terminal voltage of the LCC drops drastically. To avoid overcurrent damaging the valves, constant active power control must switch to constant current control. Consequently, the derived model of the LCC-based rectifier for DC fault analysis is the same no matter the control mode.

## 2.3 Modelling of the Two-Level Voltage-Source Converter

### 2.3.1 Dynamic Equations of the TLVSC

Fig. 2-4 depicts the equivalent circuit of the grid-connected TLVSC. $L_s$ and $R_s$ are the inductance and the resistance of the phase reactor between the AC grid and the converter, respectively. $u_s$ and $u_c$ are the voltage of the AC grid and the AC terminal of the converter, respectively. $i_s$ is the AC-side current of the converter. $C_c$ is the capacitance of the DC-link capacitor. $L_T$ is the inductance of the supplementary DC reactor to suppress DC-link harmonic

current under normal operation and DC-link current surge during the occurrence of faults. $u_d$ and $u_{dc}$ are the DC-side voltage of the TLVSC before and after the DC reactor, individually. $i_d$ and $i_c$ are the DC-link current of the converter and the capacitor, individually. $i_{dc}$ is the current flowing through the DC reactor.

According to the AC-side circuit of the grid-tied TLVSC, the following equation holds in the three-phase coordinate system,

$$u_s^j - u_c^j = L_s \frac{\mathrm{d}i_s^j}{\mathrm{d}t} + R_s i_s^j, \quad j = a,b,c \tag{2-18}$$

where the superscript $j$ denotes the three phases. For VSCs, the $dq$ coordinate system is normally utilised to realize the decoupled active and reactive power control. Considering the active power of the converter is highly associated with the $d$-axis components, only the $d$-axis dynamic equation of (2-18) is given as,

$$u_s^d - u_c^d = L_s \frac{\mathrm{d}i_s^d}{\mathrm{d}t} + R_s i_s^d - \omega_s L_s i_c^q \tag{2-19}$$

where the superscripts $d$ and $q$ denote the $d$- and $q$-axis components, individually. Under the classic unity power factor control, the reactive power of the converter is regulated as 0 to maximise the active power transmission, and thus $i_c^q = 0$.

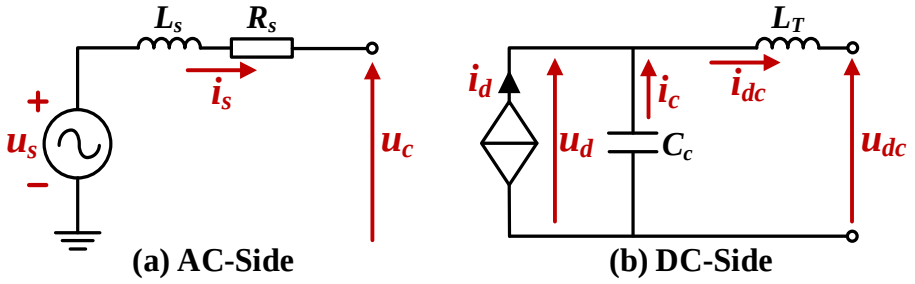


Fig. 2-4 Equivalent circuit of the grid-connected TLVSC.

At the DC side, the dynamics of the capacitor and the reactor are expressed as,

$$C_c \frac{\mathrm{d}u_d}{\mathrm{d}t} = -i_c \tag{2-20}$$

$$L_T \frac{\mathrm{d}i_{dc}}{\mathrm{d}t} = u_d - u_{dc} \tag{2-21}$$

By using Kirchhoff current law (KCL), the following equation holds,

$$i_d + i_c - i_{dc} = 0 \tag{2-22}$$

In addition, the power balance equation expressed by (2-23) holds when overlooking the

loss of the transformer and the converter.

$$P_{ac}=\frac{3}{2}u_c^d i_s^d \approx \frac{3}{2}u_s^d i_s^d \approx P_{dc}=u_d i_d \tag{2-23}$$

where $P_{ac}$ and $P_{dc}$ are the AC- and DC-side active power of the converter.

Fig. 2-5 depicts the diagram of the vector current control, which comprises an inner loop and an outer loop. The inner current loop makes the AC-link current of the converter to fast track the reference value, which is expressed as,

$$u_c^d=-K_{Pi}\left(i_s^{dref}-i_s^d\right)-K_{Ii}\int\left(i_s^{dref}-i_s^d\right)\mathrm{d}t+u_s^d+\omega_s L_s i_s^q \tag{2-24}$$

where $K_{Pi}$ and $K_{Ii}$ are the proportional and integral gains of the inner current loop.

Broadly, the outer loop control schemes fall into three categories, namely, the constant power control (CPC), the constant DC voltage control (CDVC), and the power-voltage droop control. The former two schemes maintain the active power of the converter and its DC-link voltage, respectively. The droop control can enhance the DC-link voltage stability and realize automatic active power sharing among different VSCs, thereby showing bright prospects in MTDC systems. The diagram of the droop control is illustrated by Fig. 2-5, and its dynamic equation is given as follows.

$$i_s^{dref}=K_{Po}\left(P_{ac}^{ref}+K_d\left(u_d^{ref}-u_d\right)-P_{ac}\right)+K_{Io}\int\left(P_{ac}^{ref}+K_d\left(u_d^{ref}-u_d\right)-P_{ac}\right)\mathrm{d}t \tag{2-25}$$

where $K_{Po}$ and $K_{Io}$ are the proportional and integral gains of the outer loop.

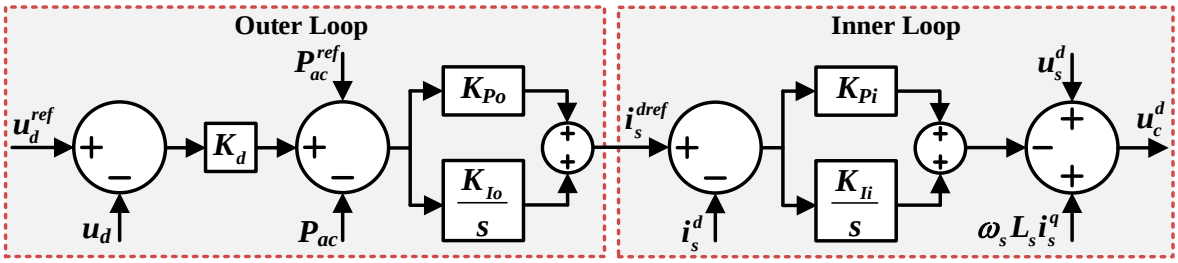


Fig. 2-5 Diagram of the vector current control.

In addition, the droop control can switch into the CPC by configuring the droop coefficient $K_d$ as 0. As for the CDVC, its equation is expressed as,

$$i_s^{dref}=K_{Pv}\left(u_d^{ref}-u_d\right)+K_{Iv}\int\left(u_d^{ref}-u_d\right)\mathrm{d}t \tag{2-26}$$

where $K_{Pv}$ and $K_{Iv}$ are the proportional and integral gains of the CDVC.

Similar to the LCC, the converter-connected AC system is assumed to be ideal, and thus the dynamics of the PLL of the TLVSC are omitted for the DC-side dynamic analysis.

### 2.3.2 Small-Signal Model of the TLVSC Under Different Control Modes

After the occurrence of a DC fault, the fault line must be fast cut off within the capacitor discharging stage to avoid the blocking of VSCs and the interruption of the entire MTDC system. Therefore, short-circuit current calculation during the initial fault period is of more interest for MTDC systems. Within this short period, the decrease in the DC-link voltage is relatively small because of the existence of the DC-link capacitor, and the changes in the AC-side voltage and current are minimal. Consequently, nonlinear equations containing corresponding variables can be linearized at the equilibrium point. In addition, the growth of the DC-link current of VSC can be described by the linear dynamic equation of the capacitor. Therefore, the VSC exhibits linear circuit characteristics during the initial stage of the fault so that the linear VSC model based on small-signal analysis is applicable under small perturbations and DC faults.

Linearizing (2-19) and (2-24) around one equilibrium and applying the Laplace transform, it yields that,

$$\Delta u_c^d = -\left(sL_s + R_s\right)\Delta i_s^d + \omega_s L_s \Delta i_c^q \tag{2-27}$$

$$\Delta u_c^d = -\left(K_{Pi} + \frac{K_{Ii}}{s}\right)\left(\Delta i_s^{dref} - \Delta i_s^d\right) + \omega_s L_s \Delta i_s^q \tag{2-28}$$

Combined with (2-27) and (2-28) provides,

$$\left(sL_s + R_s + K_{Pi} + \frac{K_{Ii}}{s}\right)\Delta i_s^d = \left(K_{Pi} + \frac{K_{Ii}}{s}\right)\Delta i_s^{dref} \tag{2-29}$$

Usually, (2-29) is designed to possess first-order system chracteristics by tuning the PI parameters based on (2-30) [100].

$$\frac{\Delta i_s^d}{\Delta i_s^{dref}} = \frac{1}{\sigma_i s + 1} \qquad \left(\frac{L_s}{K_{Pi}} = \frac{R_s}{K_{Ii}} = \sigma_i\right) \tag{2-30}$$

Based on (2-25), the small-signal form of the outer loop control is expressed as,

$$\Delta i_s^{dref} = -\left(K_{Po} + \frac{K_{Io}}{s}\right)\left(K_d \Delta u_d + \Delta P_{ac}\right) \tag{2-31}$$

Combined with (2-30) and (2-31) yields,

$$\left(\sigma_i s + 1\right)\Delta i_s^d = -\left(K_{Po} + \frac{K_{Io}}{s}\right)\left(K_d \Delta u_d + \Delta P_{ac}\right) \tag{2-32}$$

Linearizing the power balance equation expressed by (2-23), we have,

$$\Delta P_{ac} = \frac{3}{2} u_s^d \Delta i_s^d = i_{d0} \Delta u_d + u_{d0} \Delta i_d \tag{2-33}$$

Substituting (2-33) into (2-32) provides,

$$\left(\sigma_i s+1+\frac{3}{2}u_s^d\left(K_{Po}+\frac{K_{Io}}{s}\right)\right)\Delta i_s^d=-K_d\left(K_{Po}+\frac{K_{Io}}{s}\right)\Delta u_d \tag{2-34}$$

Rearranging (2-33) and (2-34), it yields that,

$$-G_d(s)\Delta u_d=\Delta i_d \tag{2-35}$$

where $G_d(s)$ is the transfer function between $\Delta i_d$ and $\Delta u_d$ under the droop control, which is expressed as,

$$G_d(s)=\frac{3u_s^d K_d\left(K_{Po}s+K_{Io}\right)}{u_{d0}\left(2\left(\sigma_i s+1\right)s+3u_s^d\left(K_{Po}s+K_{Io}\right)\right)}+g_{d0},\quad g_{d0}=\frac{i_{d0}}{u_{d0}} \tag{2-36}$$

where $g_{d0}$ is the equivalent DC-side conductance of the converter.

Based on (2-20), (2-21), (2-22), and (2-35), the following equation holds.

$$\Delta u_{dc}=-\left(sL_T+\frac{1}{G_d(s)+sC_c}\right)\Delta i_{dc} \tag{2-37}$$

(2-37) is the small-signal model of the droop-based TLVSCs, where $G_d(s)$ reflects the control effects on the dynamic responses of the converter.

By configuring the droop coefficient $K_d$ as 0, the droop control switches into the CPC. Substitution of $K_d = 0$ into (2-36), $G_d(s)$ is reduced as $g_{d0}$, and the small-signal model of the TLVSC under the CPC is obtained.

$$\Delta u_{dc}=-\left(sL_T+\frac{1}{g_{d0}+sC_c}\right)\Delta i_{dc} \tag{2-38}$$

(2-38) shows that the control parameters have negligible effects on the DC-side dynamics of the CPC-based TLVSC.

As for the CDVC, transforming (2-26) into the small-signal form yields,

$$\Delta i_s^{dref}=-\left(K_{Pv}+\frac{K_{Iv}}{s}\right)\Delta u_d \tag{2-39}$$

By combining (2-30), (2-33), and (2-39), the transfer function between $\Delta i_d$ and $\Delta u_d$ under the CDVC denoted by $G_v(s)$ can be expressed as,

$$-G_v(s)\Delta u_d=\Delta i_d,\quad G_v(s)=\frac{3u_s^d\left(K_{Pv}s+K_{Iv}\right)}{2u_{d0}\left(\sigma_i s+1\right)s}+g_{d0} \tag{2-40}$$

As a result, the small-signal model of the TLVSC under the CDVC is obtained as (2-41) based on (2-20), (2-21), (2-22), and (2-40).

$$\Delta u_{dc} = -\left( sL_T + \frac{1}{G_v(s) + sC_c} \right) \Delta i_{dc} \tag{2-41}$$

### 2.3.3 DC-Side Equivalent Circuit of the TLVSC

On the basis of the small-signal models of the TLVSC under different control modes, the equivalent circuits under DC-side disturbances can be derived as follows.

1) Constant Power Control

Based on (2-38), the TLVSC under CPC is represented by an RLC circuit, as illustrated by Fig. 2-6. $R_{eq}^{VSC}$ is the equivalent resistance of the TLVSC, which is expressed as,

$$R_{eq}^{VSC} = \frac{1}{g_{d0}} = \frac{u_{d0}}{i_{d0}} \tag{2-42}$$

Based on (2-42), $R_{eq}^{VSC}$ is positive for the CPC-based TLVSC ($i_{d0} > 0$), while it turns negative when the CPC-based TLVSC operates as the inverter ($i_{d0} > 0$).

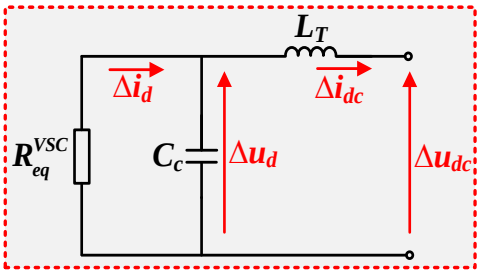


Fig. 2-6 DC-side equivalent circuits of the TLVSC under the CPC mode.

2) Constant DC Voltage Control

Since the proportional regulator inevitably leads to steady-state deviations, an integrator with a relatively low gain is required to push the DC-link voltage back to its reference value. For small values of $K_{Iv}$, the integrator has negligible effects on the overall dynamics, which therefore is assumed to be 0 for deriving the equivalent circuit of the CDVC-based TLVSC [101], [102]. The transfer function $G_v(s)$ is simplified as,

$$G_v(s) = \frac{3u_s^d K_{Pv}}{2u_{d0}(\sigma_i s + 1)} + g_{d0} \tag{2-43}$$

Based on (2-41) and (2-43), the CDVC-based TLVSC is equivalent to an RLC circuit, as illustrated by Fig. 2-7. $R_{eqp}^{VSC}$, $R_{eqs}^{VSC}$, and $L_{eq}^{VSC}$ the equivalent resistances and inductance of the TLVSC, which are expressed as,

$$\begin{cases} R_{eqp}^{VSC} = \dfrac{1}{g_{d0}} = \dfrac{u_{d0}}{i_{d0}} \\ R_{eqs}^{VSC} = \dfrac{2u_{d0}}{3u_s^d K_{Pv}} \\ L_{eq}^{VSC} = \dfrac{2u_{d0}\sigma_i}{3u_s^d K_{Pv}} \end{cases} \tag{2-44}$$

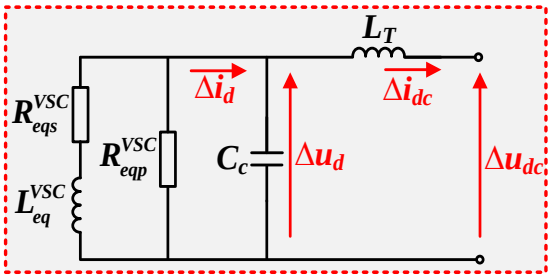


Fig. 2-7 DC-side equivalent circuits of the TLVSC under the CDVC mode.

3) Droop Control

Similarly, the transfer function $G_d(s)$ can be simplified as follows by overlooking the small value of $K_{Io}$.

$$G_d(s) = \frac{3u_s^d K_d K_{Po}}{u_{d0}\left(2(\sigma_i s + 1) + 3u_s^d K_{Po}\right)} + g_{d0} \tag{2-45}$$

Based on (2-37) and (2-45), the DC-side equivalent circuit of the TLVSC under the droop control is similar to that of the CDVC-based one, as shown in Fig. 2-7. The difference is the equivalent parameters under the droop control are calculated as,

$$\begin{cases} R_{eqp}^{VSC} = \dfrac{1}{g_{d0}} = \dfrac{u_{d0}}{i_{d0}} \\ R_{eqs}^{VSC} = \dfrac{2u_{d0} + 3u_s^d K_{Po}}{3u_s^d K_d K_{Po}} \\ L_{eq}^{VSC} = \dfrac{2u_{d0}\sigma_i}{3u_s^d K_d K_{Po}} \end{cases} \tag{2-46}$$

Compared with Fig. 2-6 and Fig. 2-7, it is found that the TLVSC under different control modes can be equivalent to RLC circuits for the dynamic analysis under DC disturbances.

## 2.4 Modelling of the Modular Multilevel Converter

### 2.4.1 Dynamic Equations of the MMC

The MMC is a category of VSCs, whose basic structure is illustrated by Fig. 2-8. Every

phase has an upper and a lower arm composed of $N_{sm}$ half-bridge sub-modules (SMs). Depending on the one SM switched in or out, the terminal voltage of the SM equals the capacitor voltage denoted by $u_{sm}$ or 0. By controlling the number of on-state SMs in the upper and low arms, the AC-side voltage of the converter marked as $u_v$ and the DC-link voltage marked as $u_{dc}$ can be controlled effectively. The capacitance of each SM is denoted as $C_{sm}$. The equivalent arm resistance and inductance are denoted by $R_a$ and $L_a$, individaully. $u_s$ and $i_s$ are the AC source voltage and the current flowing from the AC source into the converter, individaully. $i_p$ and $i_n$ are the current flowing through the upper and lower arm, individually. $u_p$ and $u_n$ are the upper and lower arm voltages generated by cascaded SMs, individually.

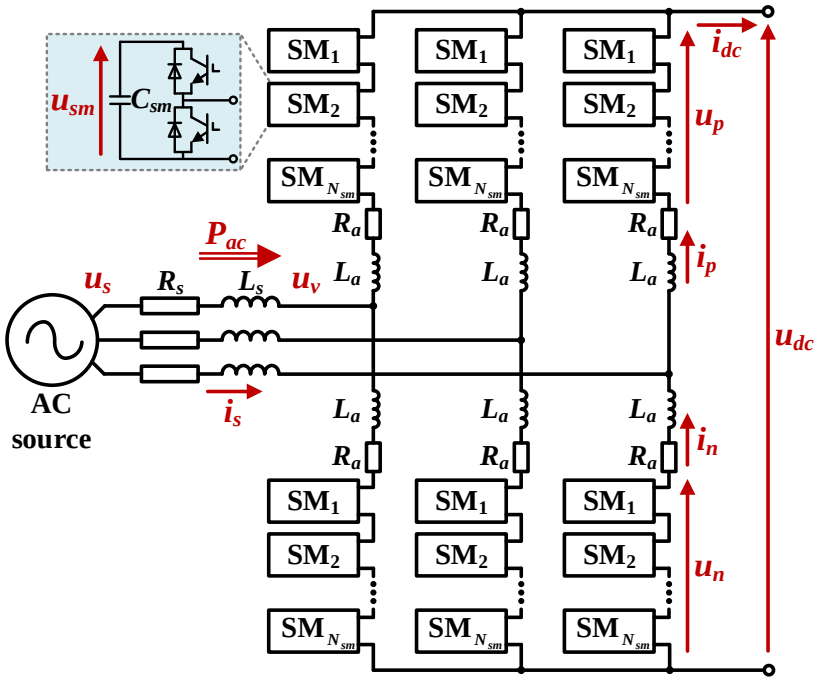


Fig. 2-8 Diagram of the MMC.

The dynamics of each phase are expressed as,

$$\begin{cases} u_v^j - \dfrac{u_{dc}}{2} = R_a i_p^j + L_a \dfrac{\mathrm{d}i_p^j}{\mathrm{d}t} - u_p^j \\ -\dfrac{u_{dc}}{2} - u_v^j = R_a i_n^j + L_a \dfrac{\mathrm{d}i_n^j}{\mathrm{d}t} - u_n^j \end{cases} \tag{2-47}$$

where the superscript $j$ represents the three-phase electrical quantities, $j = a, b, c$.

It is assumed that the harmonic current of the MMC can be effectively damped by choosing the proper parameters of the circulating current control [103], [104]. Accordingly, the arm currents satisfy the following equations.

$$\begin{cases} i_p^j = \dfrac{i_{dc}}{3} + \dfrac{i_s^j}{2} \\ i_n^j = \dfrac{i_{dc}}{3} - \dfrac{i_s^j}{2} \end{cases} \tag{2-48}$$

Substitution of (2-48) into (2-47) yields,

$$\begin{cases} u_v^j - u_c^j = \dfrac{R_a}{2} i_s^j + \dfrac{L_a}{2} \dfrac{\mathrm{d}i_s^j}{\mathrm{d}t} \\ u_d - u_{dc} = \dfrac{2}{3} R_a i_{dc} + \dfrac{2}{3} L_a \dfrac{\mathrm{d}i_{dc}}{\mathrm{d}t} \end{cases} \tag{2-49}$$

where $u_d$ are $u_c$ are the total capacitor voltage and the inner electromotive force generated in each phase satisfying,

$$\begin{cases} u_d = u_p^j + u_n^j \\ u_c^j = \left(u_n^j - u_p^j\right)/2 \end{cases} \tag{2-50}$$

(2-49) indicates that the AC-side equivalent resistance and inductance of the grid-tied MMC are individually $R_a/2$ and $L_a/2$. Meanwhile, its DC-side equivalent resistance and inductance are $R_M = 2R_a/3$ and $L_M = 2L_a/3$, respectively.

By energy balancing law, the equivalent capacitance of all three-phase units marked as $C_M$ can be derived as follows.

$$\begin{cases} \dfrac{1}{2} 6 N_{sm} C_{sm} u_{sm}^2 = \dfrac{1}{2} C_M u_d^2 \\ N_{sm} u_{sm} = u_d \end{cases} \quad \Rightarrow \quad C_M = \frac{6C_{sm}}{N_{sm}} \tag{2-51}$$

The time derivative of the capacitor energy equals the active power of the capacitor, and thus,

$$\sum_{j=a,b,c} u_p^j \left(i_p^j\right)^* + u_n^j \left(i_n^j\right)^* = -\frac{\mathrm{d}\left(C_M u_d^2/2\right)}{\mathrm{d}t} = u_d \left(-C_M \frac{\mathrm{d}u_d}{\mathrm{d}t}\right) \tag{2-52}$$

where the superscript * represents the complex conjugate. The time derivative of $u_d$ times the capacitance $C_M$ is defined as the total capacitor current of the MMC denoted by $i_c$, which is expressed as,

$$-C_M \frac{\mathrm{d}u_d}{\mathrm{d}t} = i_c \tag{2-53}$$

Substitution of (2-48) and (2-50) into (2-52) provides,

$$u_d i_c = \sum_{j=a,b,c} u_p^j \left( \frac{i_{dc}}{3} + \frac{i_s^j}{2} \right)^* + u_n^j \left( \frac{i_{dc}}{3} - \frac{i_s^j}{2} \right)^* = \sum_{j=a,b,c} \left( u_p^j + u_n^j \right) \frac{i_{dc}}{3} + \sum_{j=a,b,c} \left( u_p^j - u_n^j \right) \left( \frac{i_s^j}{2} \right)^* \\ = u_d i_{dc} - \sum_{j=a,b,c} u_c^j \left( i_s^j \right)^* \tag{2-54}$$

Neglecting the small amount of power loss in the converter and the transformer, the following power balancing equation is derived from (2-54).

$$u_d i_c = u_d i_{dc} - P_{ac} = u_d i_{dc} - \frac{3}{2} u_s^d i_s^d \tag{2-55}$$

Based on (2-55), the infeed current into the DC link denoted by $i_d$ can be obtained.

$$i_d = i_{dc} - i_c = \frac{P_{ac}}{u_d} \tag{2-56}$$

Based on (2-49), (2-53), and (2-56), the equivalent circuit of the grid-tied MMC is obtained, as illustrated by Fig. 2-9. Compared Fig. 2-4 with Fig. 2-9, it is concluded that the equivalent circuit of the grid-connected MMC is similar to that of the grid-connected TLVSC. The small arm resistance and inductance of the MMC will slightly change the parameters in the equivalent circuit.

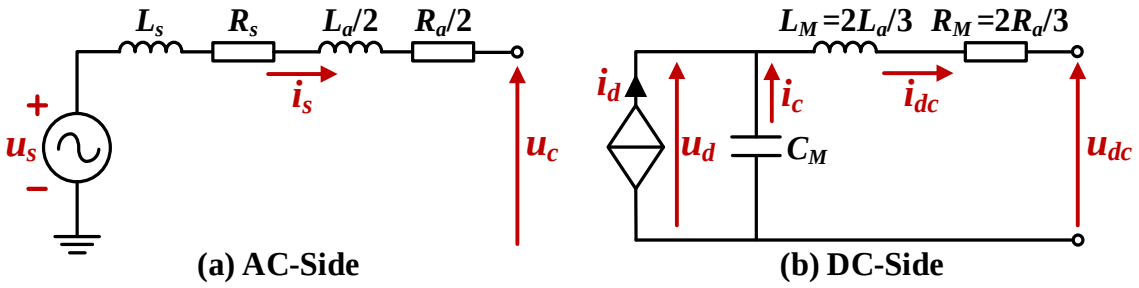


Fig. 2-9 Equivalent circuit of the grid-connected MMC.

As for the control system, the MMC also adopts the vector current control, as depicted by Fig. 2-5. The control equations of the MMC are expressed by (2-24), (2-25), and (2-26).

## 2.4.2 Small-Signal Model of the MMC Under Different Control Modes

Analogous to the TLVSC, the DC-link voltage of the MMC drops slightly within the first instants after the occurrence of DC faults due to the support of the submodular capacitors. Accordingly, the small-signal model of the MMC is also applicable during the first instants after DC faults. The derivation of the small-signal model of the MMC is analogous to that of the TLVSC, which is not presented here.

By using the small-signal analysis, the DC-link voltage and current of the CPC-based MMC satisfy the following relation.

$$\Delta u_{dc} = -\left( sL_M + R_M + \frac{1}{sC_M + g_{d0}} \right) \Delta i_{dc} \tag{2-57}$$

Under the CDVC, the relation between the DC-link voltage and DC-link current of the MMC becomes,

$$\Delta u_{dc} = -\left( sL_M + R_M + \frac{1}{G_v(s) + sC_M} \right) \Delta i_{dc}, \quad G_v(s) = \frac{3u_s^d \left( K_{Pv} s + K_{Iv} \right)}{2u_{d0} \left( \sigma_i s + 1 \right) s} + g_{d0} \tag{2-58}$$

As for the MMC under the droop control, the small-signal model is expressed as,

$$\Delta u_{dc} = -\left( sL_M + R_M + \frac{1}{G_d(s) + sC_M} \right) \Delta i_{dc}, \quad G_d(s) = \frac{3u_s^d K_d \left( K_{Po} s + K_{Io} \right)}{u_{d0} \left( 2\left( \sigma_i s + 1 \right) s + 3u_s^d \left( K_{Po} s + K_{Io} \right) \right)} \tag{2-59}$$

### 2.4.3 DC-Side Equivalent Circuit of the MMC

On the basis of the above small-signal models expressed by (2-57), (2-58), and (2-59), the DC-side equivalent circuits of the MMC under three control modes can be obtained. Fig. 2-10 (a) depicts the equivalent circuit of the CPC-based MMC, while Fig. 2-10 (b) depicts the equivalent circuit of the MMC under the CDVC or droop control. The equivalent parameter(s) under the CPC, CDVC, and droop control can be expressed by (2-42), (2-44), and (2-46), respectively.

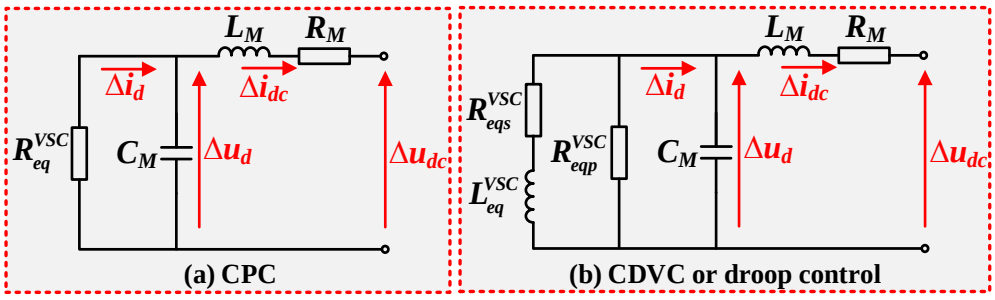


Fig. 2-10 DC-side equivalent circuits of the MMC under different control modes.

## 2.5 Case Studies

The detailed switching models of the LCC, the TLVSC, and the MMC are established in PSCAD/EMTDC to validate the accuracy of the proposed models under DC-side disturbances. The three converters are connected to an ideal DC source via a DC transmission line, separately. The LCC-based rectifier adopts the classic constant current control with the proportional and integral gains of 1 and 100, respectively. The TLVSC under the CPC, CDVC, and droop control is investigated. The proportional and integral gains of the outer loop (for all three

control modes) are configured as 1 and 10, respectively. The power-voltage droop coefficient is 5. The MMC is of 201 levels, and its control parameters are the same as the TLVSC. The main parameters of the test systems are summarized in Table 2-1.

Table 2-1 Main parameters of the test systems

| Symbol | Item | Value |
|---|---|---|
| | LCC | |
| $E$ | Nominal voltage of LCC-connected AC source | 450 kV |
| $\omega_s$ | Nominal frequency of AC grids | 50 Hz |
| $u_n$ | Nominal DC-link voltage of the LCC | 500 kV |
| $S_B$ | Base capacity of the LCC system | 1000 MW |
| $i_{dc}^{ref}$ | Reference DC-link current | 2 kA |
| $d_\gamma$ | Equivalent commutation resistance | 41 Ω |
| $L_d$ | Smoothing reactor of LCC | 200 mH |
| ($K_{Pc}$, $K_{Ic}$) | Proportional and integral gains of constant current control | (1, 100) |
| | TLVSC | |
| $u_s$ | Nominal voltage of VSC-tied AC source | 220 kV |
| $u_n$ | Nominal DC-link voltage of the VSC | 400 kV |
| $S_B$ | Base capacity of the VSC system | 400 MW |
| $C_c$ | DC-link capacitance of VSC | 220 μF |
| $u_s$ | Nominal voltage of VSC-tied AC source | 220 kV |
| | MMC | |
| $u_s$ | Nominal voltage of VSC-tied AC source | 220 kV |
| $u_n$ | Nominal DC-link voltage of the VSC | 400 kV |
| $S_B$ | Base capacity of the VSC system | 400 MW |
| $N_{sm}$ | Number of SMs per arm | 200 |
| $C_{sm}$ | SM capacitance | 6000 μF |
| $R_{on}$ | On-state resistance of a diode or IGBT | 2 mΩ |
| $L_a$ | Inductance of bridge arm | 29 mH |
| $L_T$ | VSC-side supplementary reactor | 100 mH |

### 2.5.1 LCC-Based Rectifier

Fig. 2-11 depicts the dynamics of the LCC-based rectifier under small perturbations. Fig. 2-11 (a) and (b) are the dynamic responses of the DC-link current and the DC-link voltage when the reference DC-link current changes from 1 per unit (p.u.) to 0.8 p.u, respectively. As illustrated by Fig. 2-11 (a), the DC-link current gradually decreases to 0.8 after changing its

reference value, exhibiting the typical characteristics of the inertial element. In contrast, the DC-link voltage maintains quite near the nominal value, indicating the DC-link current alternation has very limited impacts on the DC voltage dynamics. Fig. 2-11 (c) and (d) show the DC-side dynamics when the voltage of the DC source reduces from 1 p.u. to 0.95 p.u. The DC-link current first increases with the drop of the DC-link voltage, as illustrated by Fig. 2-11 (c). Subsequently, the DC-link voltage of the LCC decreases with the influences of the constant current control, as illustrated by Fig. 2-11 (d). Accordingly, the DC-link current gradually returns to its reference value, and the DC-link converter voltage eventually becomes close to the DC source voltage.

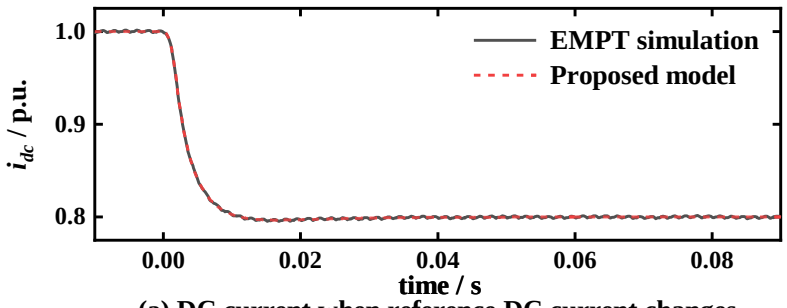


(a) DC current when reference DC current changes

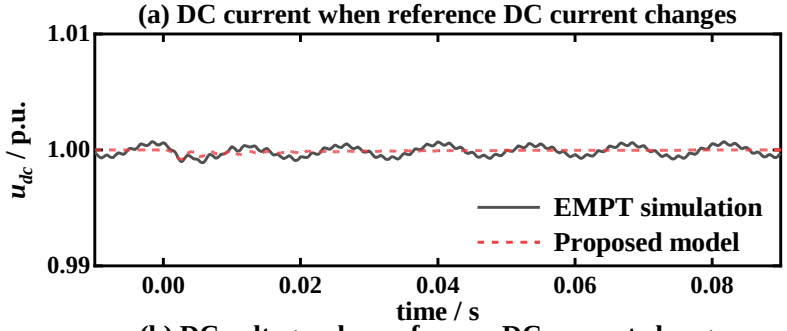


(b) DC voltage when reference DC current changes

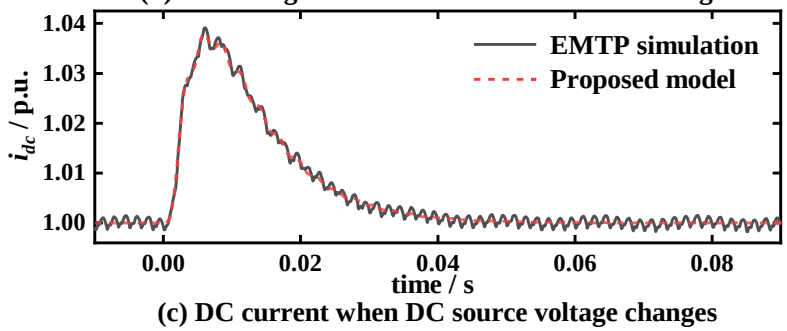


(c) DC current when DC source voltage changes

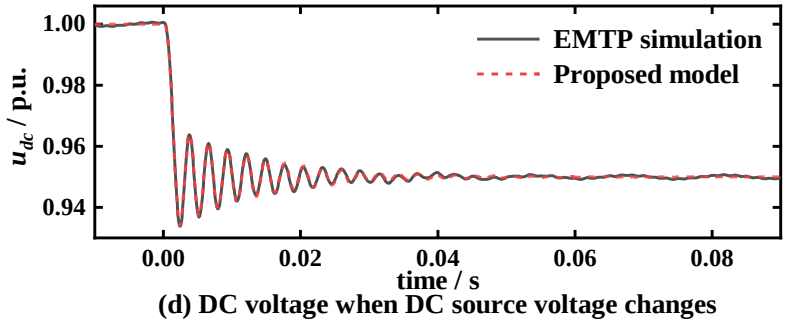


(d) DC voltage when DC source voltage changes

Fig. 2-11 Dynamics of the LCC-based rectifier under small perturbations.

Compared with the results obtained by the EMTP simulation marked as the solid black line and the proposed model marked as the dashed red line, it is found that the proposed model omits the switching process of the converter. Nevertheless, considering the DC-link current and voltage with the simulation vibrate very slightly around those with the proposed model, the proposed model can well reflect the average behaviours of the LCC-based rectifier. Fig. 2-11 verifies the accuracy of the proposed LCC model under small perturbations.

Fig. 2-12 depicts the dynamic responses of the LCC-based rectifier under DC faults. Fig. 2-12 (a) depicts the DC-link current variation when a metallic fault occurs at the beginning of the DC transmission line. The DC-link current rises fast at the occurrence of the fault, and the current rising speed decreases soon owing to the constant current control. With the EMTP simulation, the maximum DC fault current is 1.961 p.u., while that with the proposed model is 2.004 p.u. This is mainly because the nonlinearity of $\cos\alpha$ is approximated by a linear function as expressed by (2-7) with the proposed model. Notably, the relative error of the maximum fault current with these two models is 2.19%, which is fully acceptable for the fault analysis. Fig. 2-12 (b) depicts the DC-link current dynamics under a DC fault with a fault resistance of 100 Ω. Compared with Fig. 2-12 (a) and (b), it is observed that the overall transient processes of the DC-link current are quite similar under low- and high-resistance fault scenarios. As illustrated by Fig. 2-12 (b), the maximum DC fault current with the EMTP simulation and that with the proposed model are 1.696 p.u. and 1.647 p.u., individually, indicating the fault current decreases with the increase of the fault resistance. Fig. 2-12 (c) illustrates the influences of the proportional gain of the controller on the fault current. It can be seen that the DC fault current is significantly suppressed by enlarging the proportional gain, since the response time of the constant current control will reduce with a larger proportional gain. Fig. 2-12 (d) shows that the fault current reduces with the increase in the firing angle. This is because the DC-link voltage goes down when increasing the firing angle. Fig. 2-12 illustrates that the responses with the simulation and those with the proposed model are quite similar under different fault resistances, control parameters, and operating points, which validates the effectiveness of the proposed LCC model for DC fault analysis.

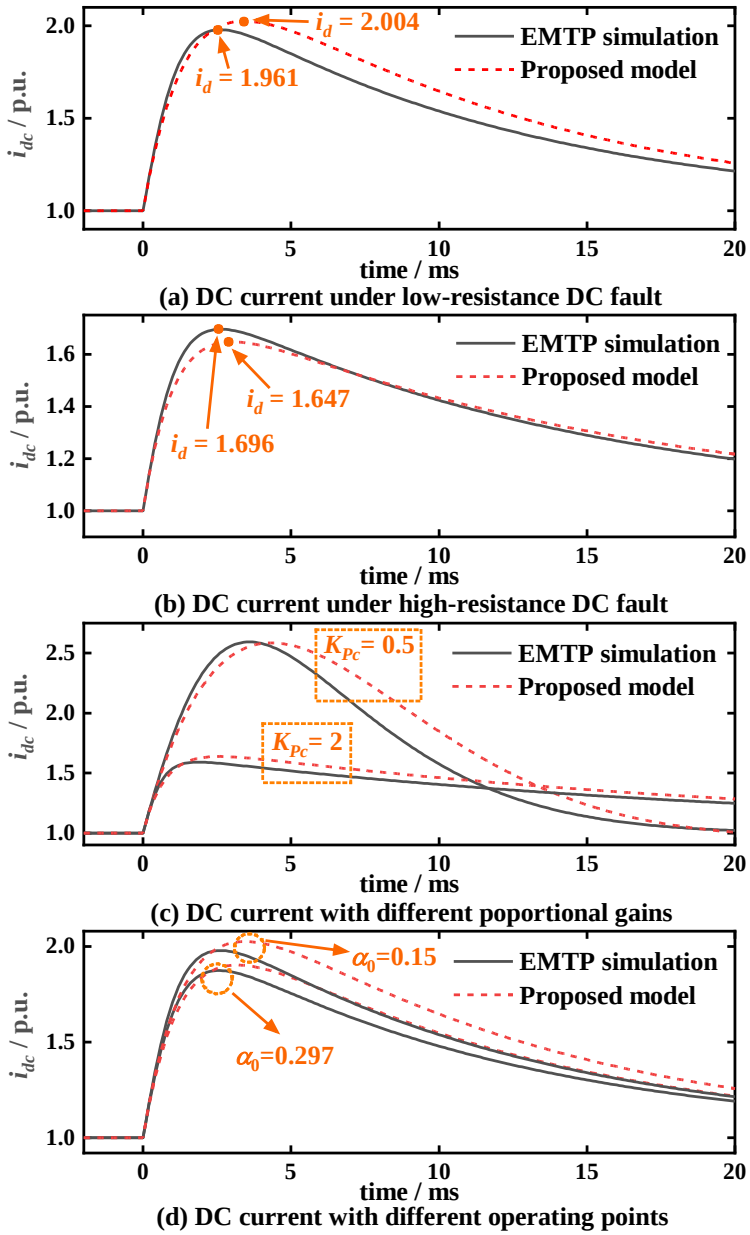


Fig. 2-12 Dynamics of the LCC-based rectifier under DC faults.

### 2.5.2 TLVSC Under Different Control Modes

Fig. 2-13 depicts the dynamic responses of the TLVSC under different control modes when subjected to small perturbations. Fig. 2-13 (a) and (b) depict the change of DC-link current and voltage of the CPC-based TLVSC when the reference active power drops from 1 p.u. to 0.75 p.u. As can be seen from Fig. 2-13 (a), there exhibit apparent oscillations in the DC-link current because of the resonance of the RLC circuit. As illustrated by Fig. 2-13 (b), the change of the DC-link voltage is much minor than that of the current. Moreover, the DC-link voltage slightly deviates from its nominal value after the transient, which is induced by the decrease of the voltage drop over the DC line with the decrease in the DC-link current.

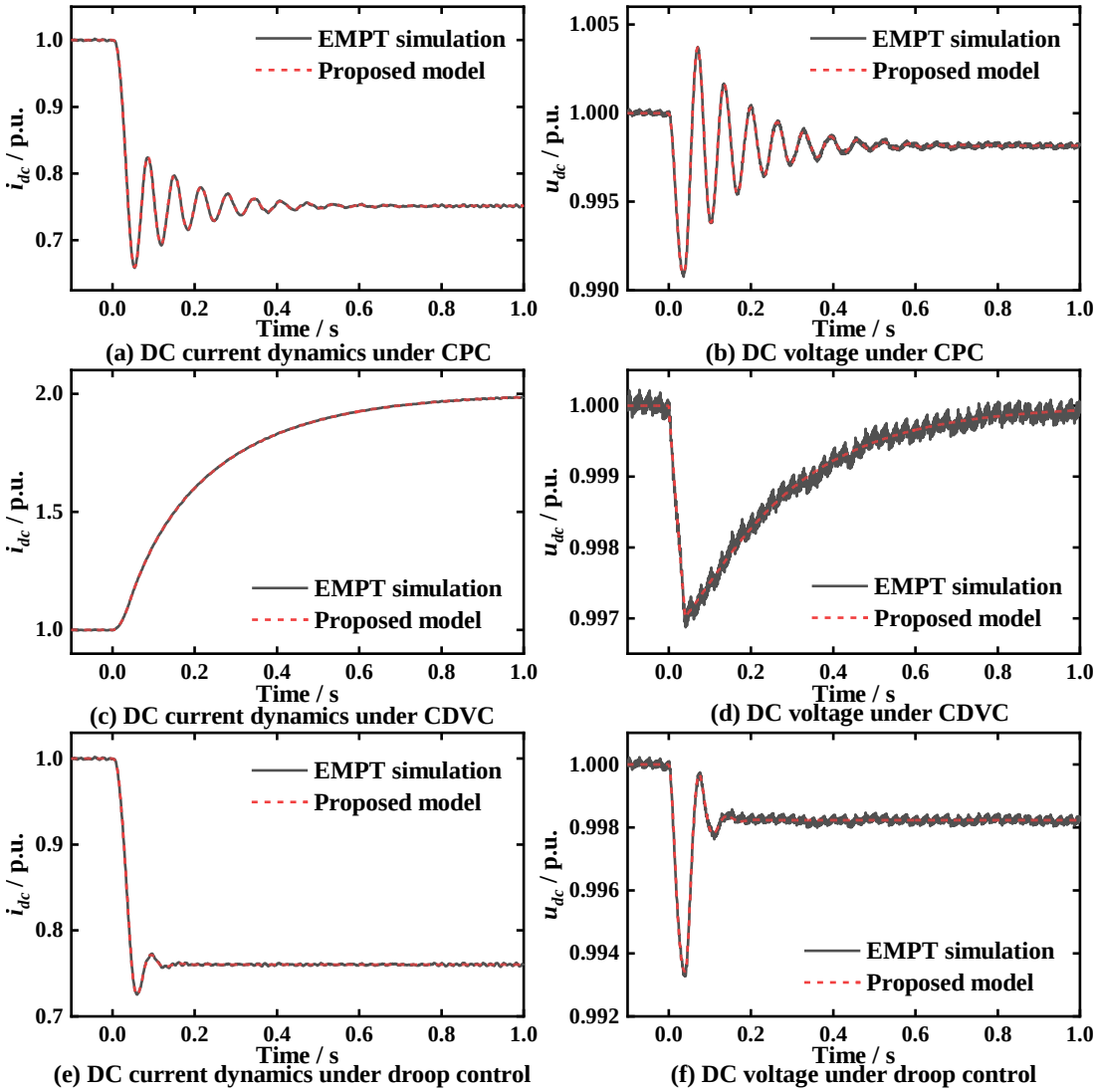


Fig. 2-13 Dynamics of the TLVSC under small perturbations.

Fig. 2-13 (c) and (d) depict the dynamic responses of the CDVC-based TLVSC when the DC source voltage changes from 0.993 p.u. to 0.985 p.u. As illustrated by Fig. 2-13 (c), the small shift of the DC source voltage leads to a significantly large variation of the DC-link current of the CDVC-based TLSVC. In contrast, the DC-link voltage of the converter first drops rapidly after the disturbance, and soon increases to its nominal value. Because of the effects of the CDVC, the change of the DC-link voltage of the TLVSC is quite small during the transient process. Fig. 2-13 (e) and (f) show the dynamic responses of the droop-based TLSVC when the reference active power changes from 1 p.u. to 0.75 p.u. Compared with Fig. 2-13 (a) and (e), it is found that the DC-link oscillations can be suppressed by introducing the power-voltage droop element. Besides, it is illustrated by Fig. 2-13 (b) and (e) that the deviations of the DC-link voltage are also reduced by the droop control. As illustrated by Fig.

2-13, the dynamic responses of the TLVSC with the proposed model marked as the dashed red line are aligned with the simulation results marked as the solid black line no matter the control mode, which verifies the accuracy of the proposed TLVSC models under small perturbations.

Fig. 2-14 illustrates the responses of the TLVSC under different control modes when a metallic fault happens at the beginning of the DC transmission line. Fig. 2-14 (a) and (b) are the dynamics of the DC-link current and the capacitor voltage of the CPC-based TLVSC. As illustrated by Fig. 2-14 (a), the DC-link current increases fast after the occurrence of the DC fault. The increasing speed of the fault current can almost maintain constant within the capacitor discharging stage, which is around several milliseconds after the DC fault. In addition, the DC-link voltage remains relatively high at the initial fault period due to the support of the DC-link capacitor, as illustrated by Fig. 2-14 (b). Fig. 2-14 (c) and (d) depict the fault responses of the CDVC-based TLVSC, which are quite similar to those of the CPC-based TLVSC. Compared with Fig. 2-14 (a) and (c), it is observed that the fault current of the CDVC-based TLVSC is slightly larger than that of the CPC-based one. This is because the capacitor voltage with the CDVC decreases slower than that with the CPC, which can be referred to in Fig. 2-14 (b) and (d), and the capacitor discharging current becomes smaller. As for the droop-based TLVSC, the change of the DC-link current is in between that of the CPC-based and the CDVC-based TLVSCs, as illustrated by Fig. 2-14 (e). Similarly, it is indicated by Fig. 2-14 (f) that the dropping speed of the capacitor voltage of the droop-based converter is also between that of the CPC-based and the CDVC-based ones.

Compared with Fig. 2-12 and Fig. 2-14, it is found that the fault characteristics of the LCC and the VSC are distinct. The fault current of the LCC is effectively regulated by the constant current control, while that of the TLVSC is mainly contributed by the capacitor discharging current, which can be much larger than the LCC. In addition, the DC-link voltage of the LCC drops fast by the constant current control to avoid overcurrent. In contrast, the DC-link capacitor of the TLVSC can support the DC-link voltage within the initial fault period. It is illustrated by Fig. 2-14 that the capacitor voltage of the TLVSC under different control modes keeps above 0.8 p.u. within 5 ms after the DC fault. Accordingly, the proposed TLVSC models obtained via the small-signal analysis are valid under DC faults. As illustrated by Fig. 2-14, the fault responses with the proposed model are almost the same as the simulation results, manifesting the effectiveness of the proposed TLVSC models for DC fault analysis.

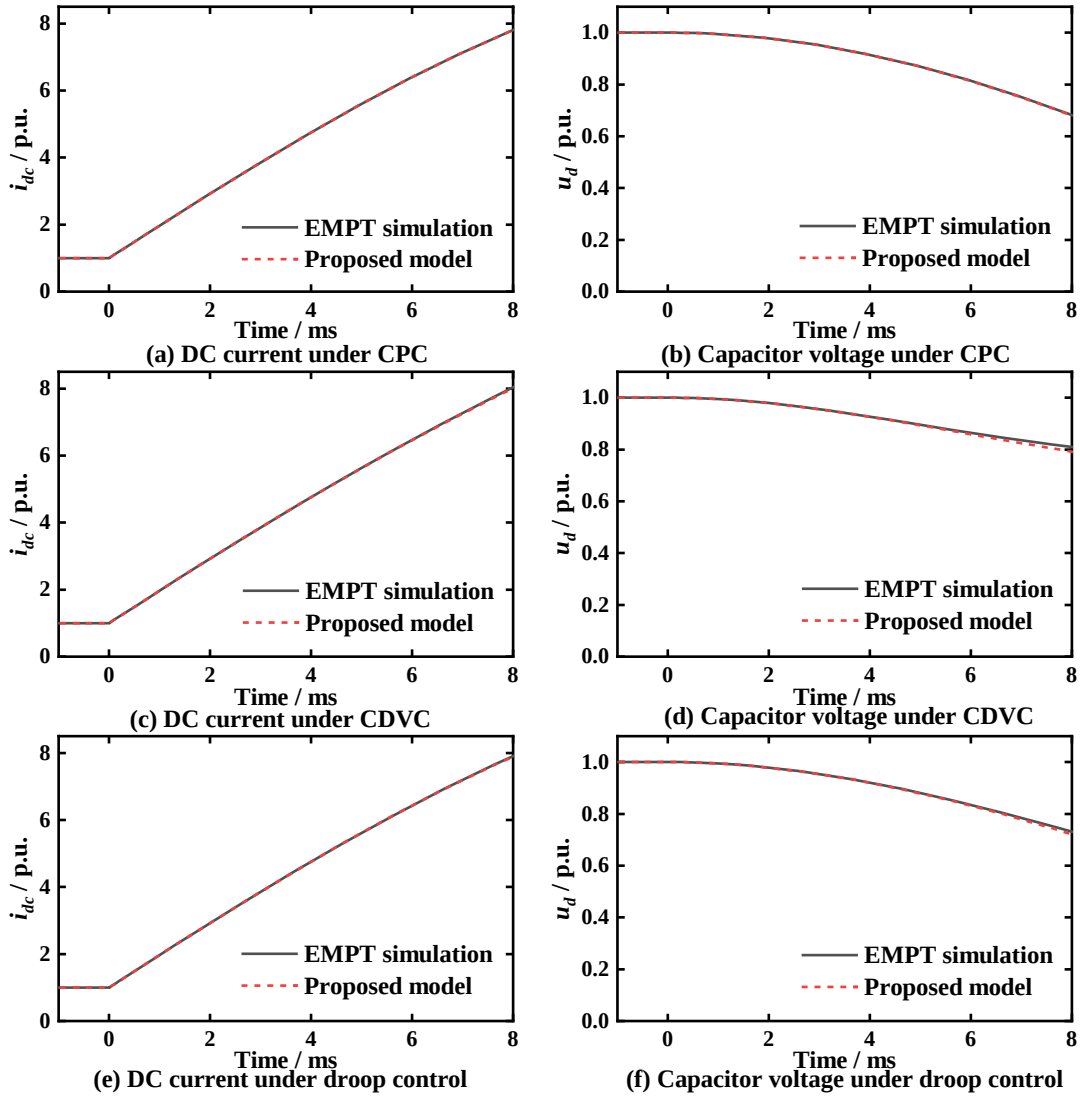


Fig. 2-14 Dynamics of the TLVSC under DC faults.

### 2.5.3 MMC Under Different Control Modes

Fig. 2-15 depicts the dynamic responses of the MMC under small disturbances. When the reference active power of the CPC-based MMC decreases from 1 p.u. to 0.75 p.u., divergent oscillations appear in the DC-link current, as illustrated by Fig. 2-15 (a). Fig. 2-15 (b) depicts the corresponding dynamics of the DC-link voltage, which also exhibit damped oscillations in a relatively smaller range. Fig. 2-15 (c) and (d) are the change of the DC-link current and voltage of the CDVC-based MMC when the DC source voltage drops from 0.993 p.u. to 0.985 p.u. It is observed that the terminal voltage of the converter maintains quite near the nominal value by the CDVC, while the DC-link current can drastically change under DC voltage alternations. Fig. 2-15 (e) and (f) are the dynamic responses of the droop-based MMC. Compared with the dynamics of the CPC-based MMC, it is indicated that the droop element

can effectively suppress the oscillation in the DC link.

Additionally, the dynamic responses of the MMC shown in Fig. 2-15 are analogous to those of the TLVSC shown in Fig. 2-13, indicating the MMC and the TLVSC have similar external characteristics. The current and voltage curves with the EMTP simulation slightly vibrate around those with the proposed model, verifying the accuracy of the proposed MMC models under small perturbations.

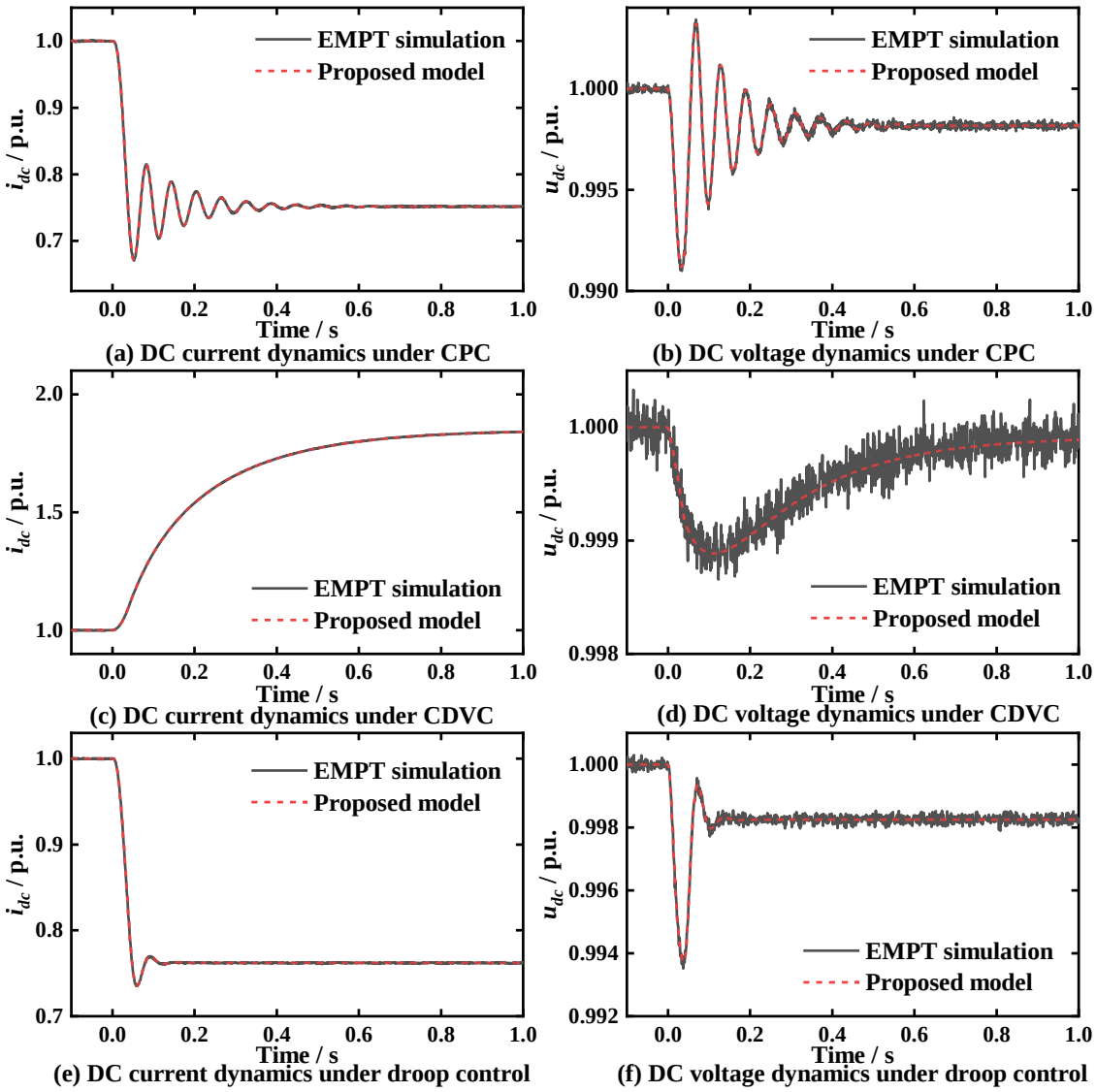


Fig. 2-15 Dynamics of the MMC under small perturbations.

Fig. 2-16 illustrates the fault responses of the MMC under different control modes when a metallic fault happens at the beginning of the DC transmission line. As illustrated by Fig. 2-16 (a), (c), and (e), the DC-link current increases fast with a similar rising speed under different control modes. In contrast, the discharging speed of the capacitors shows more apparent differences under the CPC, CDVC, and droop control, as depicted in Fig. 2-16 (b), (d), and

(e). Nevertheless, the total capacitor voltage of the MMC remains above 0.8 p.u. within 5 ms after the DC fault under different control modes, which makes the linearized models applicable to the fault scenarios. It is also observed in Fig. 2-16 that the simulation results marked as the solid black line almost coincide with the curves with the proposed model marked as the dashed red line, which manifests that the proposed MMC models under different control modes are accurate for the initial DC fault analysis.

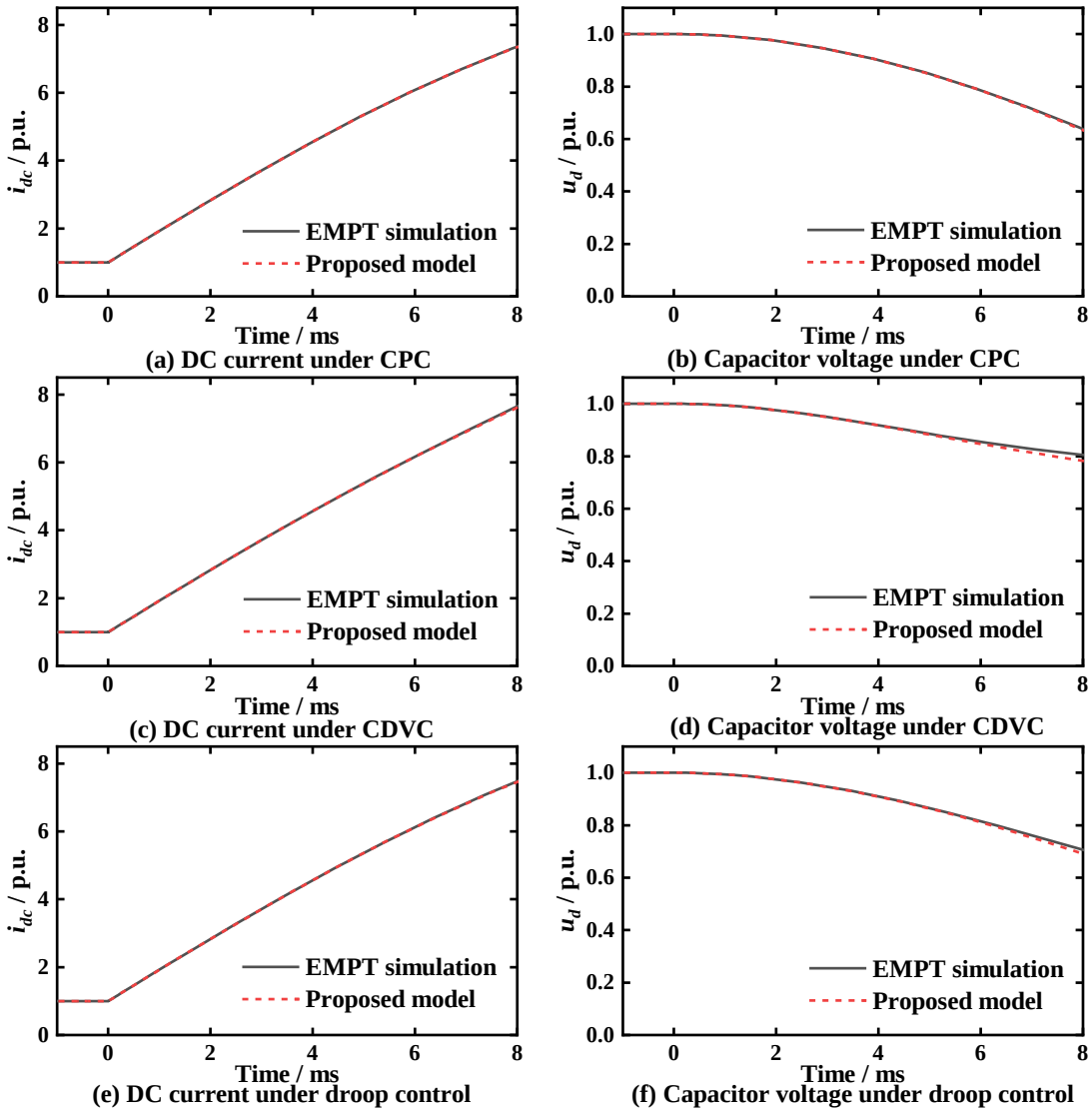


Fig. 2-16 Dynamics of the MMC under DC faults.

## 2.6 Summary

The DC-side dynamic analysis models of the LCC, TLVSC, and MMC are derived in this chapter. Depending on the DC-link voltage derivations of the LCC during disturbances, the small-signal analysis and the least squares approximation are utilised to deduce the linearized

model of the LCC, respectively. It is found that the LCC under small perturbations and DC faults can be equivalent to a similar RLC circuit with different parameters. Considering the DC-link voltage drop of the TLVSC is relatively small during the initial DC fault period, the small-signal model of the TLVSC is valid for the DC fault analysis. Accordingly, the TLVSC models under the CPC, CDVC, and droop control are derived based on the small-signal analysis, which can apply to different sizes of disturbances. As for the MMC, it is found that the external characteristics of the MMC are similar to those of the TLVSC, and thus the MMC models under three control modes are deduced in analogous to the TLVSC. In addition, it is indicated that the LCC, TLVSC, and MMC, with the consideration of control effects, can be equivalent to simple RLC circuits for dynamic analysis. Simulation studies have validated the accuracy of the derived linear models of the converters.

# 3 DC Fault Calculation of Generic MTDC Systems Based on State-Space Method

## 3.1 Introduction

Fault calculation forms a critical part of the dynamic analysis of power systems. Faults on DC networks can be classified into pole-to-pole short-circuit faults, pole-to-ground short-circuit faults, single-pole breaking-line faults, and double-pole breaking-line faults. Since pole-to-pole short-circuit faults generate the strongest impacts on the entire system and are recognized as the most dangerous ones, this thesis mainly focuses on this type of fault. In MTDC systems, the fault line must be cut off within the short capacitor discharging stage to avoid overcurrent damaging the vulnerable switching valves in converters. Therefore, fault characteristics in the initial fault period are of more interest to the DC network. The results of short-circuit calculation during the initial fault period can provide important guidance for proper sizing of power devices, such as DC circuit breakers (CBs) and supplementary DC reactors, and designing protection schemes in MTDC systems.

During a DC fault, all converters in the system can simultaneously inject current to the fault point. The coupling effects of multiple converters make the fault current calculation in a DC network difficult. So far, most works on the fault calculation of MTDC systems rely on EMTP simulation. In [45] and [50], the fault characteristics of TLVSC- and MMC-MTDC systems are investigated based on numerical simulation, respectively. To boost the calculation efficiency, a fault calculation method for MMC-MTDC systems based on the companion circuit method is proposed in [52]. As for the hybrid MTDC system that contains both LCC(s) and VSC(s), [53] establishes a detailed transient simulation mode of China Wudongde HVDC project, an LCC-MMC three-terminal HVDC transmission system to study the faul properties of the system. In [55], the transient simulation model of a two-terminal LCC-MMC system is established based on the dynamic phasor to reduce the model complexity. However, transient-simulation-based fault calculation can only investigate a limited number of selected fault scenarios. In addition, detailed parameters of extensive devices and transmission lines are required to form the simulation model of the studied system.

To tackle the shortcomings of the simulation-based fault analysis method, some researchers resolve to the state-space method. The state-space equation of the MMC-MTDC network is derived in [63], so that the fault current of the entire DC network is calculated by

solving the state-space equation. However, MMCs are regarded as an RLC series circuit, while the control effects are neglected. An improved fault current calculation method for MMC-MTDC systems is reported in [66], which takes the outer loop control of MMCs into account. Unfortunately, it is assumed that all MMCs in the system adopt the CDVC, while actual MTDC systems usually adopt the master-slave or droop-based scheme. Moreover, the inner control is neglected in this work, which can have greater influences on the fault current than the outer loop in the short initial fault period.

Existing state-space-based fault calculation methods can only apply to MTDC systems containing a single type of converter with a fixed control mode. In this chapter, a short-circuit current calculation method for generic MTDC systems is proposed. On the basis of the linear converters models derived in the last chapter, the superposition principle is utilised on the linear systems to facilitate the calculation. The system equation of the fault component network is formed by incorporating the state-space representations of converters and the DC network. After eliminating the nonstate variables, the state-space equation of the fault component network is derived, and the short-circuit current of the entire network can be solved. The proposed method can not only deal with converters with different topologies and control modes but also achieves higher accuracy than existing state-space-based fault analysis methods.

## 3.2 Fault Component Network of Generic MTDC Systems

In a generic MTDC system, the numbers of branches, nodes, and converters are denoted by $B$, $N$, and $M$, respectively. In total, the MTDC system contains $M_1$ LCC-based rectifiers, $M_2$ CPC-based TLVSCs, $M_3$ CDVC/droop-based TLVSCs, $M_4$ CPC-based MMCs, and $M_5$ CDVC/droop-based MMCs. Obviously, $M_1 + M_2 + M_3 + M_4 + M_5 = M$. For the convenience of analysis, the numbering of nodes is in accordance with the following rule.

$$\begin{cases} 1 \text{ to } M_1: & \text{nodes connected to LCCs} \\ (M_1+1) \text{ to } (M_1+M_2): & \text{nodes connected to CPC-based TLVSCs} \\ (M_1+M_2+1) \text{ to } (M_1+M_2+M_3): & \text{nodes connected to CDVC/droop-based TLVSCs} \\ (M_1+M_2+M_3+1) \text{ to } (M_1+M_2+M_3+M_4): & \text{nodes connected to CPC-based MMCs} \\ (M_1+M_2+M_3+M_4+1) \text{ to } M: & \text{nodes connected to CDVC/droop-based MMCs} \\ (M+1) \text{ to } N: & \text{nodes does not connected to any converters (virtual nodes)} \end{cases}$$

For the system incorporating a DC fault, the fault point is marked as Node 0. Accordingly, the numbers of branches and nodes of the faulted MTDC system become ($B$+1) and ($N$+1),

respectively.

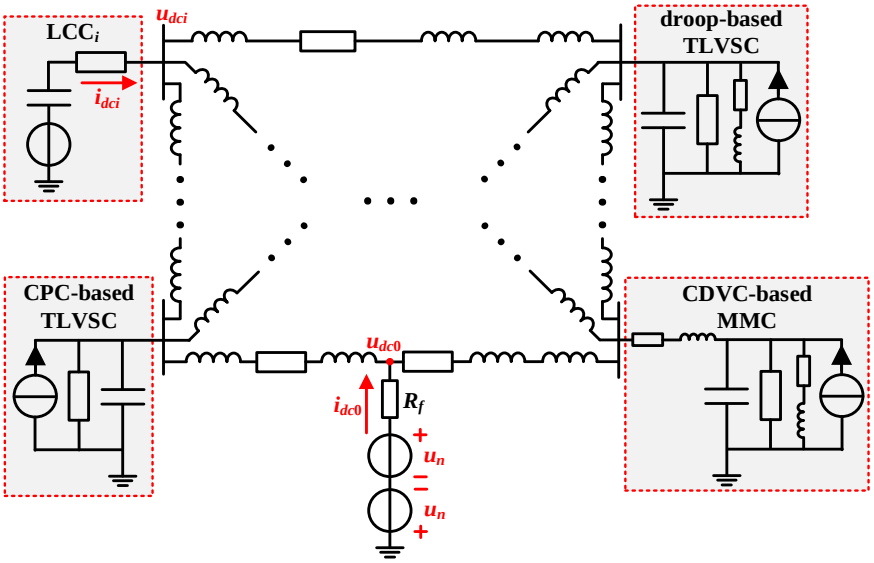


**(a) RLC circuit of the generic faulted MTDC system**

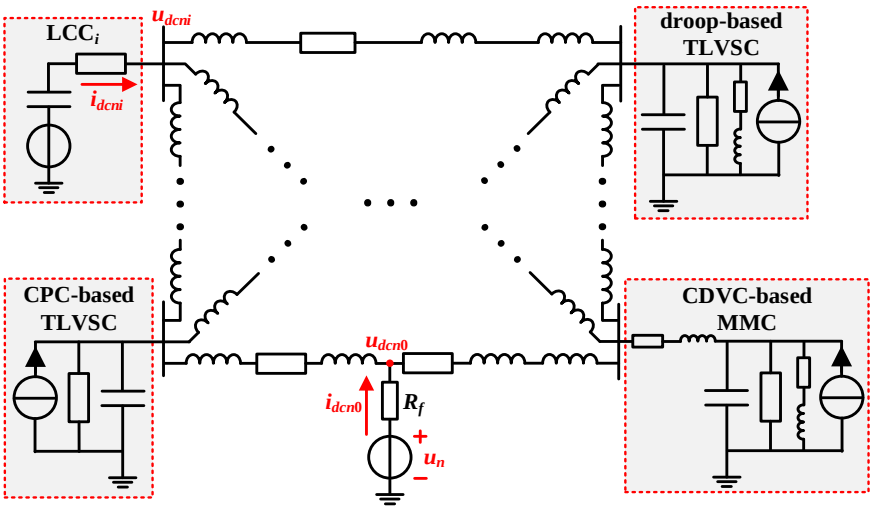


**(b) Normal operation network of the generic MTDC system**

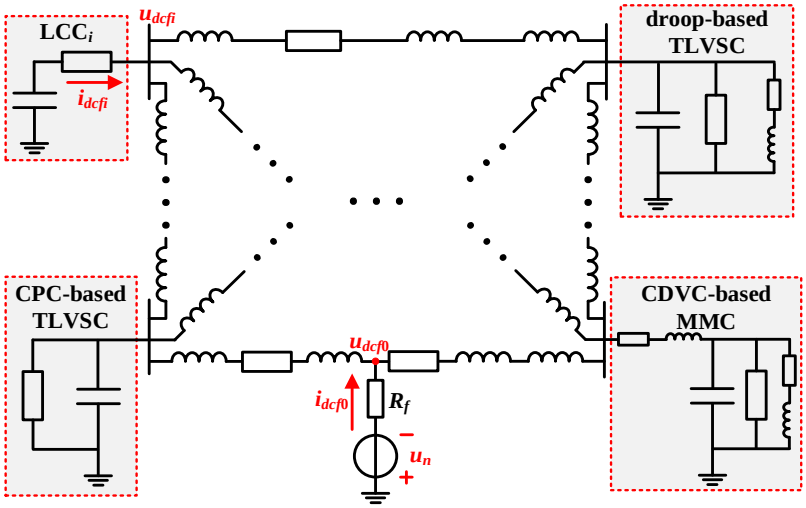


**(c) Fault component network of the generic MTDC system**

Fig. 3-1 Decomposition of the generic MTDC system under a DC fault.

As discussed in the last chapter, the derived fault analysis models of various converters are linear. Considering DC lines are represented by the RL model shown in Fig. 3-1, the entire MTDC system is a linear system. Therefore, the classic superposition principle is applied to facilitate the analysis. As illustrated by Fig. 3-1, the original MTDC system with a DC fault is decomposed into a normal operation network and a fault component network. The electrical quantities on the three networks satisfy the following relations.

$$\begin{cases} u = u_n + u_f \\ i = i_n + i_f \end{cases} \tag{3-1}$$

where $u$ and $i$ represent the voltage and current of the studied system, individually. The subscript $n$ and $f$ denote the normal operation component (pre-fault steady-state value) and the fault component value, respectively.

As illustrated by Fig. 3-1 (c), the fault component network contains only one active source, which makes the fault analysis on this network much easier. In addition, since DC supplementary reactors are installed at the terminal of the transmission line, they are not included in the converter model, but incorporated into the DC network instead.

## 3.3 State-Space Representation of Converters

In this section, the converters models derived in the last chapter are transferred into the state-space representation to form the state-space equation of the fault component network. As per the equivalent circuit model of the LCC-based rectifier depicted in Fig. 2-3, the LCC equations in a state-space form are written as,

$$\begin{cases} C_{eqi}^{LCC} \dfrac{\mathrm{d}u_{dfi}}{\mathrm{d}t} = -i_{dcfi} \\ u_{dfi} - u_{dcfi} = R_{eqi}^{LCC} i_{dcfi} \end{cases}, \quad i = 1, \cdots, M_1 \tag{3-2}$$

where $u_d$ is the voltage of the equivalent capacitor $C_{eq}^{LCC}$. $u_{dc}$ and $i_{dc}$ are the node voltage and the injected current into the node. Subscript $i$ denotes electrical quantities related to Node $i$.

Similarly, the state-space representation of the CPC-based TLVSC is deduced based on the equivalent circuit depicted in Fig. 2-6, which is written as,

$$\begin{cases} C_{ci} \dfrac{\mathrm{d}u_{dfi}}{\mathrm{d}t} = -\dfrac{1}{R_{eqi}^{VSC}} u_{dfi} - i_{dcfi} \\ u_{dfi} - u_{dcfi} = 0 \end{cases}, \quad i = \left(M_1 + 1\right), \cdots, \left(M_1 + M_2\right) \tag{3-3}$$

As for the CDVC/droop-based TLVSC, one RL series branch should be supplemented to

reflect the control effects, as shown in Fig. 2-7. Accordingly, the equations of the CDVC/droop-based TLVSC are given as,

$$\begin{cases} C_{ci}\dfrac{\mathrm{d}u_{dfi}}{\mathrm{d}t} = -\dfrac{1}{R_{eqpi}^{VSC}}u_{dfi} + i_{eqfi} - i_{dcfi} \\ L_{eqi}^{VSC}\dfrac{\mathrm{d}i_{eqfi}}{\mathrm{d}t} = -u_{dfi} - R_{eqsi}^{VSC}i_{eqfi} \\ u_{dfi} - u_{dcfi} = 0 \end{cases}, \quad i = \left(M_1 + M_2 + 1\right), \cdots, \left(M_1 + M_2 + M_3\right) \tag{3-4}$$

where $i_{eq}$ is the current flowing through the equivalent RL series branch.

In (3-3) and (3-4), the voltage of the DC-link capacitor and that of the node are equal. However, both variables are reserved to make the equation has a similar form to the equations of the LCC as expressed by (3-2).

Different from TLVSCs, the DC-link capacitor and the node are connected via an equivalent arm inductor $L_M$ as shown in Fig. 2-10. Accordingly, one equation should be added to express the dynamics in the arm. According to Fig. 2-10 (a), the state-space representation of the CPC-based MMC is written as,

$$\begin{cases} C_{Mi}\dfrac{\mathrm{d}u_{dfi}}{\mathrm{d}t} = -\dfrac{1}{R_{eqi}^{VSC}}u_{dfi} - i_{dcfi} \\ L_{Mi}\dfrac{\mathrm{d}i_{dcfi}}{\mathrm{d}t} = u_{dfi} - u_{dcfi} - R_{Mi}i_{dcfi} \end{cases}, \quad i = \left(M_1 + M_2 + M_3 + 1\right), \cdots, \left(M_1 + M_2 + M_3 + M_4\right) \tag{3-5}$$

According to Fig. 2-10 (b), the equations of the CDVC/droop-based MMC are written as,

$$\begin{cases} C_{Mi}\dfrac{\mathrm{d}u_{fi}}{\mathrm{d}t} = -\dfrac{1}{R_{eqi}^{VSC}}u_{dfi} + i_{eqfi} - i_{dcfi} \\ L_{eqi}^{VSC}\dfrac{\mathrm{d}i_{eqfi}}{\mathrm{d}t} = -u_{dfi} - R_{eqsi}^{VSC}i_{eqfi} \\ L_{Mi}\dfrac{\mathrm{d}i_{dcfi}}{\mathrm{d}t} = u_{dfi} - u_{dcfi} - R_{Mi}i_{dcfi} \end{cases}, \quad i = \left(M_1 + M_2 + M_3 + M_4\right), \cdots, M \tag{3-6}$$

## 3.4 State-Space Representation of the DC Network

For simplicity, the classic RL model is utilised to represent the DC transmission line. For Branch *ij* that connects Node *i* and Node *j*, its dynamics can be expressed as follows according to Kirchhoff voltage law (KVL).

$$L_{bij}\frac{\mathrm{d}i_{bfij}}{\mathrm{d}t} = -R_{bij}i_{bfij} + u_{dcfi} - u_{dcfj} \tag{3-7}$$

where $L_{bij}$ and $R_{bij}$ are the equivalent inductance and resistance of the branch that connects Node $i$ and Node $j$, respectively. Note that $L_{bij}$ consists of the line inductance $L_l$ and the inductance of the supplementary reactor $L_d$ or $L_T$. $i_{bfij}$ is the fault component current flowing through Branch $ij$. For the whole network, (3-7) is rewritten in a compact form as,

$$\boldsymbol{L}_b \frac{\mathrm{d}\boldsymbol{i}_{bf}}{\mathrm{d}t} = -\boldsymbol{R}_b \boldsymbol{i}_{bf} + \hat{\boldsymbol{A}} \boldsymbol{u}_{dcf} \tag{3-8}$$

where $\boldsymbol{L_b} = \mathrm{diag}\{L_{b1}, L_{b2}, \cdots, L_{b(B+1)}\}$, $\boldsymbol{R_b} = \mathrm{diag}\{R_{b1}, R_{b2}, \cdots, R_{b(B+1)}\}$, $\boldsymbol{i_{bf}} = [i_{bf1}, i_{bf2}, \cdots, i_{bf(B+1)}]^T$, $\boldsymbol{u_{dcf}} = [u_{dcf0}, u_{dcf1}, \cdots, u_{dcfN}]^T$. $\hat{\boldsymbol{A}}$ is the branch-to-node incidence matrix of the network under the DC fault, containing ($B$+1) rows and ($N$+1) columns. The entities of $\hat{\boldsymbol{A}}$ are given as,

$$\hat{a}_{ij} = \begin{cases} 0, & \text{Branch } i \text{ does not connect to Node } j \\ 1, & \text{Branch } i \text{ directes from Node } j \\ -1, & \text{Branch } i \text{ directes to Node } j \end{cases} \tag{3-9}$$

In addition, the following equation holds at the fault point.

$$-u_n - u_{dcf\,0} = R_f i_{idcf\,0} \tag{3-10}$$

where $R_f$ is the fault resistance. During normal operation, the voltage of the network is close to the nominal voltage denoted by $u_n$, and thereby the pre-fault voltage at the fault point is assumed as $u_n$ in (3-10).

According to KCL, the algebraic sum of the current injecting into each node is 0, yielding,

$$\hat{\boldsymbol{A}}^T \boldsymbol{i}_{bf} = \boldsymbol{i}_{dcf} \tag{3-11}$$

where $\boldsymbol{i_{dcf}} = [i_{dcf0}, i_{dcf1}, \cdots, i_{dcfN}]^T$. Since there is no converter connecting with virtual nodes, the injected current into Node $M$+1 to Node $N$ is 0. Thus, $\boldsymbol{i_{dcf}} = [i_{dcf0}, i_{dcf1}, \cdots, i_{dcfM}, \boldsymbol{0}_{1\times(N-M)}]^T$.

## 3.5 Short-Circuit Current Calculation of the Fault Network Based on State-Space Method

### 3.5.1 System Equation of the Fault Component Network

The system equation of the fault component network is obtained by synthesizing the converter equations and the network equations. The state-space representation of converters expressed by (3-2), (3-3), (3-4), (3-5), and (3-6) are rewritten in a compact form as,

$$\boldsymbol{C}_c \frac{\mathrm{d}\boldsymbol{u}_{df}}{\mathrm{d}t} = -\boldsymbol{g}_d \boldsymbol{u}_{df} + \boldsymbol{K}_{ieq}^T \boldsymbol{i}_{eqf} - \left[\boldsymbol{i}_{dcf}^{(1)}, \boldsymbol{i}_{dcf}^{(2)}\right]^T \tag{3-12}$$

$$\boldsymbol{L}_{eq} \frac{\mathrm{d}\boldsymbol{i}_{eqf}}{\mathrm{d}t} = -\boldsymbol{K}_{ieq} \boldsymbol{u}_{df} + \boldsymbol{R}_{eqs} \boldsymbol{i}_{eqf} \tag{3-13}$$

$$\boldsymbol{L}_{\boldsymbol{M}}\frac{\mathrm{d}\boldsymbol{i}_{\boldsymbol{dcf}}^{(2)}}{\mathrm{d}t}=\boldsymbol{K}_{\boldsymbol{idc}}\boldsymbol{u}_{\boldsymbol{df}}-\boldsymbol{R}_{\boldsymbol{M}}\boldsymbol{i}_{\boldsymbol{dcf}}^{(2)}-\boldsymbol{u}_{\boldsymbol{dcf}}^{(2)} \tag{3-14}$$

$$\boldsymbol{u}_{\boldsymbol{dcf}}^{(1)}=\boldsymbol{K}_{\boldsymbol{u}}\boldsymbol{u}_{\boldsymbol{df}}-\boldsymbol{R}_{\boldsymbol{eq}}\boldsymbol{i}_{\boldsymbol{dcf}}^{(1)} \tag{3-15}$$

where,

$$\boldsymbol{u}_{\boldsymbol{df}}=\left[u_{df1},u_{df2},\cdots,u_{dfM}\right]^T,\quad \boldsymbol{u}_{\boldsymbol{dcf}}=\left[u_{dcf0},\boldsymbol{u}_{\boldsymbol{dcf}}^{(1)},\boldsymbol{u}_{\boldsymbol{dcf}}^{(2)},\boldsymbol{u}_{\boldsymbol{dcf}}^{(3)}\right]^T,$$

$$\boldsymbol{u}_{\boldsymbol{dcf}}^{(1)}=\left[u_{dcf1},\cdots,u_{dcf(M_1+M_2+M_3)}\right]^T,\boldsymbol{u}_{\boldsymbol{dcf}}^{(2)}=\left[u_{dcf(M_1+M_2+M_3+1)},\cdots,u_{dcfM}\right]^T,\boldsymbol{u}_{\boldsymbol{dcf}}^{(3)}=\left[u_{dcf(M+1)},\cdots,u_{dcfN}\right]^T,$$

$$\boldsymbol{i}_{\boldsymbol{dcf}}^{(1)}=\left[i_{dcf1},i_{dcf2},\cdots,i_{dcf(M_1+M_2+M_3)}\right]^T,\boldsymbol{i}_{\boldsymbol{dcf}}^{(2)}=\left[i_{dcf(M_1+M_2+M_3+1)},i_{dcf(M_1+M_2+M_3+2)},\cdots,i_{dcfM}\right]^T,$$

$$\boldsymbol{i}_{\boldsymbol{eqf}}=\left[i_{eqf(M_1+M_2+1)},\cdots,i_{eqf(M_1+M_2+M_3)},i_{eqf(M-M_5+1)},\cdots,i_{eqfM}\right]^T,$$

$$\boldsymbol{C}_{\boldsymbol{c}}=\mathrm{diag}\left\{C_{eq1}^{LCC},\cdots,C_{eqM_1}^{LCC},C_{c(M_1+1)},\cdots,C_{c(M_1+M_2+M_3)},C_{M(M_1+M_2+M_3+1)},\cdots,C_{MM}\right\},$$

$$\boldsymbol{g}_{\boldsymbol{d}}=\mathrm{diag}\{\underbrace{0,\cdots,0}_{M_1},1/R_{eq(M_1+1)}^{VSC},\cdots,1/R_{eqpM}^{VSC}\},\quad \boldsymbol{R}_{\boldsymbol{eq}}=\mathrm{diag}\{R_{eq1}^{LCC},\cdots,R_{eqM_1}^{LCC},\underbrace{0,\cdots,0}_{M_2+M_3}\},$$

$$\boldsymbol{L}_{\boldsymbol{eq}}=\mathrm{diag}\left\{L_{eq(M_1+M_2+1)}^{VSC},\cdots,L_{eq(M_1+M_2+M_3)}^{VSC},L_{eq(M-M_5+1)}^{VSC},\cdots,L_{eqM}^{VSC}\right\},$$

$$\boldsymbol{R}_{\boldsymbol{eqs}}=\mathrm{diag}\left\{R_{eqs(M_1+M_2+1)}^{VSC},\cdots,R_{eqs(M_1+M_2+M_3)}^{VSC},R_{eqs(M-M_5+1)}^{VSC},\cdots,R_{eqsM}^{VSC}\right\},$$

$$\boldsymbol{L}_{\boldsymbol{M}}=\mathrm{diag}\left\{L_{M(M_1+M_2+M_3+1)},\cdots,L_{MM}\right\},\quad \boldsymbol{R}_{\boldsymbol{M}}=\mathrm{diag}\left\{R_{M(M_1+M_2+M_3+1)},\cdots,R_{MM}\right\},$$

$$\boldsymbol{K}_{\boldsymbol{ieq}}=\begin{bmatrix}\boldsymbol{0}_{\boldsymbol{M_3}\times(\boldsymbol{M_1}+\boldsymbol{M_2})} & \boldsymbol{I}_{\boldsymbol{M_3}\times\boldsymbol{M_3}} & \boldsymbol{0}_{\boldsymbol{M_3}\times\boldsymbol{M_4}} & \boldsymbol{0}_{\boldsymbol{M_3}\times\boldsymbol{M_5}}\\ \boldsymbol{0}_{\boldsymbol{M_5}\times(\boldsymbol{M_1}+\boldsymbol{M_2})} & \boldsymbol{0}_{\boldsymbol{M_5}\times\boldsymbol{M_3}} & \boldsymbol{0}_{\boldsymbol{M_5}\times\boldsymbol{M_4}} & \boldsymbol{I}_{\boldsymbol{M_5}\times\boldsymbol{M_5}}\end{bmatrix},$$

$$\boldsymbol{K}_{\boldsymbol{idc}}=\left[\boldsymbol{0}_{(\boldsymbol{M_4}+\boldsymbol{M_5})\times(\boldsymbol{M_1}+\boldsymbol{M_2}+\boldsymbol{M_3})},\boldsymbol{I}_{(\boldsymbol{M_4}+\boldsymbol{M_5})\times(\boldsymbol{M_4}+\boldsymbol{M_5})}\right],\ \boldsymbol{K}_{\boldsymbol{u}}=\left[\boldsymbol{I}_{(\boldsymbol{M_1}+\boldsymbol{M_2}+\boldsymbol{M_3})\times(\boldsymbol{M_1}+\boldsymbol{M_2}+\boldsymbol{M_3})},\boldsymbol{0}_{(\boldsymbol{M_4}+\boldsymbol{M_5})\times(\boldsymbol{M_1}+\boldsymbol{M_2}+\boldsymbol{M_3})}\right].$$

As for the network equation, (3-8) and (3-11) can be partitioned as follows.

$$\begin{bmatrix}L_{b1} & & & \\ & \boldsymbol{L}_{\boldsymbol{b}}^{(2)} & & \\ & & \boldsymbol{L}_{\boldsymbol{b}}^{(3)} & \\ & & & \boldsymbol{L}_{\boldsymbol{b}}^{(4)}\end{bmatrix}\frac{\mathrm{d}}{\mathrm{d}t}\begin{bmatrix}i_{bf1}\\ \boldsymbol{i}_{\boldsymbol{bf}}^{(2)}\\ \boldsymbol{i}_{\boldsymbol{bf}}^{(3)}\\ \boldsymbol{i}_{\boldsymbol{bf}}^{(4)}\end{bmatrix}=-\begin{bmatrix}R_{b1} & & & \\ & \boldsymbol{R}_{\boldsymbol{b}}^{(2)} & & \\ & & \boldsymbol{R}_{\boldsymbol{b}}^{(3)} & \\ & & & \boldsymbol{R}_{\boldsymbol{b}}^{(4)}\end{bmatrix}\begin{bmatrix}i_{bf1}\\ \boldsymbol{i}_{\boldsymbol{bf}}^{(2)}\\ \boldsymbol{i}_{\boldsymbol{bf}}^{(3)}\\ \boldsymbol{i}_{\boldsymbol{bf}}^{(4)}\end{bmatrix}+\begin{bmatrix}\hat{A}_{11} & \hat{\boldsymbol{A}}_{\boldsymbol{12}} & \hat{\boldsymbol{A}}_{\boldsymbol{13}} & \hat{\boldsymbol{A}}_{\boldsymbol{14}}\\ \hat{\boldsymbol{A}}_{\boldsymbol{21}} & \hat{\boldsymbol{A}}_{\boldsymbol{22}} & \hat{\boldsymbol{A}}_{\boldsymbol{23}} & \hat{\boldsymbol{A}}_{\boldsymbol{24}}\\ \hat{\boldsymbol{A}}_{\boldsymbol{31}} & \hat{\boldsymbol{A}}_{\boldsymbol{32}} & \hat{\boldsymbol{A}}_{\boldsymbol{33}} & \hat{\boldsymbol{A}}_{\boldsymbol{34}}\\ \hat{\boldsymbol{A}}_{\boldsymbol{41}} & \hat{\boldsymbol{A}}_{\boldsymbol{42}} & \hat{\boldsymbol{A}}_{\boldsymbol{43}} & \hat{\boldsymbol{A}}_{\boldsymbol{44}}\end{bmatrix}\begin{bmatrix}u_{dcf0}\\ \boldsymbol{u}_{\boldsymbol{dcf}}^{(1)}\\ \boldsymbol{u}_{\boldsymbol{dcf}}^{(2)}\\ \boldsymbol{u}_{\boldsymbol{dcf}}^{(3)}\end{bmatrix} \tag{3-16}$$

$$\begin{bmatrix}\hat{A}_{11}^T & \hat{\boldsymbol{A}}_{\boldsymbol{21}}^{\boldsymbol{T}} & \hat{\boldsymbol{A}}_{\boldsymbol{31}}^{\boldsymbol{T}} & \hat{\boldsymbol{A}}_{\boldsymbol{41}}^{\boldsymbol{T}}\\ \hat{\boldsymbol{A}}_{\boldsymbol{12}}^{\boldsymbol{T}} & \hat{\boldsymbol{A}}_{\boldsymbol{22}}^{\boldsymbol{T}} & \hat{\boldsymbol{A}}_{\boldsymbol{32}}^{\boldsymbol{T}} & \hat{\boldsymbol{A}}_{\boldsymbol{42}}^{\boldsymbol{T}}\\ \hat{\boldsymbol{A}}_{\boldsymbol{13}}^{\boldsymbol{T}} & \hat{\boldsymbol{A}}_{\boldsymbol{23}}^{\boldsymbol{T}} & \hat{\boldsymbol{A}}_{\boldsymbol{33}}^{\boldsymbol{T}} & \hat{\boldsymbol{A}}_{\boldsymbol{43}}^{\boldsymbol{T}}\\ \hat{\boldsymbol{A}}_{\boldsymbol{14}}^{\boldsymbol{T}} & \hat{\boldsymbol{A}}_{\boldsymbol{24}}^{\boldsymbol{T}} & \hat{\boldsymbol{A}}_{\boldsymbol{34}}^{\boldsymbol{T}} & \hat{\boldsymbol{A}}_{\boldsymbol{44}}^{\boldsymbol{T}}\end{bmatrix}\begin{bmatrix}i_{bf1}\\ \boldsymbol{i}_{\boldsymbol{bf}}^{(2)}\\ \boldsymbol{i}_{\boldsymbol{bf}}^{(3)}\\ \boldsymbol{i}_{\boldsymbol{bf}}^{(4)}\end{bmatrix}=\begin{bmatrix}i_{dcf0}\\ \boldsymbol{i}_{\boldsymbol{dcf}}^{(1)}\\ \boldsymbol{i}_{\boldsymbol{dcf}}^{(2)}\\ \boldsymbol{0}_{(\boldsymbol{N}-\boldsymbol{M})\times\boldsymbol{1}}\end{bmatrix} \tag{3-17}$$

(3-10), (3-12), (3-13), (3-14), (3-15), (3-16), and (3-17) constitute the system equation of the studied fault component MTDC network.

### 3.5.2 Elimination of Nonstate Variables

In the above system equation, only a part of the variables is state variables. In addition, it can be seen from (3-17) that $\boldsymbol{i}_{bf}^{(4)}$ in (3-16) is colinear with $i_{dcf0}$, $\boldsymbol{i}_{bf}^{(2)}$, and $\boldsymbol{i}_{bf}^{(3)}$. Therefore, the nonstate variables elimination should be conducted to formulate the state-space equation of the system.

According to the fourth row in (3-17), $\boldsymbol{i}_{bf}^{(4)}$ is a linear combination of $i_{dcf0}$, $\boldsymbol{i}_{bf}^{(2)}$, and $\boldsymbol{i}_{bf}^{(3)}$,

$$\boldsymbol{i}_{bf}^{(4)} = -\left(\hat{\boldsymbol{A}}_{44}^{T}\right)^{-1}\hat{\boldsymbol{A}}_{14}^{T} i_{bf1} - \left(\hat{\boldsymbol{A}}_{44}^{T}\right)^{-1}\hat{\boldsymbol{A}}_{24}^{T}\boldsymbol{i}_{bf}^{(2)} - \left(\hat{\boldsymbol{A}}_{44}^{T}\right)^{-1}\hat{\boldsymbol{A}}_{34}^{T}\boldsymbol{i}_{bf}^{(3)} \tag{3-18}$$

Substitution of (3-18) into (3-17), it yields that,

$$\begin{bmatrix} i_{dcf0} \\ \boldsymbol{i}_{dcf}^{(1)} \\ \boldsymbol{i}_{dcf}^{(2)} \end{bmatrix} = \begin{bmatrix} \hat{B}_{11} & \hat{\boldsymbol{B}}_{12} & \hat{\boldsymbol{B}}_{13} \\ \hat{\boldsymbol{B}}_{21} & \hat{\boldsymbol{B}}_{22} & \hat{\boldsymbol{B}}_{23} \\ \hat{\boldsymbol{B}}_{31} & \hat{\boldsymbol{B}}_{32} & \hat{\boldsymbol{B}}_{33} \end{bmatrix} \begin{bmatrix} i_{bf1} \\ \boldsymbol{i}_{bf}^{(2)} \\ \boldsymbol{i}_{bf}^{(3)} \end{bmatrix} \tag{3-19}$$

where $\hat{\boldsymbol{B}}_{ij} = \hat{\boldsymbol{A}}_{ji}^{T} - \hat{\boldsymbol{A}}_{4i}^{T}\left(\hat{\boldsymbol{A}}_{44}^{T}\right)^{-1}\hat{\boldsymbol{A}}_{j4}^{T}$.

Combined with (3-10) and (3-19), we have,

$$u_{dfc0} = -R_f \hat{B}_{11} i_{bf1} - R_f \hat{\boldsymbol{B}}_{12}\boldsymbol{i}_{bf}^{(2)} - R_f \hat{\boldsymbol{B}}_{13}\boldsymbol{i}_{bf}^{(3)} - u_n \tag{3-20}$$

$$\boldsymbol{u}_{dcf}^{(1)} = \boldsymbol{K}_u \boldsymbol{u}_{df} - \boldsymbol{R}_{eq}\hat{\boldsymbol{B}}_{21} i_{bf1} - \boldsymbol{R}_{eq}\hat{\boldsymbol{B}}_{22}\boldsymbol{i}_{bf}^{(2)} - \boldsymbol{R}_{eq}\hat{\boldsymbol{B}}_{23}\boldsymbol{i}_{bf}^{(3)} \tag{3-21}$$

Substitution of (3-18) into (3-16), the fourth row of (3-16) turns into an algebraic equation as follows.

$$\hat{\boldsymbol{C}}_{i1} i_{bf1} + \hat{\boldsymbol{C}}_{i2}\boldsymbol{i}_{bf}^{(2)} + \hat{\boldsymbol{C}}_{i3}\boldsymbol{i}_{bf}^{(3)} - \hat{\boldsymbol{C}}_{u0} u_{dcf0} - \hat{\boldsymbol{C}}_{u1}\boldsymbol{u}_{dcf}^{(1)} - \hat{\boldsymbol{C}}_{u2}\boldsymbol{u}_{dcf}^{(2)} - \hat{\boldsymbol{C}}_{u3}\boldsymbol{u}_{dcf}^{(3)} = \boldsymbol{0}_{(N-M)\times 1} \tag{3-22}$$

where,

$$\hat{\boldsymbol{C}}_{i1} = \hat{\boldsymbol{A}}_{14}^{T} L_{b1}^{-1} R_{b1} - \left(\boldsymbol{L}_b^{(4)}\right)^{-1}\boldsymbol{R}_b^{(4)}\hat{\boldsymbol{A}}_{14}^{T}, \quad \hat{\boldsymbol{C}}_{ij} = \hat{\boldsymbol{A}}_{j4}^{T}\left(\boldsymbol{L}_b^{(j)}\right)^{-1}\boldsymbol{R}_b^{(j)} - \left(\boldsymbol{L}_b^{(4)}\right)^{-1}\boldsymbol{R}_b^{(4)}\hat{\boldsymbol{A}}_{j4}^{T}, \quad j = 2,3$$

$$\hat{\boldsymbol{C}}_{u(j\text{-}1)} = \hat{\boldsymbol{A}}_{14}^{T}\hat{\boldsymbol{A}}_{1j} L_{b1}^{-1} + \hat{\boldsymbol{A}}_{24}^{T}\hat{\boldsymbol{A}}_{2j}\left(\boldsymbol{L}_b^{(2)}\right)^{-1} + \hat{\boldsymbol{A}}_{34}^{T}\hat{\boldsymbol{A}}_{3j}\left(\boldsymbol{L}_b^{(3)}\right)^{-1} + \left(\boldsymbol{L}_b^{(4)}\right)^{-1}\hat{\boldsymbol{A}}_{44}^{T}\hat{\boldsymbol{A}}_{4j}, \quad j = 1,2,3,4$$

Similarly, by substituting (3-16) and (3-19) into (3-14), (3-14) becomes an algebraic equation as,

$$\hat{\boldsymbol{D}}_{i1} i_{bf1} + \hat{\boldsymbol{D}}_{i2}\boldsymbol{i}_{bf}^{(2)} + \hat{\boldsymbol{D}}_{i3}\boldsymbol{i}_{bf}^{(3)} - \boldsymbol{L}_M^{-1}\boldsymbol{K}_{idc}\boldsymbol{u}_{df} + \hat{\boldsymbol{D}}_{u0} u_{dcf0} + \hat{\boldsymbol{D}}_{u1}\boldsymbol{u}_{dcf}^{(1)} + \hat{\boldsymbol{D}}_{u2}\boldsymbol{u}_{dcf}^{(2)} + \hat{\boldsymbol{D}}_{u3}\boldsymbol{u}_{dcf}^{(3)} = \boldsymbol{0}_{(M_4+M_5)\times 1} \tag{3-23}$$

where,

$$\hat{\boldsymbol{D}}_{i1}=\boldsymbol{L}_M^{-1}\boldsymbol{R}_M\hat{\boldsymbol{B}}_{31}-\hat{\boldsymbol{B}}_{31}L_{b1}^{-1}R_{b1},\quad \hat{\boldsymbol{D}}_{ij}=\boldsymbol{L}_M^{-1}\boldsymbol{R}_M\hat{\boldsymbol{B}}_{3j}-\hat{\boldsymbol{B}}_{3j}\left(\boldsymbol{L}_b^{(j)}\right)^{-1}\boldsymbol{R}_b^{(j)},\quad j=2,3$$

$$\hat{\boldsymbol{D}}_{u(j\text{-}1)}=\hat{\boldsymbol{B}}_{31}\hat{\boldsymbol{A}}_{1j}L_{b1}^{-1}+\hat{\boldsymbol{B}}_{32}\hat{\boldsymbol{A}}_{2j}\left(\boldsymbol{L}_b^{(2)}\right)^{-1}+\hat{\boldsymbol{B}}_{33}\hat{\boldsymbol{A}}_{3j}\left(\boldsymbol{L}_b^{(3)}\right)^{-1},\quad j=1,2,4$$

$$\hat{\boldsymbol{D}}_{u2}=\hat{\boldsymbol{B}}_{31}\hat{\boldsymbol{A}}_{13}L_{b1}^{-1}+\hat{\boldsymbol{B}}_{32}\hat{\boldsymbol{A}}_{23}\left(\boldsymbol{L}_b^{(2)}\right)^{-1}+\hat{\boldsymbol{B}}_{33}\hat{\boldsymbol{A}}_{33}\left(\boldsymbol{L}_b^{(3)}\right)^{-1}+\boldsymbol{L}_M^{-1}$$

Based on (3-20), (3-21), (3-22), and (3-23), $\boldsymbol{u}_{dcf}^{(2)}$ and $\boldsymbol{u}_{dcf}^{(3)}$ can be expressed by the state variables as follows.

$$\boldsymbol{u}_{dcf}^{(2)}=\hat{\boldsymbol{E}}_{u1}\boldsymbol{u}_{df}+\hat{\boldsymbol{E}}_{i1}i_{bf1}+\hat{\boldsymbol{E}}_{i2}\boldsymbol{i}_{bf}^{(2)}+\hat{\boldsymbol{E}}_{i3}\boldsymbol{i}_{bf}^{(3)}+\hat{\boldsymbol{E}}_{u2}u_n \tag{3-24}$$

$$\boldsymbol{u}_{dcf}^{(3)}=\hat{\boldsymbol{F}}_{u1}\boldsymbol{u}_{df}+\hat{\boldsymbol{E}}_{i1}i_{bf1}+\hat{\boldsymbol{E}}_{i2}\boldsymbol{i}_{bf}^{(2)}+\hat{\boldsymbol{E}}_{i3}\boldsymbol{i}_{bf}^{(3)}+\hat{\boldsymbol{E}}_{u2}u_n \tag{3-25}$$

where,

$$\hat{\boldsymbol{E}}_{u1}=\left(\hat{\boldsymbol{C}}_{u2}-\hat{\boldsymbol{C}}_{u3}\hat{\boldsymbol{D}}_{u3}^{-1}\left(\hat{\boldsymbol{D}}_{u2}+\boldsymbol{L}_M^{-1}\right)\right)^{-1}\left(\hat{\boldsymbol{C}}_{u3}\hat{\boldsymbol{D}}_{u1}\hat{\boldsymbol{D}}_{u3}^{-1}\boldsymbol{K}_u-\hat{\boldsymbol{C}}_{u1}\boldsymbol{K}_u-\hat{\boldsymbol{C}}_{u3}\hat{\boldsymbol{D}}_{u3}^{-1}\boldsymbol{L}_M^{-1}\boldsymbol{K}_{idc}\right),$$

$$\hat{\boldsymbol{E}}_{u2}=\left(\hat{\boldsymbol{C}}_{u2}-\hat{\boldsymbol{C}}_{u3}\hat{\boldsymbol{D}}_{u3}^{-1}\left(\hat{\boldsymbol{D}}_{u2}+\boldsymbol{L}_M^{-1}\right)\right)^{-1}\left(\hat{\boldsymbol{C}}_{u0}-\hat{\boldsymbol{C}}_{u3}\hat{\boldsymbol{D}}_{u3}^{-1}\hat{\boldsymbol{D}}_{u0}\right),$$

$$\begin{aligned}\hat{\boldsymbol{E}}_{ij}=&\left(\hat{\boldsymbol{C}}_{u2}-\hat{\boldsymbol{C}}_{u3}\hat{\boldsymbol{D}}_{u3}^{-1}\left(\hat{\boldsymbol{D}}_{u2}+\boldsymbol{L}_M^{-1}\right)\right)^{-1}\left(\hat{\boldsymbol{C}}_{ij}+\hat{\boldsymbol{C}}_{u3}\hat{\boldsymbol{D}}_{u3}^{-1}\hat{\boldsymbol{D}}_{ij}+\left(\hat{\boldsymbol{C}}_{u0}-\hat{\boldsymbol{C}}_{u3}\hat{\boldsymbol{D}}_{u3}^{-1}\hat{\boldsymbol{D}}_{u0}\right)R_f\hat{\boldsymbol{B}}_{1j}\right.\\&\left.+\left(\hat{\boldsymbol{C}}_{u1}-\hat{\boldsymbol{C}}_{u3}\hat{\boldsymbol{D}}_{u1}\hat{\boldsymbol{D}}_{u3}^{-1}\right)\boldsymbol{R}_{eq}\hat{\boldsymbol{B}}_{2j}\right),\quad j=1,2,3\end{aligned}$$

$$\hat{\boldsymbol{F}}_{u1}=\hat{\boldsymbol{D}}_{u3}^{-1}\boldsymbol{L}_M^{-1}\boldsymbol{K}_{idc}-\hat{\boldsymbol{D}}_{u3}^{-1}\hat{\boldsymbol{D}}_{u1}\boldsymbol{K}_u-\hat{\boldsymbol{D}}_{u3}^{-1}\left(\hat{\boldsymbol{D}}_{u2}+\boldsymbol{L}_M^{-1}\right)\hat{\boldsymbol{E}}_{u1},\quad \hat{\boldsymbol{F}}_{u2}=\hat{\boldsymbol{D}}_{u3}^{-1}\hat{\boldsymbol{D}}_{u0}-\hat{\boldsymbol{D}}_{u3}^{-1}\left(\hat{\boldsymbol{D}}_{u2}+\boldsymbol{L}_M^{-1}\right)\hat{\boldsymbol{E}}_{u2},$$

$$\hat{\boldsymbol{F}}_{ij}=\hat{\boldsymbol{D}}_{u3}^{-1}\hat{\boldsymbol{D}}_{u0}R_f\hat{\boldsymbol{B}}_{1j}+\hat{\boldsymbol{D}}_{u3}^{-1}\hat{\boldsymbol{D}}_{u1}\boldsymbol{R}_{eq}\hat{\boldsymbol{B}}_{2j}-\hat{\boldsymbol{D}}_{u3}^{-1}\hat{\boldsymbol{D}}_{ij}-\hat{\boldsymbol{D}}_{u3}^{-1}\left(\hat{\boldsymbol{D}}_{u2}+\boldsymbol{L}_M^{-1}\right)\hat{\boldsymbol{E}}_{ij},\quad j=1,2,3$$

Combined with (3-20), (3-21), (3-24), and (3-25), $\boldsymbol{u}_{dcf}$ can be rewritten as,

$$\begin{aligned}\boldsymbol{u}_{dcf}&=\hat{\boldsymbol{G}}_{ib}\tilde{\boldsymbol{i}}_{bf}+\hat{\boldsymbol{G}}_{ud}\boldsymbol{u}_{df}+\hat{\boldsymbol{G}}_{un}u_n\\&=\begin{bmatrix}-R_f\hat{B}_{11} & -R_f\hat{\boldsymbol{B}}_{12} & -R_f\hat{\boldsymbol{B}}_{13}\\ -\boldsymbol{R}_{eq}\hat{\boldsymbol{B}}_{21} & -\boldsymbol{R}_{eq}\hat{\boldsymbol{B}}_{22} & -\boldsymbol{R}_{eq}\hat{\boldsymbol{B}}_{23}\\ \hat{\boldsymbol{E}}_{i1} & \hat{\boldsymbol{E}}_{i2} & \hat{\boldsymbol{E}}_{i3}\\ \hat{\boldsymbol{F}}_{i1} & \hat{\boldsymbol{F}}_{i2} & \hat{\boldsymbol{F}}_{i3}\end{bmatrix}\begin{bmatrix}i_{bf1}\\ \boldsymbol{i}_{bf}^{(2)}\\ \boldsymbol{i}_{bf}^{(3)}\end{bmatrix}+\begin{bmatrix}0 & & \\ \boldsymbol{K}_u & & \\ & \hat{\boldsymbol{E}}_{u1} & \\ & & \hat{\boldsymbol{F}}_{u1}\end{bmatrix}\boldsymbol{u}_{df}+\begin{bmatrix}-1\\ \boldsymbol{0}_{(M_1+M_2+M_3)\times 1}\\ \hat{\boldsymbol{E}}_{u2}\\ \hat{\boldsymbol{F}}_{u2}\end{bmatrix}u_n\end{aligned} \tag{3-26}$$

### 3.5.3 State-Space Equation of the Fault Component Network

Substitution of (3-19) and (3-26) into (3-12), it yields that,

$$\boldsymbol{C}_c\frac{\mathrm{d}\boldsymbol{u}_{df}}{\mathrm{d}t}=-\begin{bmatrix}\hat{\boldsymbol{B}}_{21} & \hat{\boldsymbol{B}}_{22} & \hat{\boldsymbol{B}}_{23}\\ \hat{\boldsymbol{B}}_{31} & \hat{\boldsymbol{B}}_{32} & \hat{\boldsymbol{B}}_{33}\end{bmatrix}\begin{bmatrix}i_{bf1}\\ \boldsymbol{i}_{bf}^{(2)}\\ \boldsymbol{i}_{bf}^{(3)}\end{bmatrix}-\boldsymbol{g}_d\boldsymbol{u}_{df}+\boldsymbol{K}_{ieq}^T\boldsymbol{i}_{eqf}=\tilde{\boldsymbol{B}}\tilde{\boldsymbol{i}}_{bf}-\boldsymbol{g}_d\boldsymbol{u}_{df}+\boldsymbol{K}_{ieq}^T\boldsymbol{i}_{eqf} \tag{3-27}$$

Similarly, substituting (3-19) and (3-26) into (3-16) provides,

$$\begin{aligned}\tilde{\boldsymbol{L}}_b\frac{\mathrm{d}\tilde{\boldsymbol{i}}_{bf}}{\mathrm{d}t}&=\begin{bmatrix}L_{b1}&&\\&\boldsymbol{L}_b^{(2)}&\\&&\boldsymbol{L}_b^{(3)}\end{bmatrix}\frac{\mathrm{d}\tilde{\boldsymbol{i}}_{bf}}{\mathrm{d}t}=-\begin{bmatrix}R_{b1}&&\\&\boldsymbol{R}_b^{(2)}&\\&&\boldsymbol{R}_b^{(3)}\end{bmatrix}\tilde{\boldsymbol{i}}_{bf}+\begin{bmatrix}\hat{A}_{11}\hat{\boldsymbol{A}}_{12}\hat{\boldsymbol{A}}_{13}\hat{\boldsymbol{A}}_{14}\\\hat{\boldsymbol{A}}_{21}\hat{\boldsymbol{A}}_{22}\hat{\boldsymbol{A}}_{23}\hat{\boldsymbol{A}}_{24}\\\hat{\boldsymbol{A}}_{31}\hat{\boldsymbol{A}}_{32}\hat{\boldsymbol{A}}_{33}\hat{\boldsymbol{A}}_{34}\end{bmatrix}\left(\hat{\boldsymbol{G}}_{id}\tilde{\boldsymbol{i}}_{bf}+\hat{\boldsymbol{G}}_{ud}\boldsymbol{u}_{df}+\hat{\boldsymbol{G}}_{un}\boldsymbol{u}_n\right)\\&=\tilde{\boldsymbol{R}}_b\tilde{\boldsymbol{i}}_{bf}+\tilde{\boldsymbol{A}}\left(\hat{\boldsymbol{G}}_{id}\tilde{\boldsymbol{i}}_{bf}+\hat{\boldsymbol{G}}_{ud}\boldsymbol{u}_{df}+\hat{\boldsymbol{G}}_{un}\boldsymbol{u}_n\right)\end{aligned}\tag{3-28}$$

By combining (3-13), (3-27), and (3-28), the state-space equation of the fault component network is expressed as,

$$\begin{aligned}\frac{\mathrm{d}\boldsymbol{x}}{\mathrm{d}t}&=\frac{\mathrm{d}}{\mathrm{d}t}\begin{bmatrix}\tilde{\boldsymbol{i}}_{bf}\\\boldsymbol{u}_{df}\\\boldsymbol{i}_{eqf}\end{bmatrix}=\begin{bmatrix}-\tilde{\boldsymbol{L}}_b^{-1}\left(\hat{\boldsymbol{G}}_{ib}\tilde{\boldsymbol{R}}_b\right)&-\tilde{\boldsymbol{L}}_b^{-1}\tilde{\boldsymbol{A}}\hat{\boldsymbol{G}}_{ud}&\boldsymbol{0}_{(M+1)\times(M_3+M_5)}\\\boldsymbol{C}_c^{-1}\tilde{\boldsymbol{B}}&-\boldsymbol{C}_c^{-1}\boldsymbol{g}_d&-\boldsymbol{C}_c^{-1}\boldsymbol{K}_{ieq}^{T}\\\boldsymbol{0}_{(M_3+M_5)\times(M+1)}&-\boldsymbol{L}_{eq}^{-1}\boldsymbol{K}_{ieq}&-\boldsymbol{L}_{eq}^{-1}\boldsymbol{R}_{eqs}\end{bmatrix}\begin{bmatrix}\tilde{\boldsymbol{i}}_{bf}\\\boldsymbol{u}_{df}\\\boldsymbol{i}_{eqf}\end{bmatrix}+\begin{bmatrix}\tilde{\boldsymbol{L}}_b^{-1}\tilde{\boldsymbol{A}}\hat{\boldsymbol{G}}_{ud}\\\boldsymbol{0}_{M\times1}\\\boldsymbol{0}_{(M_3+M_5)\times1}\end{bmatrix}u_n\\&=\boldsymbol{A}\boldsymbol{x}+\boldsymbol{B}u_n\end{aligned}\tag{3-29}$$

Since the state variables are the electrical quantities of the fault component network, their initial value should be 0, i.e., $\boldsymbol{x}_0=\boldsymbol{0}_{(2M+M_3+M_5+1)\times1}$. Accordingly, the solution of the dynamic equation expressed by (3-29) is written as,

$$\boldsymbol{x}(t)=\boldsymbol{A}^{-1}\mathrm{e}^{\boldsymbol{A}t}\boldsymbol{B}u_n-\boldsymbol{A}^{-1}\boldsymbol{B}u_n\tag{3-30}$$

Based on (3-30), the dynamics of state variables of the system are calculated via matrix manipulations rather than numerical integration, which reduces the computational burden and avoids numerical issues. The operation values can be determined based on (3-10), (3-18), (3-19), and (3-26).

## 3.6 Case Studies

A radial and a meshed MTDC system are built in PSCAD/EMTDC, separately. The fault current obtained via EMPT simulation is compared with the calculated fault current to validate the accuracy of the proposed fault calculation method.

### 3.6.1 Radial MTDC System

Fig. 3-2 presents the topology of the radial LCC-MMC MTDC system. The constant current control is adopted by the 12-pulse LCC-based rectifier, while the two MMC-based inverters adopt the droop control. According to the numbering rule, Node 1 is connected to the LCC-based rectifier, Node 2 and Node 3 are connected to the MMC-based inverters, and Node 4 is a virtual node. Transmission lines are represented by the detailed frequency-dependent model, whose lengths are given in Fig. 3-2. The nominal DC voltage of the system is ±200 kV.

The inductance of smoothing reactors deployed at the terminal of LCC is chosen as 400 mH. The supplementary DC reactors are selected as 150 mH. Other parameters of the test system are presented in Table 3-1.

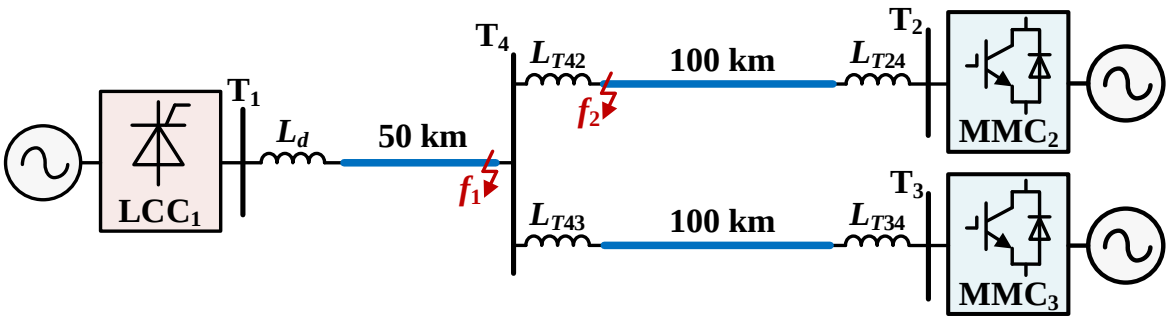


Fig. 3-2 Topology of the test radial MTDC system.

Table 3-1 Main parameters of the test radial MTDC system

| Symbol | Item | Value |
|---|---|---|
| $u_n$ | Nominal DC-link voltage of the test system | ±200 kV |
| $\omega_s$ | Nominal frequency of AC grids | 50 Hz |
| $d_\gamma$ | Equivalent commutation resistance | 41 Ω |
| $i_{dc}^{ref}$ | Reference DC-link current | 1 kA |
| ($K_{Pc}$, $K_{Ic}$) | Proportional and integral gains of constant current control | (1, 100) |
| $L_d$ | LCC-side smoothing reactor | 400 mH |
| $N_{sm}$ | Number of SMs of MMC in one arm | 200 |
| $C_{sm}$ | SM capacitance of MMC | 12 mF |
| $R_{on}$ | On-state resistance of one IGBT/diode | 5.445 mΩ |
| $L_a$ | Arm inductance of MMC | 60 mH |
| $\sigma_i$ | Time constant of the inner loop | 2 ms |
| ($K_{Po}$, $K_{Io}$) | Proportional and integral gains of the outer loop | (1, 10) |
| $K_d$ | Power-voltage droop coefficient | 0.2 |
| $L_T$ | DC reactor inductance | 150 mH |
| $R_0$ | Per-kilometre resistance of DC line | 0.015 Ω |
| $L_0$ | Per-kilometre inductance of DC line | 1.4 mH |
| $f_s$ | Sampling frequency | 10 kHz |

The fault component current of the test radial MTDC system under metallic faults is shown in Fig. 3-3, which compares the EMTP simulation and the proposed model. As seen from Fig. 3-3 (a), the current injected by the LCC-based rectifier quickly rises after the DC fault. Then, the fault current reaches the peak value at around 4 ms and starts to decrease

gradually because of the constant current control of the LCC. On the other hand, the current injected by the MMC inverter illustrated by Fig. 3-3 (b) sharply increases over 8 ms, indicating a clear capacitor discharging process. Moreover, the fault current with EMTP simulation has slight fluctuations owing to the travelling wave propagation process, but the overall patterns of the fault current are very similar to those with the proposed method. It suggests that the proposed method can effectively simplify the model complexity with little accuracy loss.

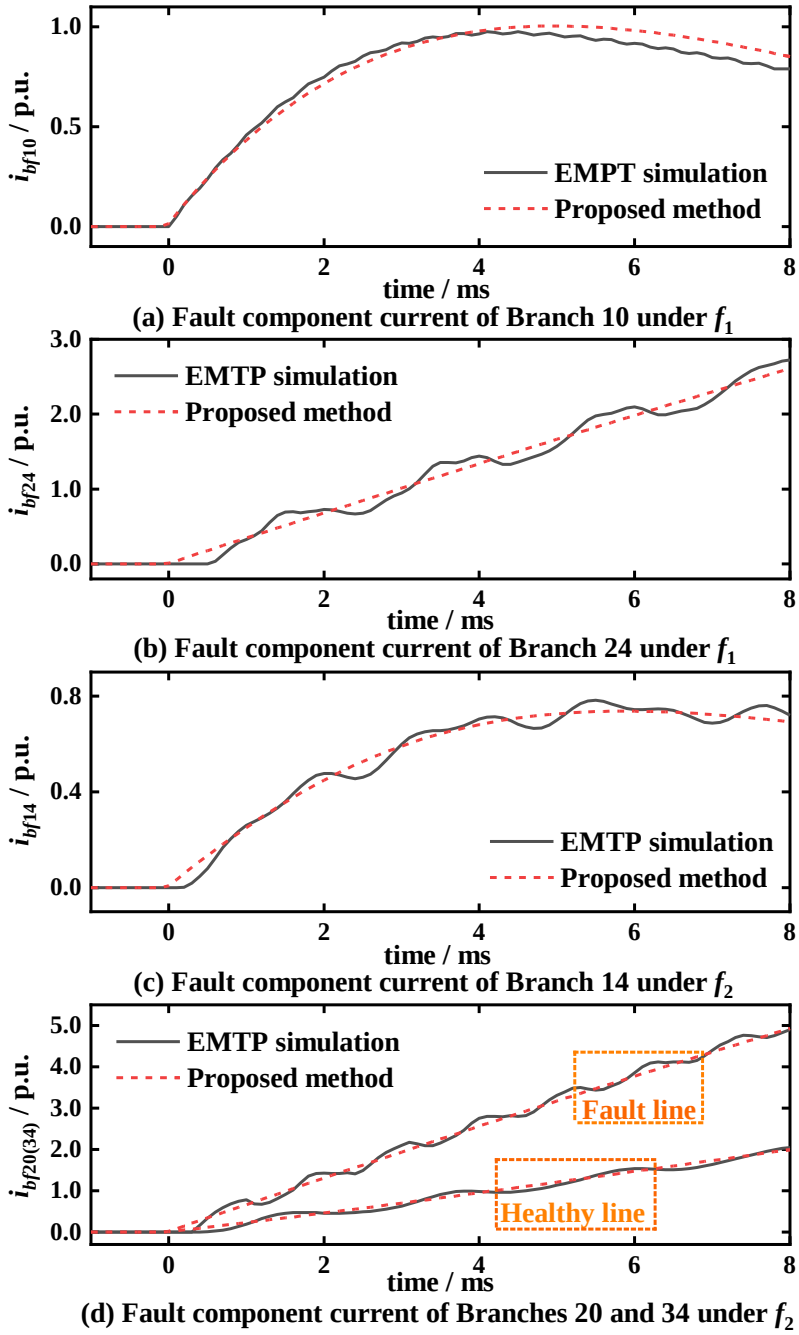


Fig. 3-3 Short-circuit current of the test radial system under metallic DC faults.

Fig. 3-3 (c) and (d) illustrate the fault current with a metallic fault occurring between $L_{T42}$

and Line 24 ($f_2$). As illuminated by by Fig. 3-3 (c), there is a drop of the current of Branch 10 and more noticeable travelling wave propagations than those in Fig. 3-3 (a), because of the increase in fault distance. For MMC-connected lines in Fig. 3-3 (d), the fault line current rises evidently faster than that of the healthy line. Furthermore, the errors between fault current with the EMTP simulation and the proposed model are relatively small, which demonstrates the accuracy of the proposed model in short-circuit current calculation within the first moments after the DC fault.

Fig. 3-4 depicts the dynamics of the test radial MTDC system under DC faults with a fault resistance of 300 Ω. When a high-resistance fault occurs at the terminal of Line 14 near Node 4 ($f_1$), the injected current from the LCC-based rectifier first rises and soon decreases with the effects of the constant current control, as illustrated by Fig. 3-4 (a). It can be seen from Fig. 3-4 (b) that there is an apparent saturation trend of the fault component of the injected current from the MMC-based inverter. Moreover, the short-circuit current with the proposed model and that with the EMTP simulation are approximated to each other. Fig. 3-4 (c) shows the fault current dynamics under a DC fault with a fault resistance of 300 Ω occurring between $L_{T42}$ and Line 24 ($f_2$). Compared with Fig. 3-3 (a) and (c), it is found that the injected current from the LCC decreases due to the increase in the fault distance. Fig. 3-4 (d) shows the fault component current of Branch 20 and Branch 34 under $f_2$. The fluctuations of current in the healthy line are larger than those of the fault line. This is because of electrical distance from the fault point to the measurement point of the healthy line is farther than that of the fault line, leading to more apparent travelling wave processes. Nevertheless, the fault current with EMTP simulation still vibrates slightly around that with the proposed method, which again validates the accuracy of the proposed method in fault calculation.

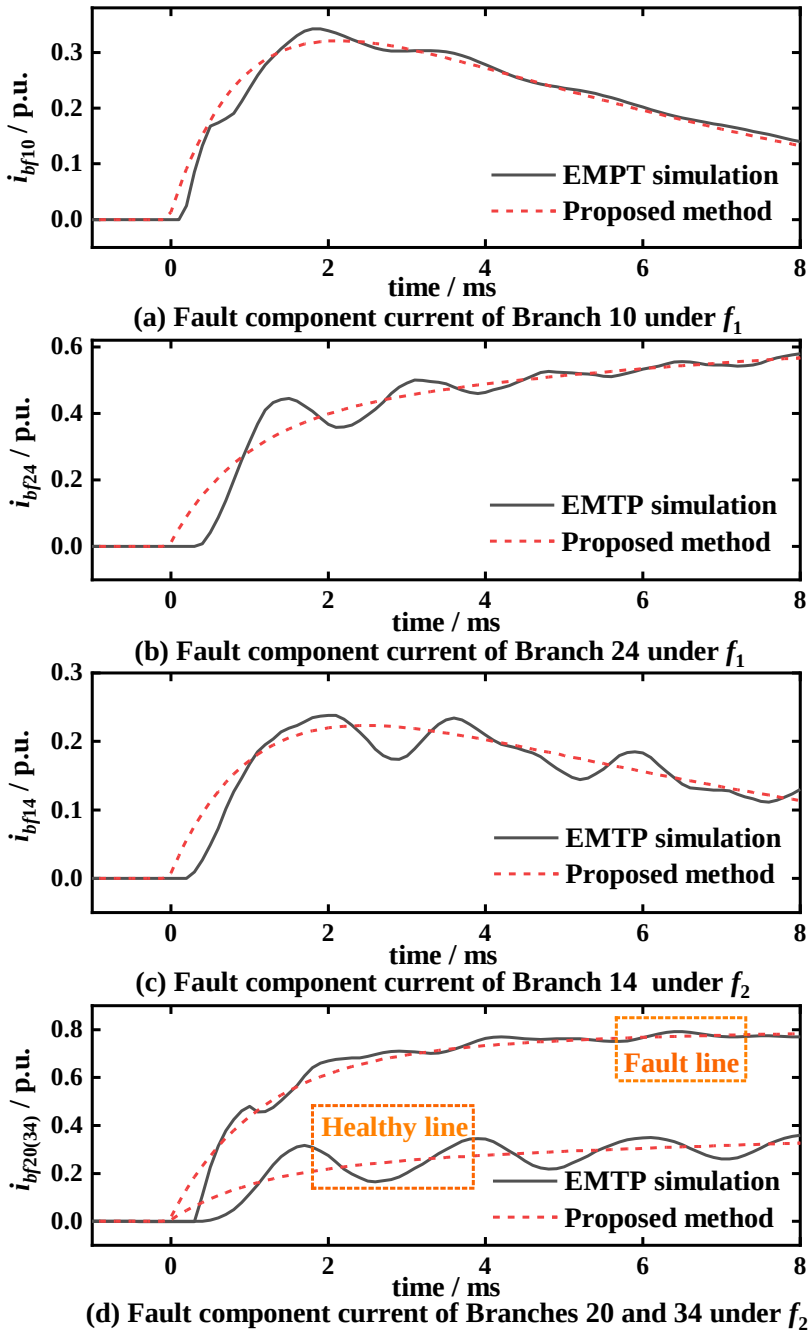


Fig. 3-4 Short-circuit current of the test radial system under high-resistance DC faults.

### 3.6.2 Meshed MTDC System

Fig. 3-5 depicts the topology of the meshed six-terminal MMC-MTDC system. $MMC_1$ to $MMC_5$ adopt the CPC, while $MMC_6$ adopts the CDVC. The nominal DC voltage of the system is ±400kV. The supplementary DC reactors are chosen to be 100 mH. The length of each DC transmission line is given in Fig. 3-5. Other main parameters of the test meshed system are summarized in Table 3-2.

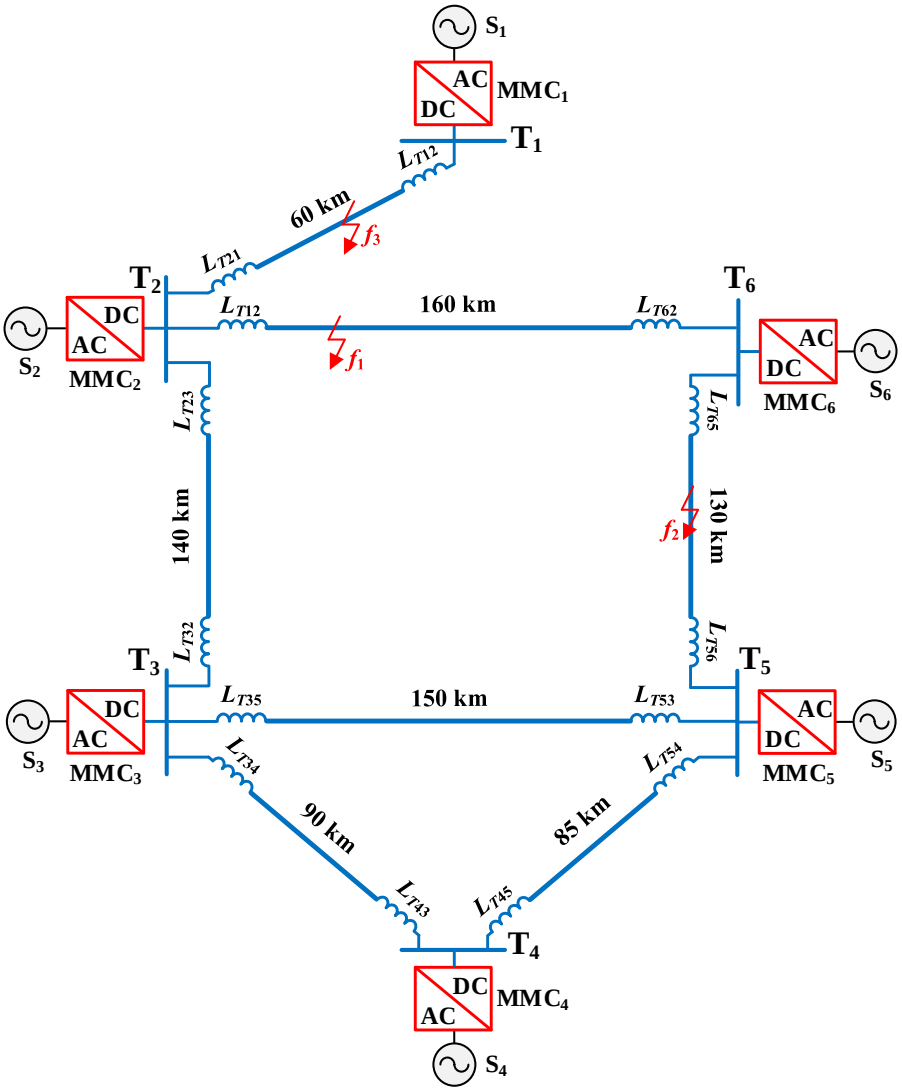


Fig. 3-5 Topology of the test meshed MTDC system.

Table 3-2 Main parameters of the test meshed MTDC system

| Symbol | Item | Value |
|---|---|---|
| $u_n$ | Nominal DC-link voltage of the meshed system | ±400 kV |
| $N_{sm}$ | Number of SMs per arm of MMC | 200 |
| $C_{sm}$ | SM capacitance of MMC | 0.8 mF |
| $R_{on}$ | On-state resistance of one IGBT/diode | 5.445 mΩ |
| $L_a$ | Arm inductance of MMC | 70 mH |
| $\sigma_i$ | Time constant of the inner loop | 2 ms |
| ($K_{Po}$, $K_{Io}$) | Proportional and integral gains of the CPC | (1, 10) |
| ($K_{Pv}$, $K_{Iv}$) | Proportional and integral gains of the CDVC | (5, 10) |
| $L_T$ | DC reactor inductance | 100 mH |
| $R_0$ | Per-kilometre resistance of DC line | 0.015 Ω |
| $L_0$ | Per-kilometre inductance of DC line | 1.4 mH |

Fig. 3-6 shows the fault component current of Branch 26 under various metallic DC faults. The fault distance here is defined from the fault point to Node 2.

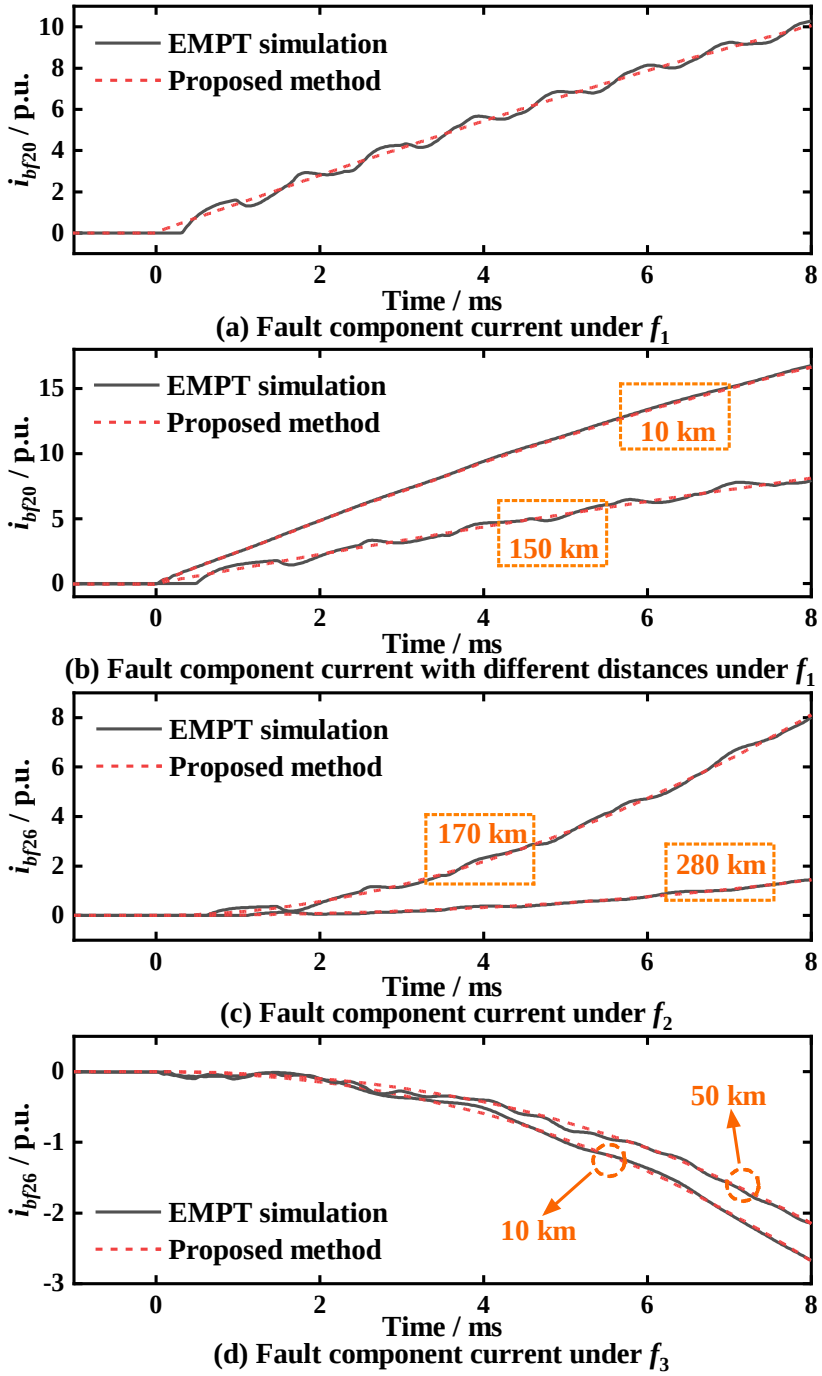


Fig. 3-6 Short-circuit current of the test meshed system under metallic faults.

Fig. 3-6 (a) depicts the current dynamics when a metallic fault happens on Line 26 ($f_1$) with a fault distance of 100 km. The fault component current rises rapidly after the fault. Because of the travelling wave process, the short-circuit current with EMTP simulation denoted by the solid black line fluctuates around the current curve obtained by the proposed

method marked as the red dashed line. However, the overall trends of the two curves are fairly similar. As illustrated by Fig. 3-6 (b), the errors between the results of EMTP simulation and the proposed method are related to the fault distance. When the fault distance is 10 km, the two current curves almost overlap together. As the fault distance increases to 150 km, the refractions and reflections of travelling waves become more apparent, leading to small vibrations in the simulation current curve compared to that of the proposed method. Notably, the errors between the lumped and distribution parameters models are in an acceptable range no matter the fault distance. Fig. 3-6 (c) shows the system dynamics under metallic fault occurring on Line 56 ($f_2$). It is observed that the fault current decreases significantly with the increase in the fault distance. Besides, the fault component current rises much slower compared with the cases of $f_1$ faults. This is because the measured current is that of Branch 26, which is a healthy line in this fault scenario. Fig. 3-6 (d) shows the fault component current when metallic faults occur on Line 12 ($f_3$). In this situation, the fault component current becomes negative because the direction of the current is defined as from Node 2 to Node 6. Since Branch 26 is a healthy line in this case, the current curves are very similar to those of $f_2$ faults. It is indicated from Fig. 3-6 that the results of the proposed method are very close to those of EMTP simulation, which manifests the accuracy of the proposed method for short-circuit current calculation in the initial DC fault period.

Fig. 3-7 presents the fault component current of Branch 26 under various high-resistance DC faults. Fig.3-7 (a) illustrates the short-circuit current dynamics when the fault distance is 100 km. Different from the current curves under metallic faults, the fault component current fast rises around 1 ms to 2 ms and soon exhibits an apparent saturation trend. This is because the DC-link voltage under high-resistance faults is higher than that under metallic faults, which shortens the discharging time of the DC-link capacitor. In addition, it is indicated from Fig. 3-7 that the fault current decreases as the fault resistance increases. Fig. 3-7 (b) and (c) show the system dynamics when the fault distances are 10 km and 150 km, respectively. As the fault distance increases, the fault component current becomes lower. Simultaneously, the travelling wave process gets easier to be observed. Fig. 3-7 (d) shows the fault component current under $f_2$ and $f_3$ faults. The fault distances are 170 km and 10 km, respectively. Since the measured current is flowing through the healthy line, i.e., Branch 26, the fault component current increases much slower compared to the aforementioned cases. Moreover, it is shown in Fig. 3-7 that the fault component current based on the proposed method is fairly close to that obtained from EMTP simulation, which again manifests the effectiveness of the proposed

method for the initial DC fault analysis in MTDC systems.

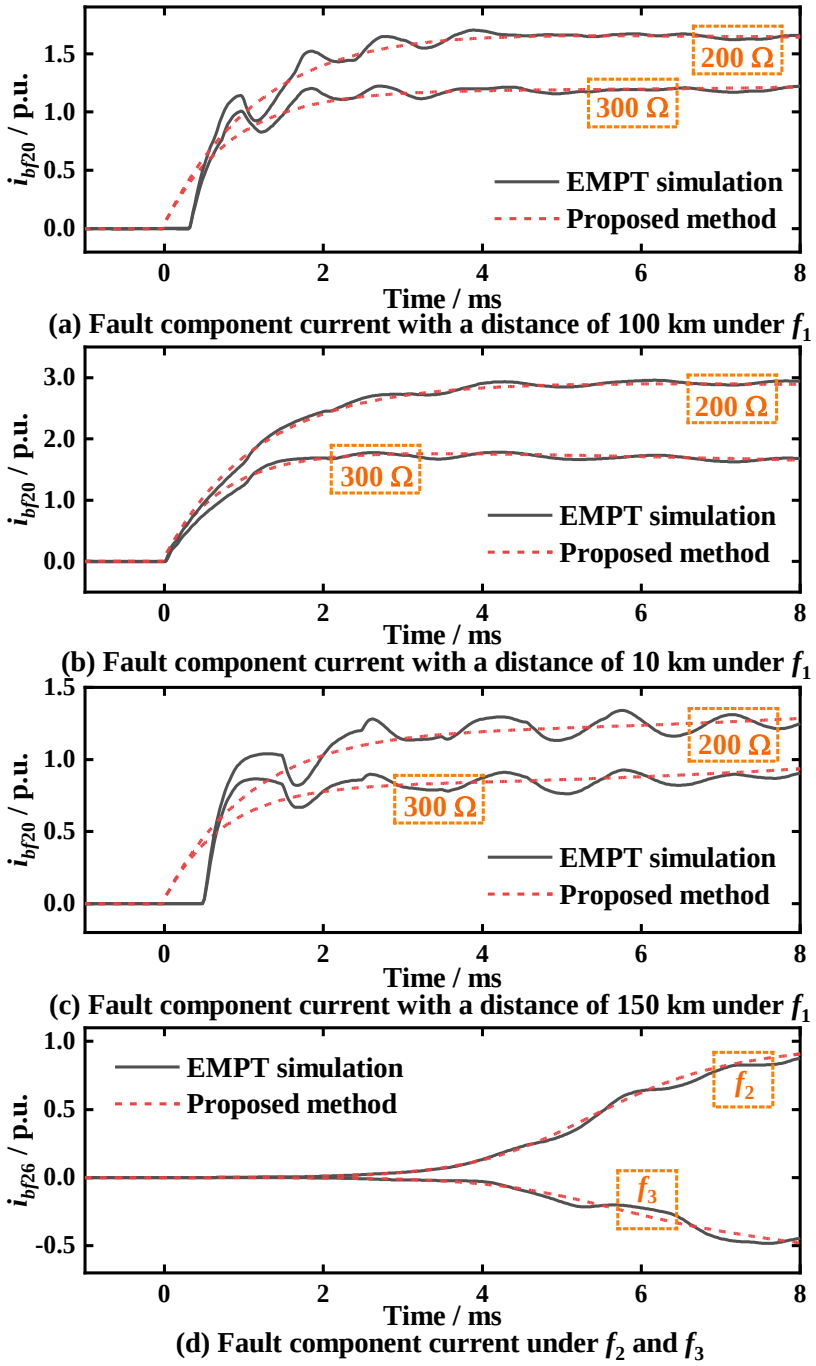


Fig. 3-7 Short-circuit current of the test meshed system under high-resistance faults.

The computational time of the state space method is related to the scale of the studied system. For the cases of the test radial and meshed MTDC systems, the computational time is less than 1 second. However, the time of simulation is several minutes. It is indicated that the state-space method can boost computation efficiency by getting rid of time-consuming numerical integrations.

## 3.7 Summary

A short-circuit current calculation method for generic MTDC systems is proposed in this chapter. On the basis of the linear converters models derived in the last chapter, the entire DC system is linear, and thereby the superposition principle can be used to facilitate the analysis. By eliminating the nonstate variables of the system equations, the state-space equation of the fault component network is formulated. Accordingly, the mathematical expression of the fault component current of the entire system can be obtained, which enables fast fault calculation based on matrix manipulations instead of solving DAEs based on numerical integration. Additionally, the proposed method is fully available to various MTDC systems with different network topologies, converters types, and control modes. Simulation studies have validated the accuracy and adaptability of the proposed method.

# 4 DC Fault Calculation of VSC-MTDC Systems Based on High-Frequency Equivalent Model

## 4.1 Introduction

A state-space-based fault calculation method for generic MTDC systems is proposed in the last chapter. Although the proposed method gets rid of the numerical solution of DAEs, the relatively complicated matrix manipulations make it hard to get general and clear rules of the fault current in MTDC systems as per (3-30).

The case studies of the meshed VSC-MTDC system in the last chapter show that the fault current in the fault line seems to increase linearly under metallic DC faults. As for healthy lines, the increasing speed of the fault current is much slower than that of the fault line because of the existence of the DC-link capacitors of VSCs, but the waveforms of healthy line current are not complicated either. Consequently, it is possible to derive simpler fault current expressions for VSC-MTDC systems. Note that the first milliseconds after the fault are of interest in the fault calculation of VSC-MTDC systems, and the high-frequency components of electrical quantities dominate in the fault network in this short period. Based on this property, the fault calculation can be significantly simplified.

This chapter proposes a simple DC fault calculation method for the most common VSC-MTDC systems using the high-frequency equivalent (HFE) model. The Laplace circuit of the fault network is first formed. Then, since only the high-frequency electrical quantities exist in the Laplace fault component network in the first milliseconds after the fault, the HFE model for the initial DC fault calculation is proposed by reserving only the high-frequency components of the Laplace circuit. Based on the HFE model, analytical time-domain expressions of the fault current of the entire network are derived. The proposed method can achieve a more straightforward DC fault analysis than existing approaches, with simple calculations and little loss of accuracy.

## 4.2 DC Fault Analysis of the Radial VSC-MTDC System

Fig. 4-1 illustrates a typical radial four-terminal DC grid that connects three offshore wind farms and one onshore AC main grid with submarine DC cables. Take a metallic fault that happens on Line 14 as an example, and the fault point is labelled as Node 0. The DC submarine

cable is simplified as a π-section, and the transient travelling wave process of the transmission line is disregarded. The resistance and inductance of Line *mn* are represented by $R_{lmn}$ and $L_{lmn}$, separately. The inductance of the DC implemental inductor installed at the *m* terminal of Line *mn* is represented by $L_{Tmn}$. For simplicity, the effect of the equivalent capacitor of cables can be added to the DC-link capacitor of VSC$_k$ as a lumped grounded capacitor at the terminal of each branch. The grounded capacitor denoted by $C_{ck}$, as shown in Fig. 4-1, is defined as the sum of the capacitance of the DC-link capacitor of VSC$_k$ and the equivalent capacitor of Cable *mn*. Although the travelling wave process is neglected by using the lumped parameter line model, it accurately reflects the relatively low-frequency properties of the fault current and thus is applicable to short-circuit current approximate calculation.

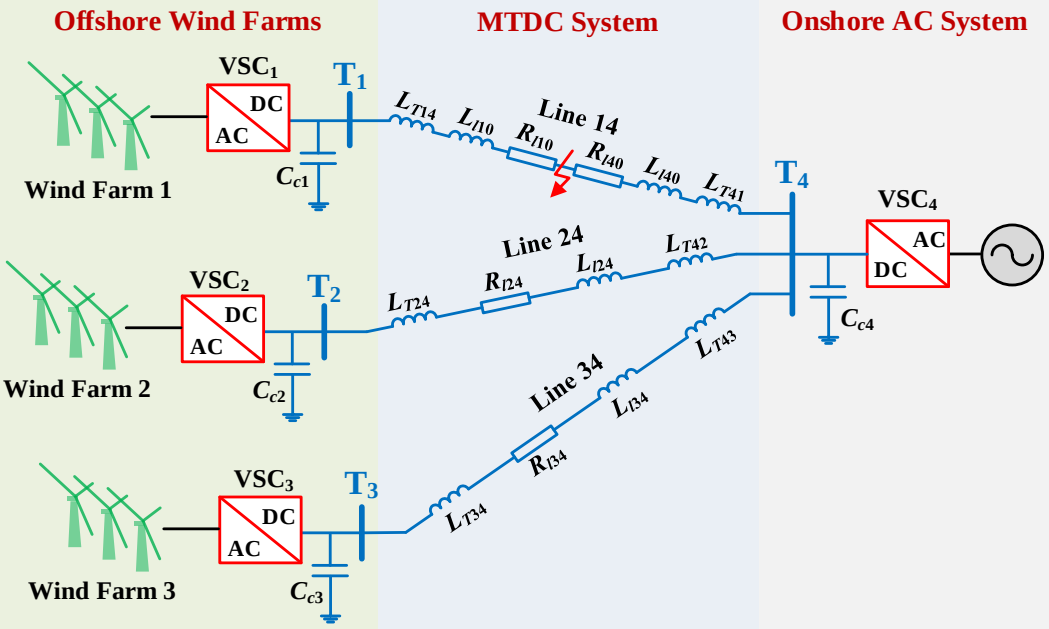


Fig. 4-1 Schematic of four-terminal radical MTDC system interconnecting offshore wind farms and onshore AC system.

### 4.2.1 Laplace Circuit of the Radial VSC-MTDC System

Similar to the analysis in the last chapter, the DC grid with a DC fault can be separated into a normal operation network and a fault component network, as seen in Fig 4-2, by using the superposition principle of electrical circuits due to the linear property of the DC grid. The fault component current can be easily obtained by solving the fault component network derived from adding a fault voltage source to the passive part of the original network. The positive direction of cable current is defined as from the healthy cable to the faulty one. The fault current calculation utilises the classical Laplace transform method that translates complex derivative operations into simpler algebraic operations.

As illustrated by Fig. 4-2 (c), the fault component current of Branch 10 denoted by $i_{bf10}$ is determined through solving the left-hand side (LHS) circuit of the fault point.

$$i_{bf10}(s)=\frac{u_n/s}{R_{l10}+s\left(L_{l10}+L_{T14}\right)+\left(sL_{eq1}^{VSC}+R_{eqs1}^{VSC}\right)/\!/\,R_{eqp1}^{VSC}/\!/\left(1/sC_{c1}\right)} \tag{4-1}$$

where $L_{eq}^{VSC}$, $R_{eqs}^{VSC}$, and $R_{eqp}^{VSC}$ are the equivalent parameters of the VSC model derived in Chapter 2. // denotes parallel connection, e.g., $x//y = 1/(1/x + 1/y)$.

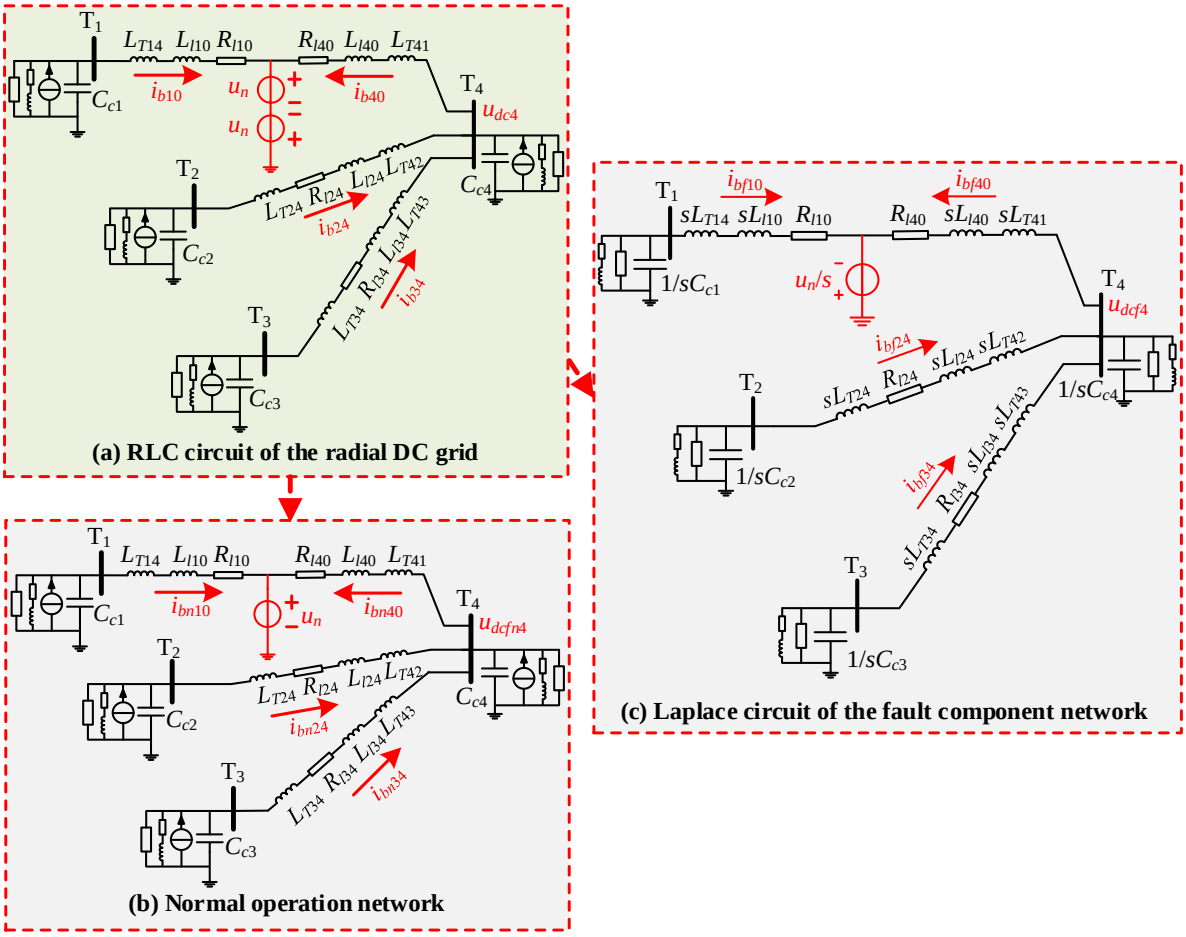


Fig. 4-2 Circuit for the four-terminal DC grid under study.

On the other hand, the deduction of fault component current of Branch 40 is much more complex because the grounded capacitor, Branch 24, and Branch 34 are parallel connected to Branch 40, significantly increasing the circuit complexity. For simplification, the related branch admittances are introduced as,

$$\begin{cases} Y_{b24}(s)=\dfrac{1}{R_{l24}+s\left(L_{l24}+L_{T24}+L_{T42}\right)+\left(sL_{eq2}^{VSC}+R_{eqs2}^{VSC}\right)/\!/\,R_{eqp2}^{VSC}/\!/\left(1/sC_{c2}\right)} \\ Y_{b34}(s)=\dfrac{1}{R_{l34}+s\left(L_{l34}+L_{T34}+L_{T43}\right)+\left(sL_{eq3}^{VSC}+R_{eqs3}^{VSC}\right)/\!/\,R_{eqp3}^{VSC}/\!/\left(1/sC_{c3}\right)} \end{cases} \tag{4-2}$$

where, $Y_{b24}$ and $Y_{b34}$ are the admittance of Branch 24 and Branch 34, respectively. Applying KCL to Terminal 4, the following equality holds.

$$Y_{b24}(s)u_{dcf4}(s)+Y_{b34}(s)u_{dcf4}(s)+sC_{c4}u_{dcf4}(s)-i_{bf40}(s)=0 \tag{4-3}$$

where, $u_{dcf4}$ and $i_{bf40}$ denote the fault component of the DC-link voltage of Terminal 4 and the fault component current of Branch 40, individually.

Applying KVL to the right-hand side (RHS) circuit of the fault point, the following equation should hold.

$$\frac{u_n}{s}u_{dcf4}(s)-\left(R_{l40}+sL_{l40}+sL_{T41}\right)i_{bf40}(s)=0 \tag{4-4}$$

By synthesizing (4-3) and (4-4), $u_{dcf4}$ is eliminated, and it yields the expression of $i_{bf40}$ as follows.

$$i_{bf40}(s)=\frac{u_n/s}{R_{l40}+s\left(L_{l40}+L_{T41}\right)+\left(1/Y_{b24}(s)\right)/\!/\left(1/Y_{b34}(s)\right)/\!/\left(sL_{eq4}^{VSC}+R_{eqs4}^{VSC}\right)/\!/R_{eqp4}^{VSC}/\!/\left(1/sC_{c4}\right)} \tag{4-5}$$

### 4.2.2 High-Frequency Equivalent Model and the Reduction of Initial Fault Calculation

The proposed analytic converter model is only valid for fault analysis within several milliseconds after the DC fault. Therefore, it is unnecessary and inaccurate to derive the full time-domain expression of $i_{bf40}(t)$ through the inverse Laplace transform of (4-5).

When the observed time is very short, the slow-changing low-frequency components of a signal cannot be reflected, while its fast-changing high-frequency components can be obtained. Therefore, during the initial first instants after the occurrence of the fault, only the high-frequency components of electrical quantities dominate in the Laplace circuit. Based on this property, the low-frequency components in the Laplace circuit can be omitted for the fault calculation in the initial fault period. The reserved Laplace circuit composed of high-frequency components is referred to as the high-frequency equivalent (HFE) model, which is very useful for simplifying the initial fault analysis.

Normally, the capacitor discharging period of VSC-MTDC systems does not exceed 10 ms, so the high-frequency region is above 100 Hz here. The following inequalities hold with typical parameters of VSC-MTDC systems in the high-frequency domain,

$$\begin{cases} \left|sL_{bij}\right| = \left|s\left(L_{lij} + L_{Tij} + L_{Tji}\right)\right| \gg \left|1/sC_{ci}\right| \\ \left|sL_{eqi}^{VSC}\right| \gg \left|1/sC_{ci}\right| \\ \left|R_{eqpi}^{VSC}\right| \gg \left|1/sC_{ci}\right| \end{cases}, \quad i = 1,2,3,4 \tag{4-6}$$

Fig. 4-3 illustrates the amplitude-frequency characteristics of the branch inductance of a 100 km DC cable connected with two DC reactors of 100 mH at the terminals, the grounded capacitor, the equivalent inductance and resistance of the TLVSC with typical HVDC parameters. It is validated that the inductance and resistance components are more influential than the capacitance in the high-frequency domain, where the inequalities expressed in (4-6) can hold.

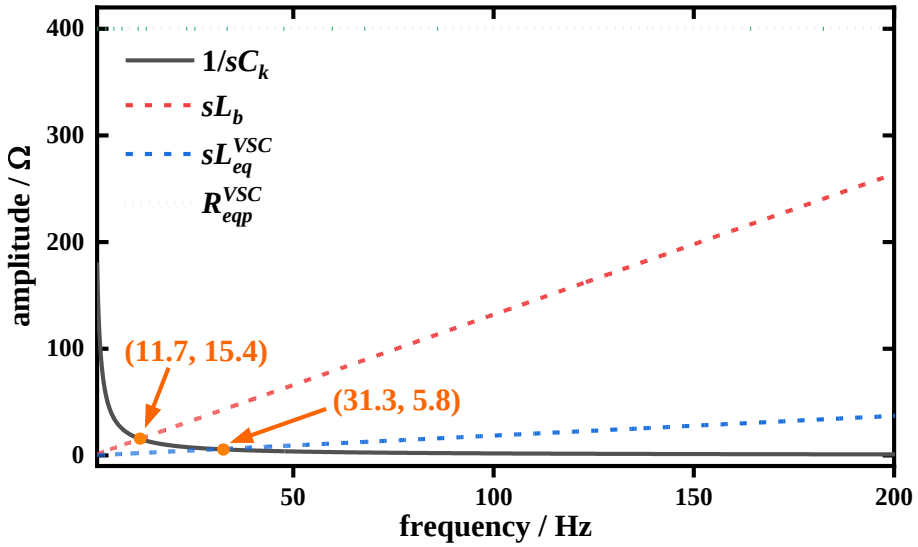


Fig. 4-3 Amplitude-frequency characteristics of the grounded capacitor, branch inductance, equivalent inductance and resistance of the TLVSC with typical HVDC parameters.

Based on (4-6) and further neglecting the resistances of DC cable lines, it yields the following relation,

$$\left|Y_{bi4}(s)\right| \approx \left|\frac{1}{R_{li4} + sL_{bi4} + 1/sC_{ci}}\right| \approx \left|\frac{1}{sL_{bi4}}\right| = \left|1/s\left(L_{li4} + L_{Ti4} + L_{T4i}\right)\right|, \quad i = 2,3 \tag{4-7}$$

Based on (4-7), the DC cable line is simplified as an equivalent inductance for the initial fault calculation. By substituting (4-6) into (4-7), it yields that,

$$\left|Y_{bi4}\right| \approx \left|1/sL_{bi4}\right| \ll \left|sC_{c4}\right|, \quad i = 2,3 \tag{4-8}$$

(4-8) indicates that in the high-frequency domain, the admittance of the DC-link capacitor $C_{c4}$ are much larger than those of Branch 24 and Branch 34.

In the high-frequency domain, Branch 24 and Branch 34 can be neglected. By

synthesizing (4-5) and (4-8), the expression of the high-frequency component of the fault component current of Branch 40 marked as $i_{bf40}^{H}(s)$ is obtained as,

$$i_{bf40}(s)=\frac{u_n/s}{R_{l40}+s\left(L_{l40}+L_{T41}\right)+\left(sL_{eq4}^{VSC}+R_{eqs4}^{VSC}\right)/\!/\,R_{eqp4}^{VSC}/\!/\left(1/sC_{c4}\right)} \tag{4-9}$$

Compared with (4-1) and (4-9), it is found that the fault component current in the LHS and RHS branches of the fault point have the same format, indicating that branches parallel connected to the grounded capacitor can be neglected for the initial fault calculation of the fault line. Substitution of (4-6) into (4-1) and (4-9), the fault component current of the fault line can be reduced in the high-frequency region as,

$$i_{bfi0}^{H}(s)=\frac{u_n/s}{R_{li0}+sL_{bi0}+1/sC_{ci}},\quad i=1,4 \tag{4-10}$$

As for the fault component current of healthy lines, the following reduction holds in the high-frequency region.

$$i_{bfi4}^{H}(s)=i_{bfi4}^{H}(s)\frac{Y_{bi4}(s)}{Y_{b24}(s)+Y_{b34}(s)+\left(1/sL_{eq4}^{VSC}+R_{eqs4}^{VSC}\right)+\left(1/R_{eqp4}^{VSC}\right)+sC_{c4}}\approx\frac{i_{bfi4}^{H}(s)}{s^2L_{bi4}C_{c4}},\quad i=2,3 \tag{4-11}$$

(4-10) and (4-11) are the reduced fault current expressions of the studied radial DC grid based on the HFE model, which indicate that the fault component current of the healthy line equals that of the fault line times a second-order low-pass filter. Therefore, the high-frequency component of the healthy line current diminishes drastically compared with that of the fault line current.

## 4.3 DC Fault Analysis of the Meshed VSC-MTDC System

Fig. 4-4 depicts a typical three-terminal meshed HVDC system with a metallic fault occurring on Line 12. Similar to the analysis of the radial system, DC transmission lines are represented by the lumped RL series circuit (RL model). The symbolic notations are the same as the radial system.

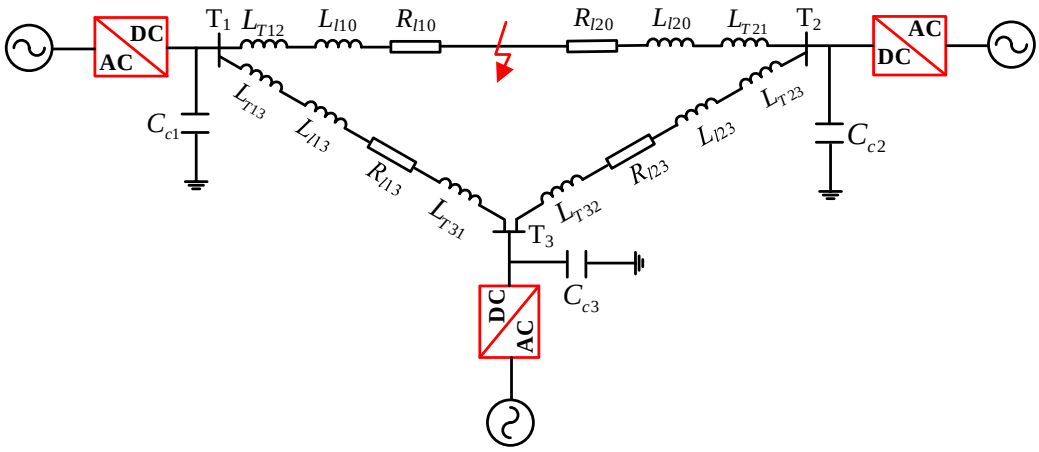


Fig. 4-4 Schematic of three-terminal meshed VSC-MTDC system.

### 4.3.1 Laplace Circuit of the Meshed VSC-MTDC System

Based on the superposition principle of linear electrical circuits, the Laplace circuit of the fault component network of the studied meshed DC system is shown in Fig. 4-5. To facilitate the analysis, the equivalent impedances of converters are first defined as follows.

$$Z_{ci}(s)=(1/sC_{ci})\ /\!/\ R_{eqpi}^{VSC}\ /\!/\ \left(sL_{eqi}^{VSC}+R_{eqsi}^{VSC}\right),\quad i=1,2,3 \tag{4-12}$$

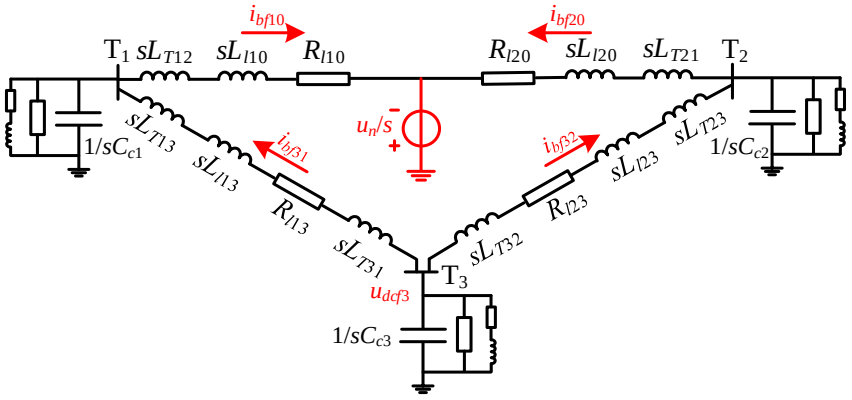


Fig. 4-5 Laplace fault component network of the meshed VSC-MTDC system.

Based on KCL and KVL, the following equation holds.

$$u_{dcf3}(s)=Z_{c3}(s)\left(i_{bf31}(s)+i_{bf32}(s)\right) \tag{4-13}$$

To open the loop in the meshed network, $Z_{c3}(s)$ is decomposed into two equivalent impedances as,

$$\begin{cases} Z_{c31}(s)=\dfrac{i_{bf31}(s)+i_{bf32}(s)}{i_{bf31}(s)}Z_{c3}(s) \\ Z_{c32}(s)=\dfrac{i_{bf31}(s)+i_{bf32}(s)}{i_{bf32}(s)}Z_{c3}(s) \end{cases} \tag{4-14}$$

Denote $r_{b21}$ as the ratio of the fault component current of Branch 32 and Branch 31, which is expressed as,

$$r_{b21}=\frac{i_{bf32}(s)}{i_{bf31}(s)} \tag{4-15}$$

Substitution of (4-15) into (4-14), it yields that,

$$\begin{cases} Z_{c31}(s)=(1+r_{b21})Z_{c3}(s) \\ Z_{c32}(s)=\left(1+\dfrac{1}{r_{b21}}\right)Z_{c3}(s) \end{cases} \tag{4-16}$$

Using the decomposed impedances expressed in (4-16), the studied meshed DC network turns into a radial one, as shown in Fig. 4-6. As per the LHS circuit of the fault point in the open-loop network, the fault component current of Branch 10 is calculated as,

$$i_{bf10}(s)=\frac{u_n/s}{R_{l10}+s(L_{l10}+L_{T12})+Z_{c1}(s)\,/\!/\,\left(R_{l13}+s(L_{l13}+L_{T13}+L_{T31})+Z_{c31}(s)\right)} \tag{4-17}$$

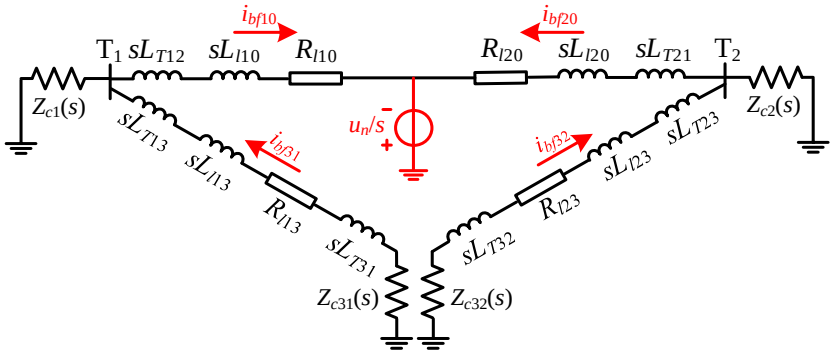


Fig. 4-6 Open-loop circuit of the fault component network of the studied meshed VSC-MTDC system.

### 4.3.2 Reduced Fault Current Expression Based on HFE Model

Deriving the time-domain expression of the fault current via the inverse Laplace transform of (4-17) is very difficult owing to the complex structure of the equivalent converters impedances $Z_{c1}(s)$ and $Z_{c31}(s)$. Similar to the analysis of the radial network, the HFE model is utilised to simplify the fault component network.

Based on the inequalities expressed in (4-6), the equivalent impedances of converters are simplified in the high-frequency region as follows.

$$Z_{ci}(s)=(1/sC_{ci})\,/\!/\,R_{eqpi}^{VSC}\,/\!/\,\left(sL_{eqi}^{VSC}+R_{eqsi}^{VSC}\right)\approx 1/sC_{ci},\quad i=1,2,3 \tag{4-18}$$

Based on (4-6) and (4-18), it can be concluded that the equivalent impedances of converters are much smaller than the branch impedances, and thus,

$$\begin{aligned} Z_{c1}(s)/\!/\left(R_{l13}+s\left(L_{l13}+L_{T13}+L_{T31}\right)+Z_{c31}(s)\right) &\approx \left(1/sC_{c1}\right)/\!/\left(R_{l13}+s\left(L_{l13}+L_{T13}+L_{T31}\right)+\left(1+r_{b21}\right)/sC_{c1}\right) \\ &\approx \left(1/sC_{c1}\right)/\!/\left(R_{l13}+s\left(L_{l13}+L_{T13}+L_{T31}\right)\right) \approx 1/sC_{c1} \end{aligned} \tag{4-19}$$

(4-19) indicates that the branches parallel connected to the ground capacitor can be omitted when calculating the fault line current. Substitution of (4-19) into (4-17), the fault component current of the fault line is reduced as follows in the high-frequency region.

$$i_{bf10}^{H}(s)=\frac{u_n/s}{R_{l10}+s\left(L_{l10}+L_{T12}\right)+1/sC_{c1}} \tag{4-20}$$

Compared with (4-10) and (4-20), it is found that the fault line current of radial and meshed VSC-MTDC systems can be expressed in the same format.

As for the healthy line, its fault component current can be expressed as follows in the high-frequency region based on (4-6).

$$\begin{aligned} i_{bf31}^{H}(s) &= i_{bf10}^{H}(s)\frac{1/\left(R_{l13}+s\left(L_{l13}+L_{T13}+L_{T31}\right)+Z_{c31}(s)\right)}{1/Z_{c1}(s)+1/\left(R_{l13}+s\left(L_{l13}+L_{T13}+L_{T31}\right)+Z_{c31}(s)\right)} \\ &\approx i_{bf10}^{H}(s)\frac{1/\left(R_{l13}+s\left(L_{l13}+L_{T13}+L_{T31}\right)+\left(1+r_{b21}\right)/sC_{c3}\right)}{1/sC_{c1}+1/\left(R_{l13}+s\left(L_{l13}+L_{T13}+L_{T31}\right)+\left(1+r_{b21}\right)/sC_{c3}\right)} \\ &\approx \frac{i_{bf10}^{H}(s)}{s^2L_{b13}C_{c1}} \end{aligned} \tag{4-21}$$

(4-21) indicates that the fault component current of the healthy line equals that of the fault line times a second-order low-pass filter in the meshed VSC-MTDC system. Combined with the fault current expressions as shown in (4-10), (4-11), (4-20), and (4-21), it is concluded that within the first instants after a DC fault, the high-frequency fault component current mainly flows in the fault line, while the low-frequency one flows in the other lines. This characteristic holds for both radial and meshed VSC-MTDC systems.

## 4.4 Analytical Fault Current Expression of Generic VSC-MTDC Systems

### 4.4.1 HFE Model of Generic VSC-MTDC Systems

The above fault analysis is based on networks with specified structures. However, to apply the HFE model to more generic VSC-MTDC systems, a new concept called the line level is introduced. This concept represents how many grounded capacitor buses will pass through from the investigated line to the fault point. Here are the steps to define the line level in this system. Firstly, the fault line takes a line level of 0. Secondly, the lines connected with the fault line take a line level of 1. Then, the line level of other lines connected with Level 1

line(s) is 2, and so on.

For general VSC-MTDC systems presented in Fig. 4-7, the fault component current of the fault line is determined based on (4-10), and those of the other lines are calculated based on (4-11) in the increasing order of the line level. Therefore, the fault component current of the generic VSC-MTDC system is written as follows based on the HFE model.

$$\begin{cases} i_{bfi0}^{H}(s)=\dfrac{u_n/s}{R_{i0}+s\left(L_{li0}+L_{Tik}\right)+1/sC_{ci}} \\ i_{bfij}^{H}(s)=i_{bfi0}^{H}(s)\prod_{l=1}^{L}h_l(s) \end{cases} \tag{4-22}$$

where $L$ is the line level of Line $ij$. $h_l$ is the second-order low-pass filter of a line with the level of $l$, which has the following form.

$$h_l(s)=1/s^2L_{bij}C_{ci}$$

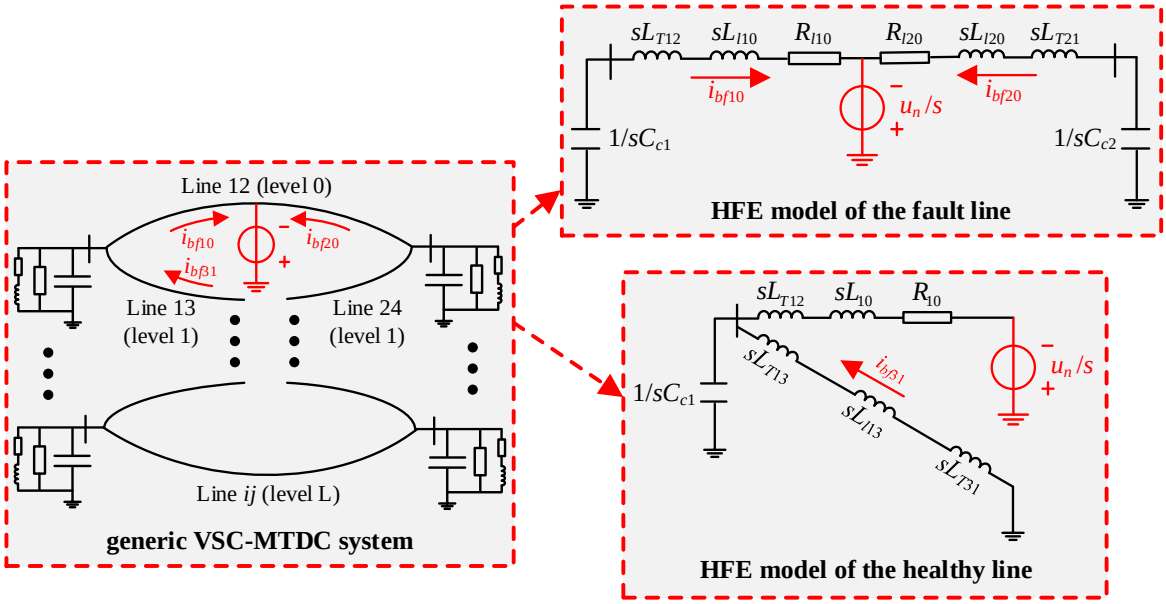


Fig. 4-7 Fault calculation of generic VSC-MTDC system based on the HFE model.

## 4.4.2 Analytical Time-Domain Fault Current Expression

Based on (4-6), the grounded capacitor $C_{ci}$ and the branch resistance $R_{i0}$ in (4-22) can be further neglected in the high-frequency domain so that the fault component current of the fault line is reduced as,

$$i_{bfi0}^{H}(s)=\frac{u_n}{s^2\left(L_{li0}+L_{Tik}\right)} \tag{4-23}$$

By applying the inverse Laplace transform on (4-23), the time-domain expression of the fault component current of the fault line during the initial fault period is deduced as,

$$i_{bfi0}(t)=\mathcal{L}^{-1}\left(i_{bfi0}^{H}(s)\right)=\frac{u_n}{L_{li0}+L_{Tik}}t \tag{4-24}$$

where $\mathcal{L}^{-1}(\cdot)$ denotes the inverse Laplace transform.

Combined with (4-22) and (4-23), the fault component current of the healthy line with level 1 can be reduced as,

$$i_{bfij}^{H}(s)=i_{bfi0}^{H}(s)h(s)=\frac{u_n}{s^4\left(L_{li0}+L_{Tik}\right)L_{bij}C_{ci}} \tag{4-25}$$

By calculating the inverse Laplace transform of (4-25), the fault component current of the healthy line is expressed as follows within the initial fault period.

$$i_{bfij}(t)=\mathcal{L}^{-1}\left(i_{bfij}^{H}(s)\right)=\frac{u_n}{6\left(L_{li0}+L_{Tik}\right)L_{bij}C_{ci}}t^3 \tag{4-26}$$

It can be seen from (4-24) and (4-26) that the proposed HFE model effectively reduces the original complex network for the DC fault analysis, so that the approximate expressions of the fault component current of the fault and healthy lines can be clearly presented. In addition, it is revealed that the fault line current surges linearly, while the healthy line current increases cubically within the first milliseconds after the DC fault.

Compared with the state-space method, the HFE-based fault analysis can significantly reduce the complexity of the network, such that concise expressions of the fault current are derived. Its main advantages include high efficiency and the capability to provide general rules of the fault current in the initial fault period.

### 4.4.3 Fault Current Calculation Considering Fault Resistance

The core idea of the HFE model is irrelevant to the fault type, and thus the HFE model is also applicable to DC faults with a fault resistance. Fig. 4-8 depicts the equivalent circuits of the fault line with a fault resistance based on the HFE model. Similar to the analysis of the meshed VSC-MTDC grid, the original circuit is open-looped at the fault point. Accordingly, two decomposed circuits for the DC fault calculation are formed, as ilstrated by Fig. 4-8.

The fault resistance $R_f$ is decomposed into two equivalent resistances noted as $R_{fi0}$ and $R_{fk0}$, which satisfy the following equations.

$$\begin{cases} R_{fi0}=\dfrac{i_{bfi0}+i_{bfk0}}{i_{bfi0}}R_f=\left(1+r_{bki}\right)R_f \\ R_{fk0}=\dfrac{i_{bfi0}+i_{bfk0}}{i_{bk0}}R_f=\left(1+\dfrac{1}{r_{bki}}\right)R_f \end{cases} \tag{4-27}$$

where $r_{bki}$ is the ratio between the fault component current of Branch $k0$ and Branch $i0$.

Based on the decomposed circuits in Fig. 4-8, the fault current of Branch $i0$ and that of Branch $k0$ are expressed as,

$$\begin{cases} i_{bfi0}^{H}(s) = \dfrac{u_n}{s\left(s\left(L_{li0}+L_{Tik}\right)+R_{li0}+R_{fi0}\right)} \\ i_{bfk0}^{H}(s) = \dfrac{u_n}{s\left(s\left(L_{lk0}+L_{Tki}\right)+R_{lk0}+R_{fk0}\right)} \end{cases} \tag{4-28}$$

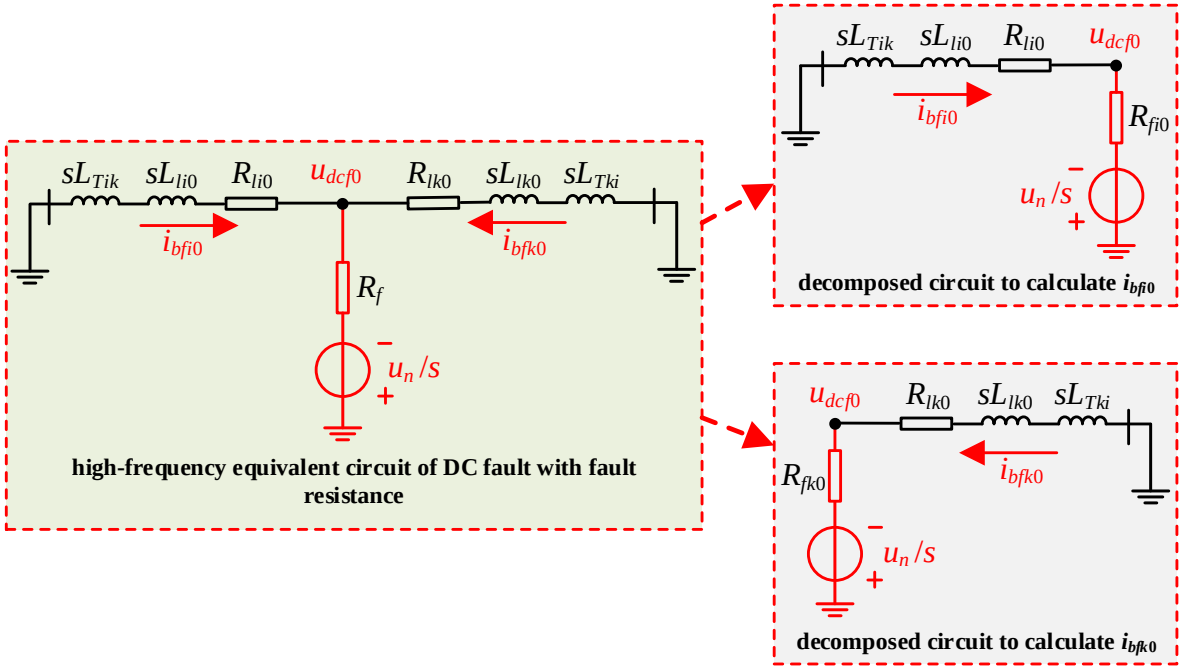


Fig. 4-8 High-frequency equivalent circuits for fault analysis considering fault resistance.

Based on (4-28), $r_{bki}$ is simplified in the high-frequency domain as,

$$r_{bki} = \frac{i_{bfk0}}{i_{bfi0}} \approx \frac{s\left(L_{li0}+L_{Tik}\right)+R_{li0}+R_{fi0}}{s\left(L_{lk0}+L_{Tki}\right)+R_{lk0}+R_{fk0}} \approx \frac{L_{li0}+L_{Tik}}{L_{lk0}+L_{Tki}} = \frac{L_{bi0}}{L_{bk0}} \tag{4-29}$$

Substitution of (4-27) and (4-29) into (4-28), the fault component current of the fault line is derived as,

$$i_{bfi0}^{H}(s) = \frac{u_n}{s\left(sL_{bi0}+R_{li0}+\left(1+r_{bki}\right)R_f\right)} = \frac{u_n}{s\left(sL_{bi0}+R_{li0}+\left(L_{bik}/L_{bk0}\right)R_f\right)} \tag{4-30}$$

Applying the inverse Laplace transform on (4-30), the fault component current of the fault line considering the fault resistance is expressed as,

$$i_{bfi0}(t) = \mathcal{L}^{-1}\left(i_{bfi0}^{H}(s)\right) = \frac{u_n}{R_{li0}+\left(L_{bik}/L_{bk0}\right)R_f}\left(1-\mathrm{e}^{-\frac{R_{li0}+\left(L_{bik}/L_{bk0}\right)R_f}{L_{bi0}}t}\right) \tag{4-31}$$

Based on (4-31), the fault component current of the fault line exhibits a typical time response of a one-order system when considering the fault resistance.

## 4.5 Case Studies

To manifest the effectiveness of the proposed initial DC fault calculation based on the HFE model, simulation studies are conducted in a radial and a meshed VSC-MTDC system, respectively. Specifically, the fault responses with three models are compared, namely, the detailed EMTP simulation model, the switching converter model with transmission lines represented by the π-section model (referred to as the RL model), and the HFE model.

### 4.5.1 Radial VSC-MTDC System

Fig. 4-9 shows the test radial four-terminal VSC-HVDC system. Three offshore wind farms and a main onshore system are connected via submarine cables. At the terminal of each cable, DC reactors of 100 mH are installed to suppress the fault current surge.

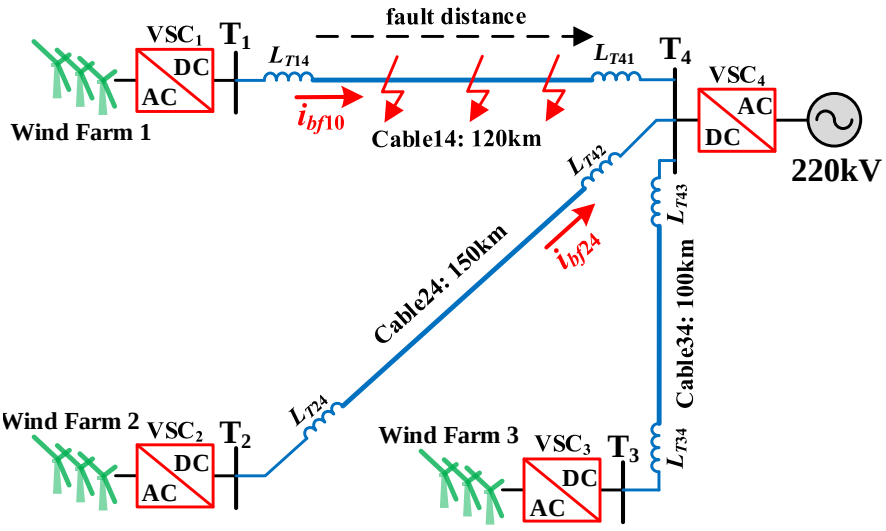


Fig. 4-9 Schematic of the test radial four-terminal VSC-HVDC system.

As shown in Table 4-1, the nominal DC-link voltage of the test radial VSC-MTDC system is ±200 kV. The DC-link capacitor of VSCs is 800 μF, and the short circuit ratio (SCR) of each AC system is 5.6. The classic master-slave scheme is adopted in the test system, i.e., the three wind farm integration converters adopt the CPC, while the onshore converter adopts the CDVC. The main control parameters are provided in Table 4-1. The sampling frequency is chosen as 10 kHz.

Table 4-1 Main parameters of the test radial MTDC system

| Symbol | Item | Value |
|---|---|---|
| $u_n$ | Nominal DC-link voltage of the test system | ±200 kV |
| $\omega_s$ | Nominal frequency of AC grids | 50 Hz |
| SCR | AC side system SCR | 5.6 |
| $C_{ci}$ | DC-link capacitance of VSCs | 800 μF |
| $\sigma_i$ | Time constant of the inner loop | 2 ms |
| ($K_{Po}$, $K_{Io}$) | Proportional and integral gains of the CPC | (1, 10) |
| ($K_{Pv}$, $K_{Iv}$) | Proportional and integral gains of the CDVC | (1, 10) |
| $L_T$ | Inductance of DC reactors | 100 mH |
| $R_0$ | Per-kilometre resistance of DC cable | 0.083 Ω |
| $L_0$ | Per-kilometre inductance of DC cable | 0.1 mH |
| $f_s$ | Sampling frequency | 10 kHz |

Fig. 4-10 depics the dynamics of the fault component current of the test radial MTDC system during metallic DC faults. As depicted in Fig. 4-10 (a), when a metallic fault occurs at the terminal of Cable 14 (close near T4), the fault component current of the faulty cable (Cable 14) with EMTP simulation rapidly rises around 0.8 ms following the fault occurrence because of the travelling wave process. To compare the models fairly, a time delay of 0.8 ms is added to the fault curves with the lumped parameter line models (the RL model and the HFE model) to compensate for the travelling wave propagation process. Under the RL model and the HFE model, the fault component current of Cable 14 has the same trend. As for the EMTP simulation model, the corresponding fault component current of Cable 14 vibrates little around those with the RL and HFE models. Fig. 4-10 (b) shows the dynamics of the fault component current of Cable 14 when a metallic fault occurs at 100 km and 20 km away from the terminal of Cable 14 (adjacent to T1). As the fault distance increases, the travelling wave effect becomes more apparent and leads to fluctuation of the fault component current of Cable 14 with EMTP simulation. The fault component currents of the fault line with the three models involved are rather approximate, manifesting the accuracy of the proposed HFE model for the analysis of DC fault current responses within several milliseconds after the fault. When a metallic fault occurs at the terminal of Cable 14, the travelling wave process is negligible for the healthy Cable 24, as illustrated by Fig. 4-10 (c), resulting in nearly the same fault component current curves with three different models involved. Fig. 4-10 (d) depicts the fault component current of the healthy line with different fault distances. Still, the fault component

currents of the healthy line with the three models involved are rather approximate due to the weak travelling wave process in Cable 24. These simulation results verify that as per the HFE model, the initial DC fault current can be determined by solving simple RLC circuits in radial MTDC systems.

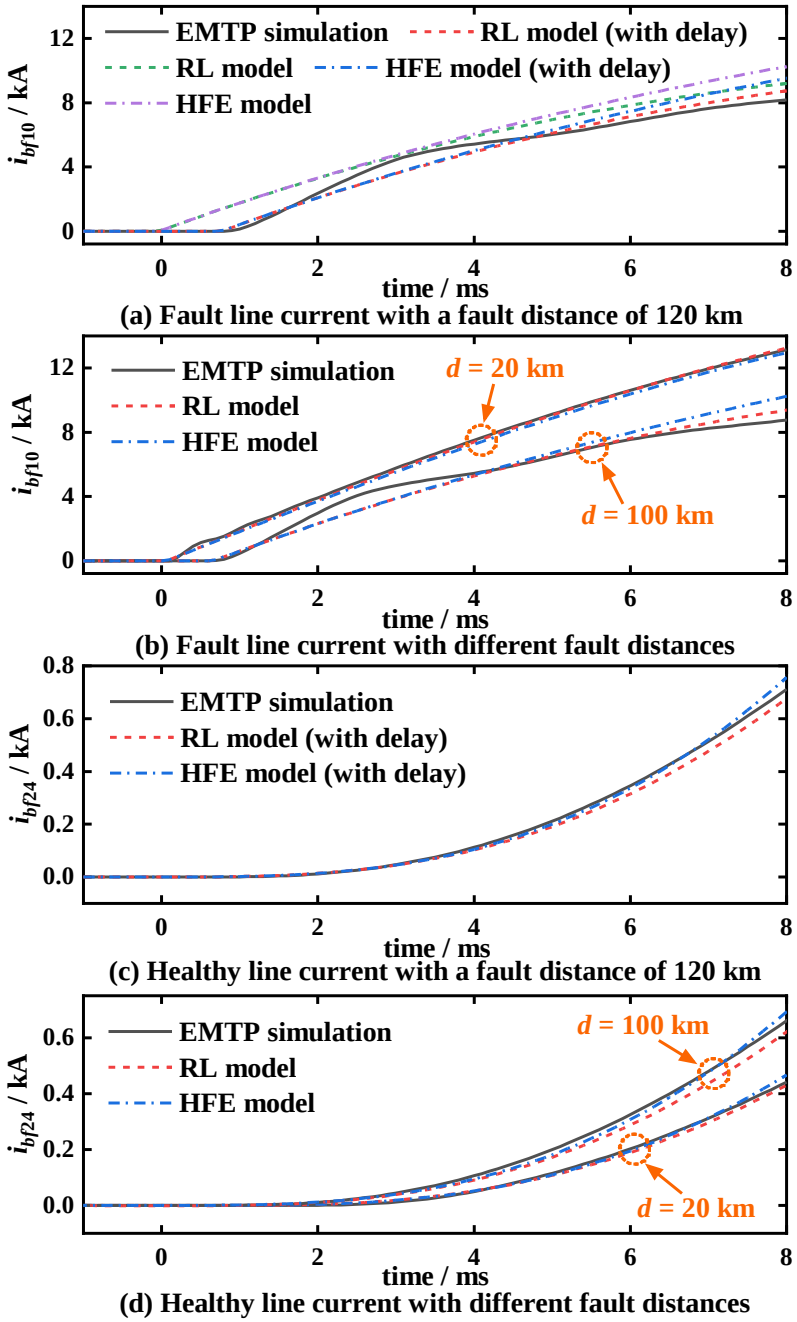


Fig. 4-10 Fault component current of the test radial MTDC system under metallic DC faults.

Fig. 4-11 depicts the dynamics of the fault component current of the fault line when high-resistance DC faults occur on Cable 14. As illustrated by Fig. 4-11 (a), the fault component current descends with the increase of the fault distances. Compared with Fig. 4-11 (a) and (b),

it is found that the fault component current decreases as the fault resistance increases. In addition, the fault component current with EMTP simulation exhibits clear oscillations compared to that with the RL and HFE models due to the travelling waving effect. Nevertheless, the errors are in an acceptable range. Fig. 4-11 verifies that the proposed HFE model is effective for the initial DC fault calculation considering the fault resistance.

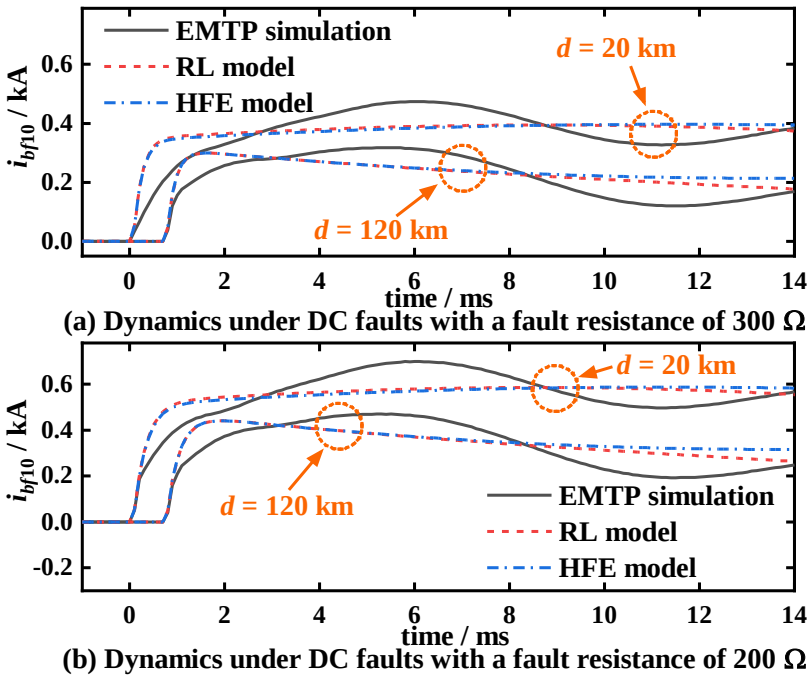


Fig. 4-11 Fault component current of the test radial MTDC system under high-resistance DC faults.

### 4.5.2 Meshed VSC-MTDC System

To verify the effectiveness of the proposed HFE model for meshed VSC-MTDC systems, a four-terminal grid is built in PSCAD/EMTDC, as illustrated by Fig. 4-12. Table 4-2 presents the main parameters of the test meshed four-terminal HVDC system. The nominal DC-link voltage of the test system is ±200 kV. The inductance of the implemental DC inductors at each terminal of DC overhead transmission lines is 100 mH. The DC-link capacitor voltage of VSCs is 880 μF, and the short circuit ratio SCR of each AC system is 5.6. $VSC_1$, $VSC_3$, and $VSC_4$ regulate their active and reactive power. In contrast, $VSC_2$ regulates the DC-link voltage and the exchange of reactive power with the connected AC system. The control parameters of VSCs are the same as those of the test radial VSC-MTDC system, which can be referred to in Table 4-1.

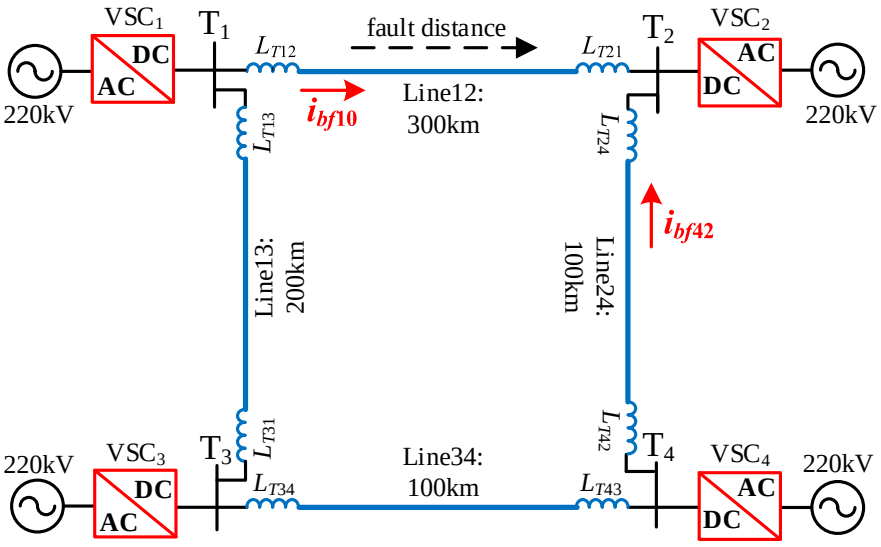


Fig. 4-12 Schematic of the test meshed four-terminal VSC-HVDC system.

Table 4-2 Main parameters of the test meshed MTDC system

| Symbol | Item | Value |
|---|---|---|
| $u_n$ | Nominal DC-link voltage of the test system | ±200 kV |
| $\omega_s$ | Nominal frequency of AC grids | 50 Hz |
| SCR | AC side system SCR | 5.6 |
| $C_{ci}$ | DC-link capacitor voltage of VSCs | 880 μF |
| $L_T$ | Inductance of DC reactors | 100 mH |
| $R_0$ | Per-kilometre resistance of DC cable | 0.015 Ω |
| $L_0$ | Per-kilometre inductance of DC cable | 1.635 mH |
| $f_s$ | Sampling frequency | 10 kHz |

Fig. 4-13 depicts the dynamics of the fault component current of the fault line when metallic faults occur on the test meshed four-terminal VSC-HVDC system. Fig. 4-13 (a) illustrates the fault line current when a metallic fault occurs at the terminal of Line 12 (close near $T_2$). As can be seen, the fault line current rapidly surges after the occurrence of the DC fault. In addition, the fault component current curves with the RL and HFE models are close to each other, which almost increases linearly with respect to time. This is in line with the analysis results expressed by (4-24). The fault component current curve with EMTP simulation exhibits the travelling wave propagation process. Delaying the fault component current curve with the RL model around 1 ms to compensate for the travelling wave propagation delay, it is observed that the fault component current with EMTP simulation

fluctuates around the delayed curve. This indicates that the lumped parameter models (the RL and HFE models) can represent the average behaviour of the distributed model.

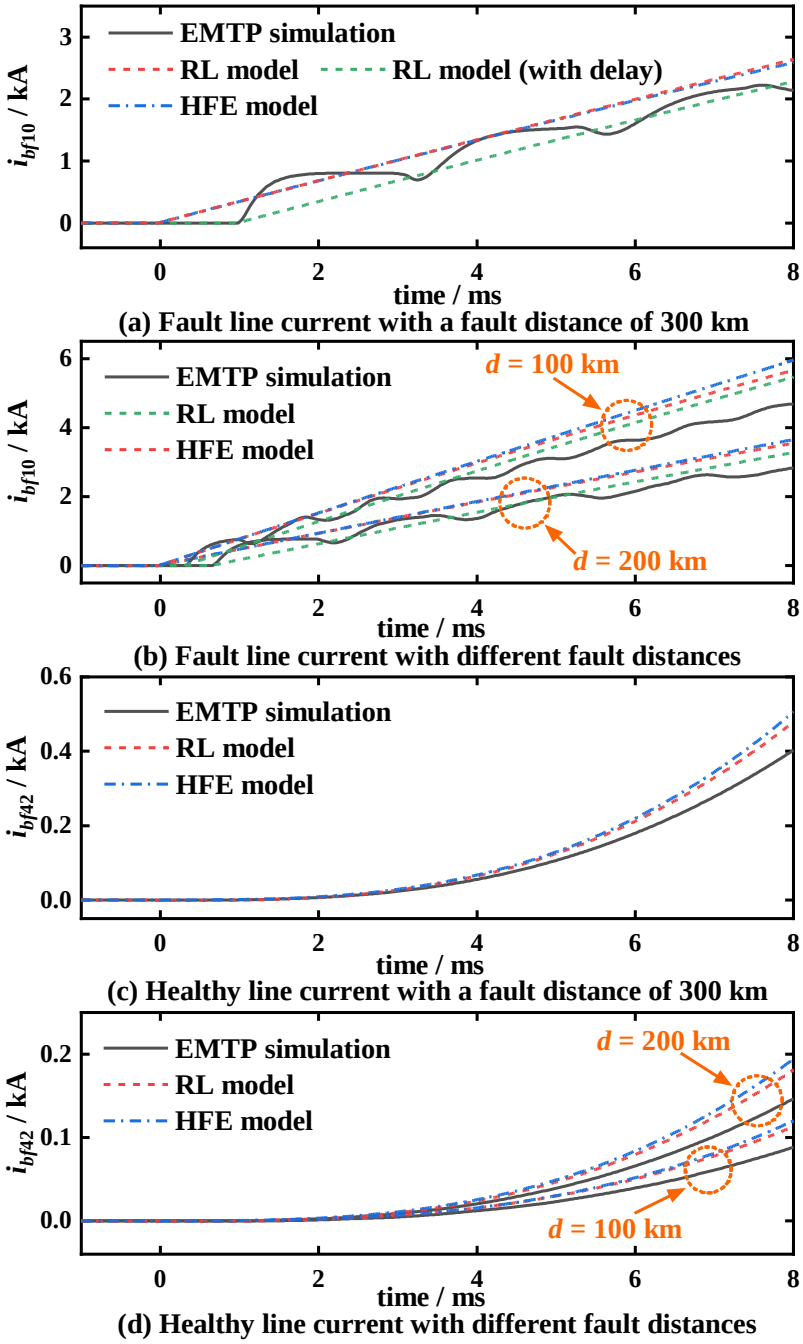


Fig. 4-13 Fault component current of the test meshed MTDC system under metallic DC faults.

Fig. 4-13 (b) depicts the fault line current with different fault distances. It is seen that the fault component current of the fault line decreases with the increase in the fault distance. With the EMTP simulation model, it is observed that the travelling wave process becomes weaker with the increase in the fault distance. With the RL and HFE models, the fault component current curves linearly rise with very similar speeds. The errors between the three models are

in an acceptable range, which validates the effectiveness of the proposed HFE model for the initial DC fault calculation. As for the fault component current of the healthy line (Line 24), it is shown in Fig. 4-13 (c) that it increases much slower than that of the fault line. Since the line boundary composed by the DC supplementary reactor and the DC-link capacitor serves as a second-order low-pass filter, the travelling wave process becomes almost invisible when it propagates into the healthy line. As a result, the fault component current curves with the three models are very close. Fig. 4-13 (d) illstrates the healthy line current with different fault distances. With the increases in the fault distance, the fault point becomes closer to the healthy line, leading to the increase of the fault component current of the healthy line. Based on the fault current curves with different models under different fault distances, it is concluded that the proposed fault calculation method based on the HFE model has accuracy within the initial period after the DC fault.

Fig. 4-14 depicts the dynamics of the fault component current of the fault line under high-resistance faults. As illustrated by Fig. 4-14 (a), the fault component current increases rapidly for around 1 ms and soon tends to a constant value, which is in line with the analysis result as expressed by (4-31). When the fault distance increases, there is a significant reduction in the fault component current. In addition, it is observed from the curve with EMTP simulation denoted by the solid black line that it takes a longer time for the fault travelling wave to arrive at the measurement point. On the whole, the fault component current with EMTP simulation fluctuates around that of the RL model, while the fault component current curves with the RL and HFE models are almost the same. It verifies the accuracy of the proposed HFE model for the DC fault analysis of the meshed VSC-MTDC system. Fig. 4-14 (b) shows the dynamics of the fault line current when the fault resistance decreases from 200 Ω to 100 Ω. The overall features of the fault component curve with the three models are similar to those illustrated by Fig. 4-14 (a). Compared with Fig. 4-14 (a) and (b), it is indicated that the fault component current increases as the fault resistance decreases. The fault current curves with EMTP simulation fluctuate around those of the RL and HFE models, validating the applicability of the proposed HFE-based fault analysis method for meshed VSC-MTDC system with the consideration of fault resistance.

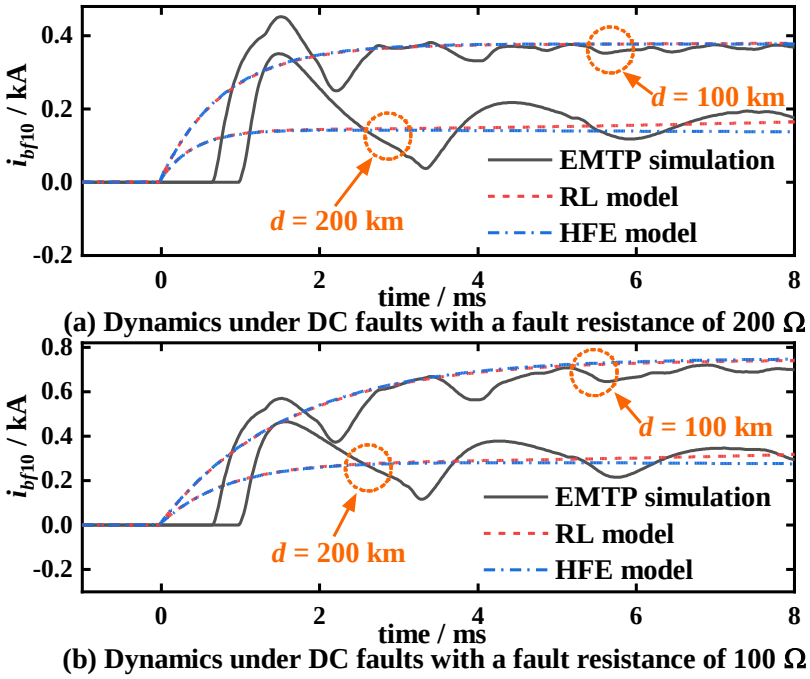


Fig. 4-14 Fault component current of the test meshed MTDC system under high-resistance DC faults.

## 4.6 Summary

This chapter proposes a simple and efficient method for the approximate fault calculation of VSC-MTDC systems by using the HFE model. Considering the high-frequency electrical quantities dominate in the fault component Laplace circuit within the first milliseconds after the fault, the low-frequency components of the Laplace circuit can be omitted to simplify the initial fault analysis, which is referred to as the HFE model. As per the HFE model, it is found that the parallel connected branches with the grounded capacitor can be overlooked when calculating the fault component current of the fault line, while the fault component current of the healthy line equals that of the fault line times a second-order low-pass LC filter. It reveals that the fault component current of the fault line rises approximately linearly, while that of the healthy line increases approximately cubically within several milliseconds after the DC fault. Simulation studies have validated the accuracy of the proposed DC fault calculation method based on the HFE model in both radial and meshed VSC-MTDC systems.

# 5 DC-Side Damping Properties and Small-Signal Stability Analysis of Different Types of Converters

## 5.1 Introduction

The dynamic behaviours of MTDC systems under fault conditions have been studied in the last two chapters. In the following, the dynamics of MTDC systems under normal conditions perturbed by a disturbance will be investigated. Specifically, the stability issue determining whether the system can restore to steady-state operation after perturbations is of interest. There are DC-link capacitors, supplementary DC reactors, and DC transmission lines in the DC network. Accordingly, the energy exchanges between inductance and capacitance components can introduce natural resonance frequencies to the DC system. If the controllers of converters cannot provide sufficient damping within the resonant frequency band, there will exhibit low-frequency oscillations in the DC-link current, which may lead to the alarm of monitoring devices or even the blocking of converters. This new stability issue originating from the DC link is called DC-side stability, which is particularly important for the stable operation of MTDC systems. In addition, when subjected to large disturbances causing significant DC-link voltage derivations, the power transmission of the DC link will be interrupted, and the DC system should be restarted. Therefore, this thesis only concentrates on small-signal disturbances that do not lead to a large change in the DC-link voltage.

Modal analysis is a classic method used for small-signal stability analysis, which involves examining the eigenvalues of the system state matrix. It can determine the small-signal stability of the studied system under specified operating conditions. [79] reports the harmonic transfer function of the MMC, which considers the detailed harmonic dynamics of the MMC. The stability issue highly relevant to harmonic dynamics is called harmonic stability. The interactions between MMCs in a point-to-point HVDC system are investigated based on the relative gain array (RGA) in [80]. Nevertheless, modal analysis requires detailed system parameters to form the system matrix and comparably elaborate iterative numerical calculations to obtain the eigenvalues. In addition, it is hard to derive analytical stabilising conditions for a high-order system based on modal analysis, making the instability mechanism of the studied system unclear.

The impedance-based method has gained popularity for the stability analysis of converter systems recently. The studied system is split into a source subsystem and a load subsystem.

Then, the Nyquist criterion is applied to the ratio of the impedances of these subsystems to determine the stability of the studied system. Instead of requiring detailed parameters of physical and control systems, the impedance-based approach concentrates on the external behaviours of the subsystems, which can be determined via external measurement. In [83] and [84], the impedances of the TLVSC from the AC and DC sides are derived. By using the net-damping criterion, the influences of the source and load subsystems on the system stability are assessed in [86]. [87] points out that under certain operating conditions, the VSC may exhibit nonpassive properties, and DC-side instability may appear once the VSC amplifies the resonances in the DC grid. It is found in [89] that DC-side stability could degrade as the proportional gain of the CDVC increases, but the feasible range of the control parameter to guarantee DC-side stability is not provided. Besides, since the impedance matrices include internal dynamics of several coupling control loops, the impedance computation could be rather complex, making it hard to reveal the DC-side instability mechanism in DC networks based on the impedance-based method.

Passivity analysis is another approach that is widely used in stability analysis. To address the instability arised from resonances, the TLVSC is tuned to possess passive input admittance in [91]. In [92], the choose of the dividing point of a point-to-point HVDC link is discussed to form the two subsystems. As per passivity analysis, the conductance of VSCs should be positive to suppress the resonances in the network. However, concise expressions bridging system stability and critical parameters of physical and control systems cannot be directly obtained via passivity analysis.

Existing methods based on eigenvalue calculation or Nyquist plot only provide numerical solutions to the small-signal stability of DC systems. As a result, the stability analysis involves relatively complicated calculations, and the instability mechanism lacks clear physical interpretations. To tackle this, the DC-side damping properties of different converters are first investigated in this chapter. By focusing on the dynamic behaviours in the neighbourhood of the dominant oscillation frequency, which is referred to as dominant frequency analysis (DFA), the impacts of control parameters on the DC-side damping of the converter can be evaluated via simple and direct calculation. Subsequently, the DC-side stability of the two-terminal VSC-based DC link is studied. An analytical stabilising condition of the system is derived based on DFA, which reveals the instability mechanism of the DC link under joint actions of different VSCs.

## 5.2 DC-Side Damping Properties of the LCC

The system shown in Fig. 5-1 is utilised to investigate the DC-side damping properties of converters with different topologies and control modes, where a single converter connects to an ideal DC source via a DC transmission line. The transmission line is represented by the classic RL model, which is sufficiently accurate for the stability analysis because the oscillatory frequencies in the DC link fall into the feasible frequency band of the RL line model. $R_l$ and $L_l$ are the resistance and inductance of the DC line, respectively. The terminal voltage of the ideal DC source is regulated to the nominal DC-link voltage $u_n$.

Based on the derived model of the LCC-based rectifier shown in Fig. 2-3, the equivalent circuit of an LCC-based rectifier to an ideal DC source system is illustrated by Fig. 5-2. Accordingly, the system equations are written as,

$$\begin{cases} C_{eq}^{LCC}\dfrac{\mathrm{d}u_d}{\mathrm{d}t} = -i_{dc} \\ L_b\dfrac{\mathrm{d}i_{dc}}{\mathrm{d}t} = u_d - u_n - R_b i_{dc} \end{cases} \tag{5-1}$$

where $R_b$ and $L_b$ are the equivalent resistance and inductance of the branch, and $R_b = R_{eq}^{LCC} + R_l$, $L_b = L_d + L_l$.

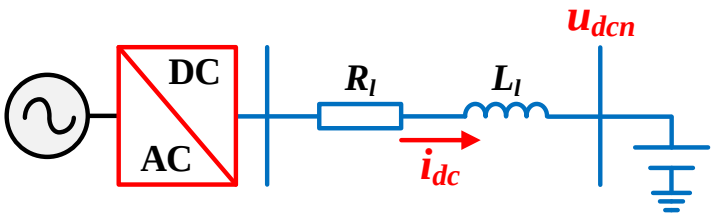


Fig. 5-1 Schematic of a single converter connected to an ideal DC bus.

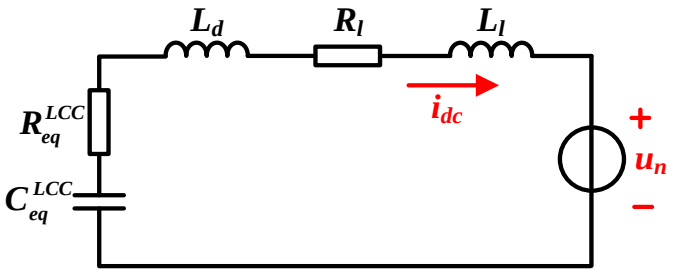


Fig. 5-2 Equivalent circuit of an LCC to an ideal DC source system.

Considering $u_n$ is constant, the small-signal form of (5-1) can be expressed as,

$$\frac{\mathrm{d}}{\mathrm{d}t}\begin{bmatrix}\Delta u_d\\ \Delta i_{dc}\end{bmatrix}=\begin{bmatrix}0 & -\dfrac{1}{C_{eq}^{LCC}}\\ -\dfrac{1}{L_b} & -\dfrac{R_b}{L_b}\end{bmatrix}\begin{bmatrix}\Delta u_d\\ \Delta i_{dc}\end{bmatrix} \tag{5-2}$$

Based (5-2), the characteristic function of the LCC to an ideal DC source system is obtained as,

$$F(s)=\begin{vmatrix}s & \dfrac{1}{C_{eq}^{LCC}}\\ \dfrac{1}{L_b} & s+\dfrac{R_b}{L_b}\end{vmatrix}=s^2+\frac{R_b}{L_b}s+\frac{1}{L_bC_{eq}^{LCC}} \tag{5-3}$$

Based on (2-16) and (5-3), the natural oscillation frequency $\omega_n$ and the damping ratio $\zeta$ of the system are calculated as,

$$\begin{cases}\omega_n=\dfrac{1}{\sqrt{L_bC_{eq}^{LCC}}}=\sqrt{\dfrac{V_o\sin\alpha_0K_{Pc}}{L_b}}=\sqrt{\dfrac{V_o\sin\alpha_0K_{Pc}}{L_d+L_l}}\\ \zeta=\dfrac{R_b}{2\omega_nL_b}=\dfrac{R_b+V_o\sin\alpha_0K_{Pc}}{2\sqrt{L_bV_o\sin\alpha_0K_{Ic}}}=\dfrac{d_\gamma+R_l+V_o\sin\alpha_0K_{Pc}}{2\sqrt{(L_d+L_l)V_o\sin\alpha_0K_{Ic}}}\end{cases} \tag{5-4}$$

(5-4) indicates that the oscillation frequency in the DC link is related to the operating point, the transmission inductance, and the proportional gain of the constant current controller. The integral gain of the constant current control will not influence the oscillation frequency. In contrast, the damping ratio is relevant to the operating point, the transmission resistance and inductance, and the proportional and integral gains of the constant current controller. Additionally, (5-4) also implies that the LCC-based rectifier always provides positive damping as the damping ratio is positive. The DC-side damping of the LCC can be enlarged by increasing the proportional gain or reducing the DC-link voltage, the transmission inductance, and the integral gain of the constant current controller.

## 5.3 DC-Side Damping Properties of the VSC

### 5.3.1 CPC-Based VSC

According to the derived model of the CPC-based TLVSC illustrated by Fig. 2-6, the equivalent circuit of a CPC-based VSC to an ideal DC source system is illustrated by Fig. 5-3. The system equations are expressed as,

$$\begin{cases} C_c \dfrac{\mathrm{d}u_d}{\mathrm{d}t} = -\dfrac{1}{R_{eq}^{VSC}} u_d - i_{dc} \\ L_b \dfrac{\mathrm{d}i_{dc}}{\mathrm{d}t} = u_d - u_n - R_b i_{dc} \end{cases} \tag{5-5}$$

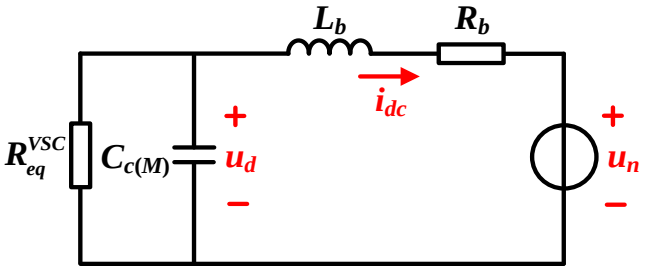


Fig. 5-3 Equivalent circuit of a CPC-based VSC to an ideal DC source system.

Compared with the equivalent circuits of the TLVSC and the MMC, as shown in Fig. 2-6, Fig. 2-7, and Fig. 2-10, it is found that the main difference between these two converters is that the MMC has DC-side equivalent resistance and inductance, which can be incorporated into the transmission resistance and inductance in the stability analysis. Accordingly, for the TLVSC, $R_b$ and $L_b$ in (5-5) are written as,

$$\begin{cases} R_b = R_l \\ L_b = L_T + L_l \end{cases}$$

As for the MMC, $R_b$ and $L_b$ in (5-5) are written as,

$$\begin{cases} R_b = R_M + R_l \\ L_b = L_M + L_T + L_l \end{cases}$$

Since the TLVSC and the MMC possess similar external characteristics, the TLVSC is adopted in the stability analysis for simplicity and without loss of generality.

Rewriting (5-5) in a small-signal form, it provides that,

$$\frac{\mathrm{d}}{\mathrm{d}t}\begin{bmatrix} \Delta u_d \\ \Delta i_{dc} \end{bmatrix} = \begin{bmatrix} -\dfrac{1}{R_{eq}^{VSC} C_c} & -\dfrac{1}{C_c} \\ \dfrac{1}{L_b} & -\dfrac{R_b}{L_b} \end{bmatrix} \begin{bmatrix} \Delta u_d \\ \Delta i_{dc} \end{bmatrix} \tag{5-6}$$

The characteristic function of the single CPC-based VSC to an ideal DC source system can be derived based on (5-6) as follows.

$$F(s)=\begin{vmatrix} s+\dfrac{1}{R_{eq}^{VSC}C_c} & \dfrac{1}{C_c} \\ -\dfrac{1}{L_b} & s+\dfrac{R_b}{L_b} \end{vmatrix}=s^2+\left(\frac{1}{R_{eq}^{VSC}C_c}+\frac{R_b}{L_b}\right)s+\left(\frac{R_b}{R_{eq}^{VSC}}+1\right)\frac{1}{L_bC_c} \tag{5-7}$$

Notice that with $R_{eq}^{VSC}=1/g_{d0}$, the natural oscillation frequency and the damping ratio of the DC link are calculated based on (5-7).

$$\begin{cases} \omega_n=\sqrt{\left(\dfrac{R_b}{R_{eq}^{VSC}}+1\right)\dfrac{1}{L_bC_c}}=\sqrt{\dfrac{R_bg_{d0}+1}{L_bC_c}}\approx\dfrac{1}{\sqrt{L_bC_c}} \\ \zeta=\dfrac{1}{2\omega_n}\left(\dfrac{1}{R_{eq}^{VSC}C_c}+\dfrac{R_b}{L_b}\right)=\dfrac{R_bC_c+L_bg_{d0}}{2\sqrt{L_bC_c\left(R_bg_{d0}+1\right)}}\approx\dfrac{R_bC_c+L_bg_{d0}}{2\sqrt{L_bC_c}} \end{cases} \tag{5-8}$$

Because of the small value of the equivalent DC-side conductance $g_{d0}$, we have $R_bg_{d0} \approx 1$. Consequently, the approximations in (5-8) can hold. (5-8) indicates that the oscillation frequency is determined by the transmission inductance of the DC link and the grounded capacitance of the VSC. The increase in the transmission inductance or the grounded capacitance will decrease the oscillation frequency. As for the damping ratio, it is also influenced by the transmission resistance and the operating point. Since $g_{d0}$ is negative when the VSC operates as an inverter, there is a risk of negative damping in the DC link. In addition, it is interesting to find from (5-8) that the oscillation frequency and the damping ratio are irrelevant to the control parameters of the CPC.

According to (5-8), the stability criterion of the single CPC-based VSC to an ideal DC source system can be expressed as,

$$\zeta>0 \quad \Rightarrow \quad R_bC_c+L_bg_{d0}>0 \tag{5-9}$$

(5-9) indicates that the CPC-based VSC rectifier provides positive damping to the DC link and will not result in oscillatory instability. In contrast, the DC link will be destabilised once the positive damping provided by the transmission resistance cannot offset the negative damping induced by the CPC-based inverter. Rearranging (5-9) provides that,

$$g_{d0}=\frac{i_{d0}}{u_{d0}}=\frac{P_{dc}}{u_{d0}^2}>-\frac{R_bC_c}{L_b} \quad \Rightarrow \quad P_{dc}>-\frac{R_bC_cu_{d0}^2}{L_b}=-P_{dc}^{cr} \tag{5-10}$$

(5-10) indicates that there is a critical transfer power for the CPC-based inverter. Once the active power of the VSC exceeds this critical value, the damping ratio will become negative, leading to divergent oscillation in the DC link.

### 5.3.2 CDVC-Based VSC

Based on the derived model of the CDVC-based VSC illustrated by Fig. 2-7, the equivalent circuit of a CDVC-based VSC to an ideal DC source system is shown in Fig. 5-4. The system equations are expressed as,

$$\begin{cases} C_c \dfrac{\mathrm{d}u_d}{\mathrm{d}t} = -\dfrac{1}{R_{eqp}^{VSC}} u_d - i_{dc} + i_{eq} \\ L_b \dfrac{\mathrm{d}i_{dc}}{\mathrm{d}t} = u_d - u_n - R_b i_{dc} \\ L_{eq}^{VSC} \dfrac{\mathrm{d}i_{eq}}{\mathrm{d}t} = -u_d - R_{eqs}^{VSC} i_{eq} \end{cases} \tag{5-11}$$

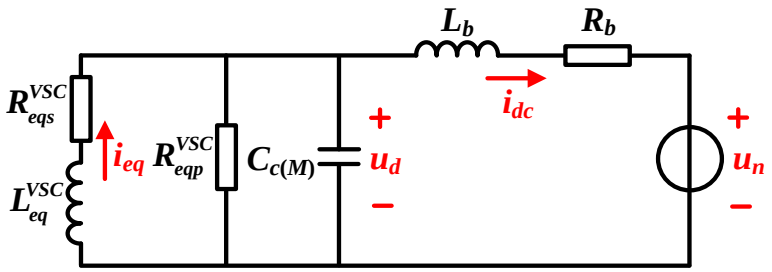


Fig. 5-4 Equivalent circuit of a CDVC-based VSC to an ideal DC source system.

It is observed from (5-11) that the single CDVC-based VSC to an ideal DC source system is a three-order dynamic system, making it difficult to derive a concise analytical stability criterion for such a system. Note that the dominant oscillation modes that possess low damping ratios determine the small-signal stability of the system. Accordingly, the other modes can be simplified by reserving only the behaviours nearby the dominant frequency intact. In this way, the model reduction can be achieved without losing primary stability characteristics. The model reduction is called DFA in this thesis. Based on DFA, the natural oscillation mode of the system should be first determined, and the impacts of other factors will be introduced subsequently.

Compared with Fig. 5-3 and Fig. 5-4, it is found that the main difference between the CPC and CDVC-based VSCs is the CDVC-based VSC has an additional branch representing the control effect. Therefore, the natural oscillation mode of these two systems is the same, which is mainly determined by the physical system.

The impacts of the CDVC is written below by applying Laplace transform to the third equation in (5-11).

$$\Delta i_{eq} = -\frac{1}{sL_{eq}^{VSC} + R_{eqs}^{VSC}} \Delta u_d = -G_{eq}(s)\Delta u_d \tag{5-12}$$

Combined with (5-11) and (5-12), the small-signal model of the single VSC to an ideal DC source system considering the CDVC effects can be obtained as,

$$\frac{\mathrm{d}}{\mathrm{d}t}\begin{bmatrix}\Delta u_d \\ \Delta i_{dc}\end{bmatrix} = \begin{bmatrix} -\dfrac{g_{d0} + G_{eq}(s)}{C_c} & -\dfrac{1}{C_c} \\ \dfrac{1}{L_b} & -\dfrac{R_b}{L_b} \end{bmatrix}\begin{bmatrix}\Delta u_d \\ \Delta i_{dc}\end{bmatrix} \tag{5-13}$$

Based on (5-13), the characteristic function of the single CDVC-based VSC to an ideal DC source system is written as,

$$F(s) = \begin{vmatrix} s + \dfrac{g_{d0} + G_{eq}(s)}{C_c} & \dfrac{1}{C_c} \\ -\dfrac{1}{L_b} & s + \dfrac{R_b}{L_b} \end{vmatrix} = s^2 + \left(\frac{R_b}{L_b} + \frac{g_{d0} + G_{eq}(s)}{C_c}\right)s + \frac{R_b\left(g_{d0} + G_{eq}(s)\right) + 1}{L_b C_c} \tag{5-14}$$

Substitution of $s = j\omega_n$ into (5-14), the characteristic function can be simplified as follows in the vicinity of the dominant frequency.

$$F(s) = s^2 + a_1 s + a_0 \tag{5-15}$$

where,

$$\begin{cases} a_1 = \dfrac{R_b}{L_b} + \dfrac{g_{d0} + \mathrm{Re}\left(G_{eq}(j\omega_n)\right)}{C_c} + \dfrac{R_b\,\mathrm{Im}\left(G_{eq}(j\omega_n)\right)}{L_b C_c \omega_n} \\ a_0 = \dfrac{R_b g_{d0} + 1 + R_b\,\mathrm{Re}\left(G_{eq}(j\omega_n)\right)}{L_b C_c} - \dfrac{\mathrm{Im}\left(G_{eq}(j\omega_n)\right)\omega_n}{C_c} \end{cases} \tag{5-16}$$

Substituting the natural frequency expressed by (5-8) into $G_{eq}(j\omega_n)$, it yields that,

$$\begin{cases} \mathrm{Re}\left(G_{eq}(j\omega_n)\right) = \dfrac{R_{eqs}^{VSC}}{\left(R_{eqs}^{VSC}\right)^2 + \omega_n^2\left(L_{eq}^{VSC}\right)^2} = \dfrac{R_{eqs}^{VSC} L_b C_c}{\left(R_{eqs}^{VSC}\right)^2 L_b C_b + \left(L_{eq}^{VSC}\right)^2} \\ \mathrm{Im}\left(G_{eq}(j\omega_n)\right) = -\dfrac{\omega_n L_{eq}^{VSC}}{\left(R_{eqs}^{VSC}\right)^2 + \omega_n^2\left(L_{eq}^{VSC}\right)^2} = -\dfrac{L_{eq}^{VSC}\sqrt{L_b C_c}}{\left(R_{eqs}^{VSC}\right)^2 L_b C_b + \left(L_{eq}^{VSC}\right)^2} \end{cases} \tag{5-17}$$

Combined with (5-16) and (5-17), it provides that,

$$\begin{cases} a_1 = \dfrac{R_b}{L_b} + \dfrac{g_{d0}}{C_c} + \dfrac{R_{eqs}^{VSC} L_b - R_b L_{eq}^{VSC}}{\left(R_{eqs}^{VSC}\right)^2 L_b C_c + \left(L_{eq}^{VSC}\right)^2} \\ a_0 = \dfrac{R_b g_{d0} + 1}{L_b C_c} + \dfrac{R_b R_{eqs}^{VSC}}{\left(R_{eqs}^{VSC}\right)^2 L_b C_c + \left(L_{eq}^{VSC}\right)^2} + \dfrac{L_{eq}^{VSC}}{C_c\left(\left(R_{eqs}^{VSC}\right)^2 L_b C_c + \left(L_{eq}^{VSC}\right)^2\right)} \end{cases} \tag{5-18}$$

Substitution of (2-44) into (5-18) and notice that with the small value of the time constant of the inner loop denoted by $\sigma_i$, the coefficients are expressed as,

$$\begin{cases} a_1 = \dfrac{R_b}{L_b} + \dfrac{g_{d0}}{C_c} + \dfrac{L_b - R_b\sigma_i}{\left(2u_{d0}/3u_s^d K_{Pv}\right)\left(L_b C_c + \sigma_i^2\right)} \approx \dfrac{R_b}{L_b} + \dfrac{1}{C_c}\left(g_{d0} + \dfrac{3u_s^d K_{Pv}}{2u_{d0}}\right) \\ a_0 = \dfrac{R_b g_{d0} + 1}{L_b C_c} + \dfrac{1}{\left(2u_{d0}/3u_s^d K_{Pv}\right)\left(L_b C_c + \sigma_i^2\right)}\left(R_b + \dfrac{\sigma_i}{C_c}\right) \approx \dfrac{1}{L_b C_c}\left(1 + \dfrac{3u_s^d K_{Pv} R_b}{2u_{d0}} + \dfrac{3u_s^d K_{Pv}\sigma_i}{2u_{d0} C_c}\right) \end{cases} \tag{5-19}$$

(5-19) indicates that $a_0$ is always positive. To ensure the stability of the system, $a_1$ should be positive, which provides,

$$a_1 > 0 \quad \Rightarrow \quad K_{Pv} > \frac{2u_{d0}}{3u_s^d}\left(-g_{d0}\right) - \frac{2u_{d0} R_b C_c}{3u_s^d L_b} \tag{5-20}$$

Deonte $P_{dc}^{cap}$ as the transmission capacity of the DC link, and the minimum proportional gain of the CDVC for ensuring stability can be obtained based on (5-20).

$$K_{Pv} > K_{Pv}^{\min} = \frac{2u_{d0}}{3u_s^d}\left(\frac{P_{dc}^{cap}}{u_{d0}^2}\right) - \frac{2u_{d0} R_b C_c}{3u_s^d L_b} = \frac{2P_{dc}^{cap}}{3u_s^d u_{d0}} - \frac{2u_{d0} R_b C_c}{3u_s^d L_b} \tag{5-21}$$

(5-21) indicates that the CDVC-based VSC to an ideal DC source system is stable if the proportional gain $K_{Pv}$ is less than $K_{Pv}^{\min}$. Actually, $K_{Pv}^{\min}$ is rather small based on (5-21) such that the CDVC-based VSC with typical parameters can always keep stable.

In addition, the dominated oscillation frequency denoted by $\omega_d$ and the damping ratio of the single CDVC-based VSC to an ideal DC source system can be calculated as follows based on (5-19).

$$\begin{cases} \omega_d = \dfrac{1}{\sqrt{L_b C_c}}\sqrt{1 + \dfrac{3u_s^d K_{Pv} R_b}{2u_{d0}} + \dfrac{3u_s^d K_{Pv}\sigma_i}{2u_{d0} C_c}} \\ \zeta = \dfrac{a_1}{2\omega_d} = \dfrac{R_b C_c + L_b\left(g_{d0} + 3u_s^d K_{Pv}/2u_{d0}\right)}{2\sqrt{L_b C_c\left(1 + 3u_s^d K_{Pv}\left(R_b + \sigma_i/C_c\right)/2u_{d0}\right)}} \end{cases} \tag{5-22}$$

It is indicated by (5-22) that the dominant oscillation frequency and the damping ratio of the DC link are associated with the control parameters. Due to the small value of $g_{d0}$, the damping ratio $\zeta$ is positive with common parameters. It reveals that the CDVC is conducive

to the DC-side stability, and the CDVC-based VSC with a common proportional gain maintains stability no matter serves as a rectifier or an inverter.

### 5.3.3 Droop-Based VSC

As discussed previously, the DC-side equivalent circuit of the VSC under the droop control is similar to that of the CDVC-based one. Consequently, the equivalent circuit of a CDVC-based VSC to an ideal DC source system is the same as Fig. 5-4. Similar to the analysis of the damping properties of the CDVC-based VSC, the characteristic function of the single droop-based VSC to an ideal DC source system is also expressed by (5-15) and (5-16). Based on DFA, the coefficients of the characteristic function can be written as (5-18). Substitution of (2-46) into (5-18), it provides that,

$$\begin{cases} a_1 = \dfrac{R_b}{L_b} + \dfrac{g_{d0}}{C_c} + \dfrac{3u_s^d K_{Po} K_d \left( \left( 3u_s^d K_{Po} + 2u_{d0} \right) L_b - 2u_{d0} \sigma_i R_b \right)}{\left( 3u_s^d K_{Po} + 2u_{d0} \right)^2 L_b C_c + 4u_d^2 \sigma_i^2} \\ a_0 = \dfrac{R_b g_{d0} + 1}{L_b C_c} + \dfrac{3u_s^d K_{Po} K_d \left( \left( 3u_s^d K_{Po} + 2u_{d0} \right) R_b + 2u_{d0} \sigma_i / C_c \right)}{\left( 3u_s^d K_{Po} + 2u_{d0} \right)^2 L_b C_c + 4u_{d0}^2 \sigma_i^2} \end{cases} \tag{5-23}$$

Notice that with the small value of $\sigma_i$ and $g_{d0}$, the coefficients of the characteristic function can be reduced as,

$$\begin{cases} a_1 \approx \dfrac{R_b}{L_b} + \dfrac{g_{d0}}{C_c} + \dfrac{3u_s^d K_{Po} K_d}{2u_{d0} C_c} \\ a_0 \approx \dfrac{1}{L_b C_c} \left( 1 + \dfrac{3u_s^d K_{Po} K_d}{3u_s^d K_{Po} + 2u_{d0}} \left( R_b + \dfrac{2u_{d0} \sigma_i}{\left( 3u_s^d K_{Po} + 2u_{d0} \right) C_c} \right) \right) \end{cases} \tag{5-24}$$

(5-24) indicates that $a_0$ is positive. On the contrary, $a_1$ could be negative when the droop-based VSC with a relatively small droop coefficient serves as an inverter. Consequently, there is also a critical transfer power for the droop-based inverter, which can be derived as follows.

$$a_1 > 0 \Rightarrow g_{d0} = \frac{P_{dc}}{u_{d0}^2} > -\left( \frac{R_b C_c}{L_b} + \frac{3u_s^d K_{Po} K_d}{2u_{d0}} \right) \Rightarrow P_{dc} > -\left( \frac{R_b C_c u_{d0}^2}{L_b} + \frac{3u_s^d u_{d0} K_{Po} K_d}{2} \right) = -P_{dc}^{cr} \tag{5-25}$$

Compared with (5-10) and (5-25), it is found that the critical transfer power of the VSC is not only related to the DC-link voltage, the transmission resistance and inductance, and the grounded capacitance, but also relevant to the droop coefficient. The critical transfer power enlarges with the increase in the droop coefficient, thereby enhancing the DC-side stability.

Based on (5-24), the dominant frequency and the damping ratio of the DC link can be expressed as,

$$\begin{cases} \omega_d = \dfrac{1}{\sqrt{L_b C_c}} \sqrt{1+\dfrac{3u_s^d K_{Po} K_d}{3u_s^d K_{Po}+2u_{d0}} \left( R_b + \dfrac{2u_{d0}\sigma_i}{\left(3u_s^d K_{Po}+2u_{d0}\right) C_c} \right)} \\ \zeta = \dfrac{\left(3u_s^d K_{Po}+2u_{d0}\right)\left(2u_{d0} R_b C_c + 2u_{d0} L_b g_{d0} + 3u_s^d K_{Po} K_d L_b\right)}{4u_{d0}\sqrt{\left(3u_s^d K_{Po}+2u_{d0}\right)^2 L_b C_c + 3u_s^d K_{Po} K_d L_b \left(\left(3u_s^d K_{Po}+2u_{d0}\right) R_b C_c + 2u_{d0}\sigma_i\right)}} \end{cases} \tag{5-26}$$

By configuring $K_d$ as 0, (5-26) reduces into (5-8), indicating a droop-based VSC with a small droop coefficient has similar damping properties as the CPC-based VSC. In contrast, when $K_d$ is sufficiently large, taking $K_d \longrightarrow \infty$, $K_{Po} = K_{pv}/K_d$ into (5-26), (5-26) reduces into (5-22), manifesting that a droop-based VS`C with a large droop gain has similar damping properties as the CDVC-based VSC.

## 5.4 DC-Side Small-Signal Stability Analysis of the Two-Terminal VSC-Based DC Link

The above part discussed the DC-side damping properties of a single converter. Next, a two-terminal VSC-based DC link depicted in Fig. 5-5 is investigated to develop insight into the interaction of different converters and their influences on the DC-side stability. The classic master-slave control is adopted, i.e., $VSC_1$ utilises the CPC while $VSC_2$ utilises the CDVC. Based on the derived models of the CPC- and CDVC-based VSCs, the equivalent circuit of the DC link under study is depicted in Fig. 5-6. The subscripts $p$ and $v$ denote the electrical quantities at the CPC- and the CDVC-based VSC sides, respectively.

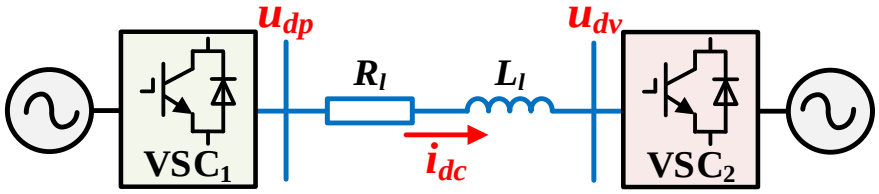


Fig. 5-5 Schematic of two-terminal VSC-based DC link.

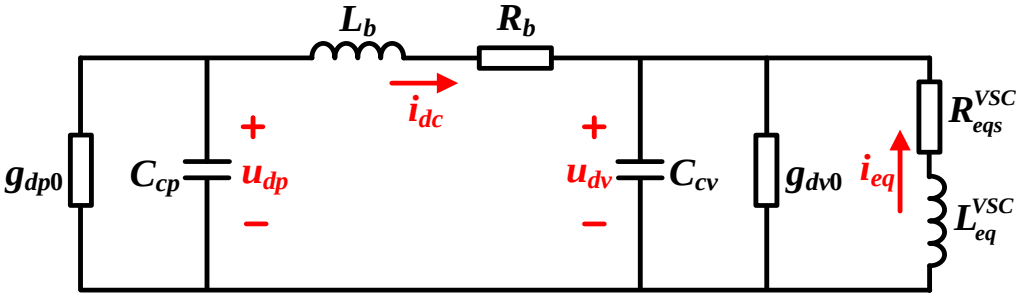


Fig. 5-6 Equivalent circuit of two-terminal VSC-based DC link.

As per the equivalent circuit shown in Fig. 5-6, the studied system are written as follows.

$$\begin{cases} C_{cp}\dfrac{\mathrm{d}u_{dp}}{\mathrm{d}t} = -g_{dp0}u_{dp} - i_{dc} \\ L_b\dfrac{\mathrm{d}i_{dc}}{\mathrm{d}t} = u_{dp} - u_{dv} - R_b i_{dc} \\ C_{cv}\dfrac{\mathrm{d}u_{dv}}{\mathrm{d}t} = i_{dc} - g_{dv0}u_{dv} + i_{eq} \\ L_{eq}^{VSC}\dfrac{\mathrm{d}i_{eq}}{\mathrm{d}t} = -u_{dv} - R_{eqs}^{VSC}i_{eq} \end{cases} \tag{5-27}$$

(5-27) indicates that the two-terminal DC system under study is a four-order dynamic system. It is difficult to deduce an analytical stability criterion for such a high-order system. To address this issue, DFA is utilised for the stability analysis as follows.

### 5.4.1 Dominant Oscillation Mode of the Two-Terminal VSC-Based DC Link

The first step of DFA is to determine the dominant oscillation mode in the system under study. On the basis of the analysis of the damping properties of VSCs, the CPC-based VSC induces negative damping to the DC link when serving as an inverter, while the CDVC-based VSC always provides positive damping to the system when the proportional gain of the CDVC is not too small. Therefore, the dominant oscillation mode in the two-terminal DC link is induced by that the negative damping of the CPC-based VSC stimulates the resonance of the DC network. The natural oscillation mode of the two-terminal DC link is the same as that of the single CPC-based VSC to an ideal DC source system, which is written as,

$$\frac{\mathrm{d}}{\mathrm{d}t}\begin{bmatrix}\Delta u_{dp}\\ \Delta i_{dc}\end{bmatrix} = \begin{bmatrix} -\dfrac{g_{dp0}}{C_{cp}} & -\dfrac{1}{C_{cp}} \\ \dfrac{1}{L_b} & -\dfrac{R_b}{L_b}\end{bmatrix}\begin{bmatrix}\Delta u_{dp}\\ \Delta i_{dc}\end{bmatrix} \tag{5-28}$$

Based on (5-28), the natural oscillation frequency is obtained as,

$$\omega_n = \frac{R_b g_{dp0} + 1}{\sqrt{L_b C_c}} \approx \frac{1}{\sqrt{L_b C_c}} \tag{5-29}$$

(5-29) indicates that the DC transmission inductance and the equivalent DC-link capacitance of the CPC-based VSC constitute a second-order oscillator. Accordingly, the natural frequency of the DC link is only associated with the transmission inductance and the capacitance of the CPC-based VSC.

### 5.4.2 Impacts of the CDVC-Based VSC on the DC Link

Calculating the inverse Laplace transform of the third and fourth equations in (5-27), it yields that,

$$\begin{cases} \Delta i_{eq} = -\dfrac{1}{sL_{eq}^{VSC} + R_{eq}^{VSC}} \Delta u_{dv} = -G_{eq}(s)\Delta u_{dv} \\ \Delta i_{dc} = \dfrac{1}{sC_{cv} + g_{dv0} + G_{eq}(s)} \Delta u_{dv} = G_z(s)\Delta u_{dv} \end{cases} \tag{5-30}$$

Substitution of (5-30) into the first and second equations in (5-27) yields,

$$\frac{\mathrm{d}}{\mathrm{d}t}\begin{bmatrix} \Delta u_{dp} \\ \Delta i_{dc} \end{bmatrix} = \begin{bmatrix} -\dfrac{g_{dp0}}{C_{cp}} & -\dfrac{1}{C_{cp}} \\ \dfrac{1}{L_b} & -\dfrac{R_b + G_z(s)}{L_b} \end{bmatrix} \begin{bmatrix} \Delta u_{dp} \\ \Delta i_{dc} \end{bmatrix} \tag{5-31}$$

Based on (5-31), the characteristic function of the system under study is derived as,

$$F(s) = \begin{vmatrix} s + \dfrac{g_{dp0}}{C_{cp}} & \dfrac{1}{C_{cp}} \\ -\dfrac{1}{L_b} & s + \dfrac{R_b + G_z(s)}{L_b} \end{vmatrix} = s^2 + \left( \frac{R_b}{L_b} + \frac{g_{dp0}}{C_{cp}} + \frac{G_z(s)}{L_b} \right) s + \frac{\left(R_b + G_z(s)\right) g_{dp0} + 1}{L_b C_{cp}} \tag{5-32}$$

### 5.4.3 Model Reduction of the Two-Terminal DC Link Based on Dominant Frequency Analysis

Based on DFA, the characteristic function expressed by (5-32) can be simplified in the vicinity of the dominant frequency as follows.

$$F(s) = s^2 + a_1 s + a_0 s \tag{5-33}$$

where,

$$\begin{cases} a_1 = \dfrac{R_b}{L_b} + \dfrac{g_{dp0}}{C_{cp}} + \dfrac{\mathrm{Re}\left(G_z(j\omega_n)\right)}{L_b} + \dfrac{g_{dp0}\,\mathrm{Im}\left(G_z(j\omega_n)\right)}{L_b C_{cp}\omega_n} \\ a_0 = \dfrac{R_b g_{dp0} + 1}{L_b C_{cp}} + \dfrac{g_{d0}\,\mathrm{Re}\left(G_z(j\omega_n)\right)}{L_b C_{cp}} - \dfrac{\omega_n\,\mathrm{Im}\left(G_z(j\omega_n)\right)}{L_b} \end{cases} \tag{5-34}$$

Based on (2-44), (5-29), and (5-30), $G_z(j\omega_n)$ is simplified as follows nearby the dominant frequency.

$$
\begin{aligned}
G_z\left(j\omega_n\right) &= \frac{1}{j\omega_n C_{cv} + g_{dv0} + 1\Big/\left(j\omega_n L_{eq}^{VSC} + R_{eqs}^{VSC}\right)} \\
&= \frac{\dfrac{2u_{dv0}}{3u_s^d K_{Pv}}\left(1 + j\dfrac{\sigma_i}{\sqrt{L_b C_{cp}}}\right)}{1 + \dfrac{2u_{dv0}g_{dv0}}{3u_s^d K_{Pv}} - \dfrac{2u_{dv0}\sigma_i C_{cv}}{3u_s^d K_{Pv} L_b C_{cp}} + j\dfrac{1}{\sqrt{L_b C_{cp}}}\left(\dfrac{2u_{dv0}\sigma_i}{3u_s^d K_{Pv}} + C_{cv}\right)} \\
&\approx \frac{2u_{dv0}}{3u_s^d K_{Pv}} + j\frac{2u_{dv0}\sigma_i}{3u_s^d K_{Pv}\sqrt{L_b C_{cp}}}
\end{aligned}
\tag{5-35}
$$

Substitution of (5-35) into (5-34), the coefficients of the characteristic function can be reduced as,

$$
\begin{cases}
a_1 = \dfrac{R_b}{L_b} + \dfrac{g_{dp0}}{C_{cp}} + \dfrac{2u_{dv0}}{3u_s^d K_{Pv} L_b} + \dfrac{2u_{dv0}\sigma_i g_{dp0}}{3u_s^d K_{Pv} L_b C_{cp}} \approx \dfrac{R_b}{L_b} + \dfrac{g_{dp0}}{C_{cp}} + \dfrac{2u_{dv0}}{3u_s^d K_{Pv} L_b} \\
a_0 = \dfrac{1}{L_b C_{cp}}\left(1 + R_b g_{dp0} + \dfrac{2u_{dv0}g_{dp0}}{3u_s^d K_{Pv}} - \dfrac{2u_{dv0}\sigma_i}{3u_s^d K_{Pv} L_b}\right) \approx \dfrac{1}{L_b C_{cp}}
\end{cases}
\tag{5-36}
$$

Note that the approximations in (5-35) and (5-36) hold due to the small values of $g_{d0}$, $\sigma_i$, and $C_c$. Based on (5-36), the dominant oscillation frequency and the damping ratio of the DC link are written as,

$$
\begin{cases}
\omega_d = \dfrac{1}{\sqrt{L_b C_{cp}}} \\
\zeta = \dfrac{a_1}{2\omega_n} = \dfrac{1}{2\sqrt{L_b C_{cp}}}\left(\dfrac{R_b}{L_b} + \dfrac{g_{dp0}}{C_{cp}} + \dfrac{2u_{dv0}}{3u_s^d K_{Pv} L_b}\right)
\end{cases}
\tag{5-37}
$$

(5-37) indicates that the CPC- and CDVC-based VSCs jointly determine the damping ratio of the DC link.

### 5.4.4 Analytical DC-Side Stabilising Condition of the Two-Terminal DC Link

The two-terminal DC link is stable, provided that the dominant mode has a positive damping ratio. According to (5-37), a concise stabilising requirement of the two-terminal VSC-based DC system can be expressed as,

$$
a_1 > 0 \quad \Rightarrow \quad \frac{R_b}{L_b} + \frac{P_{dc}}{u_{dp0}^2 C_{cp}} + \frac{2u_{dv0}}{3u_s^d K_{Pv} L_b} > 0 \tag{5-38}
$$

(5-38) indicates that the damping of the studied system broadly comes from three aspects. The first term denotes the positive damping arising from the transmission resistance in the DC

link. The second term denotes the impacts of the CPC-based VSC, and this term is negative once the VSC serves as an inverter. The third term denotes the positive damping generated from the CDVC-based VSC. It is interesting to find that if the positive damping induced by the CDVC-based VSC and the transmission resistance cannot offset the negative damping brought by the CPC-based inverter, DC-side instability will occur in the DC link.

Substitution of $g_{dp0} = P_{dc} / u_{dp0}^2$ into (5-38) provides,

$$P_{dc} > -\frac{u_{dp0}^2 C_{cp}}{L_b}\left(R_b + \frac{2u_{dv0}}{3u_s^d K_{Pv}}\right) = -P_{dc}^{cr} \approx -\frac{u_n^2 C_{cp}}{L_b}\left(R_b + \frac{2u_n}{3u_s^d K_{Pv}}\right) \tag{5-39}$$

In (5-39), $u_{dp0}$ and $u_{dv0}$ are replaced with $u_n$ since the DC-link voltage is very close to the nominal value during normal operation. (5-39) implies that DC-side instability could occur if the power transferred in the DC link is larger than a critical value.

The stability margin can be defined as the relative distance from the actual transfered power to the critical one, which is expressed as,

$$M_s = \frac{\left(-P_{dc}^{cr}\right) - P_{dc}}{\left(-P_{dc}^{cr}\right)} = 1 + \frac{P_{dc}}{P_{dc}^{cr}} \tag{5-40}$$

Based on (5-40), the stability margin decreases as the transferred power $P_{dc}$ decreases. Therefore, the system has the minimum stability margin if $P_{dc} = -P_{dc}^{cap}$.

For reliability, the stability margin must be higher than a positive value under every operating point. The allowable minimum stability margin is denoted by $M_s^{\min}$ in this thesis. Synthesizing (5-39) and (5-40), the maximum value of $K_{Pv}$ for ensuring the stability margin reserve can be obtained as,

$$\min\left\{M_s\right\} = 1 + \frac{-P_{dc}^{cap}}{P_{dc}^{cr}} > M_s^{\min} \quad \Rightarrow \quad K_{Pv} < \frac{2u_n^3 C_{cp}\left(1 - M_s^{\min}\right)}{3u_s^d\left(P_{dc}^{cap} L_b - u_n^2 R_b C_{cp}\left(1 - M_s^{\min}\right)\right)} = K_{Pv}^{\max} \tag{5-41}$$

By setting $K_{Pv}$ no more than $K_{Pv}^{\max}$, the DC link keeps stable under DC-side disturbances even under the severest operating point.

## 5.5 Case Studies

### 5.5.1 A Single Converter to an Ideal DC Source System

A single VSC connected to an ideal DC source system illustrated by Fig. 5-1 is built in PSCAD/EMTDC to verify the analysis of the damping properties of VSCs. The nominal DC-link voltage of the test system is ±200 kV. The TLVSC adopts the CPC or the droop control,

and the time constant of its inner loop is 3 ms. DC supplementary reactors of 50 mH are deployed at the terminals of a 200 km DC transmission line. Other parameters of the test system are summarized in Table 5-1.

Table 5-1 Main parameters of the test single VSC to an ideal DC source system

| Symbol | Item | Value |
|---|---|---|
| $u_n$ | Nominal DC-link voltage of the test system | ±200 kV |
| $u_s$ | Nominal voltage of VSC-tied AC source | 220 kV |
| $\omega_s$ | Nominal frequency of AC grids | 50 Hz |
| $C_c$ | DC-link capacitance of VSC | 220 μF |
| $\sigma_i$ | Time constant of the inner loop | 3 ms |
| ($K_{Po}$, $K_{Io}$) | Proportional and integral gains of the CPC | (1, 10) |
| $K_d$ | Droop coefficient | 0.2 |
| $L_T$ | Inductance of DC reactors | 50 mH |
| $R_0$ | Per-kilometre resistance of DC line | 0.015 Ω |
| $L_0$ | Per-kilometre inductance of DC line | 1.635 mH |
| $l$ | Length of the DC line | 200 km |

Fig. 5-7 shows the dynamic properties of the single VSC to an ideal DC source system under power alternations. Fig. 5-7 (a) and (b) are dynamic responses of the DC-link current and the transmitted active power when the reference power of the CPC-based VSC suddenly changes, respectively. The negative sign denotes the CPC-based VSC serves as an inverter. As can be seen, the damping ratio gradually decreases with the increase in the transfer power. When the reference power changes from -50 MW to -300 MW, the damping ratio of the DC link becomes negative. Accordingly, apparent divergent oscillations appear in the DC-link current and the transfer power. This validates the CPC-based inverter will induce negative damping to the DC link. Fig. 5-7 (c) depicts the dynamics of the test system under a relatively slow increase in the reference power of the CPC-based VSC. Based on (5-10), the critical transfer power of the DC link is calculated as 247 MW. When the transfer power exceeds this value, divergent oscillations appear in the DC link, which gradually develops into unattenuated oscillations because of the saturation of the inner current control of the VSC. Fig. 5-7 (d) depicts the change in the damping ratio and oscillation frequency with the transfer power. It is observed that when the CPC-based VSC serves as a rectifier, the increase in the transfer power is conducive to its damping properties. On the contrary, when the CPC-based VSC serves as an inverter, the increase in the transfer power degrades the damping ratio and even causes DC-

side instability. As for the oscillation frequency, different operating points have negligible impacts on the frequency. This can be explained by (5-8) that the oscillation arises from the resonant oscillator composed by the transmission inductance and the grounded capacitance. Fig. 5-7 (e) shows the root locus of the dominant oscillation mode of the test system when the VSC adopts the droop control. It is shown that the root locus moves right with the increase in the droop coefficient. The critical transfer power increases to 399 MW with $K_d = 0.4$, which is in line with (5-25). It is indicated that the DC-side stability enhances with the increase in the droop coefficient.

Fig. 5-8 depicts the dynamic responses of the test system under sudden power alternations with different physical and control parameters. As illustrated by Fig. 5-8 (a), the damping ratio drops as the DC-link capacitance of the CPC-based VSC decreases, and DC-side instability appears with the converter capacitance decreases to 150 μF. In addition, it can be seen that the decrease of the DC-link capacitance leads to an increase in the oscillation frequency in the DC link. Fig. 5-8 (b) shows the influences of the line length on the system dynamics. The damping ratio decreases with a shorter transmission distance. This is because the shorter the line is, the less the ratio between the transmission resistance and the inductance will be due to the existence of the DC supplementary reactors. As a result, the critical transfer power of the DC link drops based on (5-10) so that the DC-side stability gets endangered. Fig. 5-8 (c) shows the system dynamics with different DC reactor inductances. As the DC reactor inductance increases, the damping ratio of the DC link significantly reduces. Simultaneously, the oscillation frequency also decreases. Fig. 5-8 (d) shows the system dynamic responses with different droop coefficients. As the droop coefficient decreases, the damping ratio of the DC link decreases, and there exhibit divergent oscillations in the transfer power with $K_d = -0.2$. This can be explained by (5-25) that the increase in the droop coefficient will enlarge the critical transfer power, thereby reducing the risks of DC-side stability. Simulation studies validate the correctness of the analysis of the damping properties of converters.

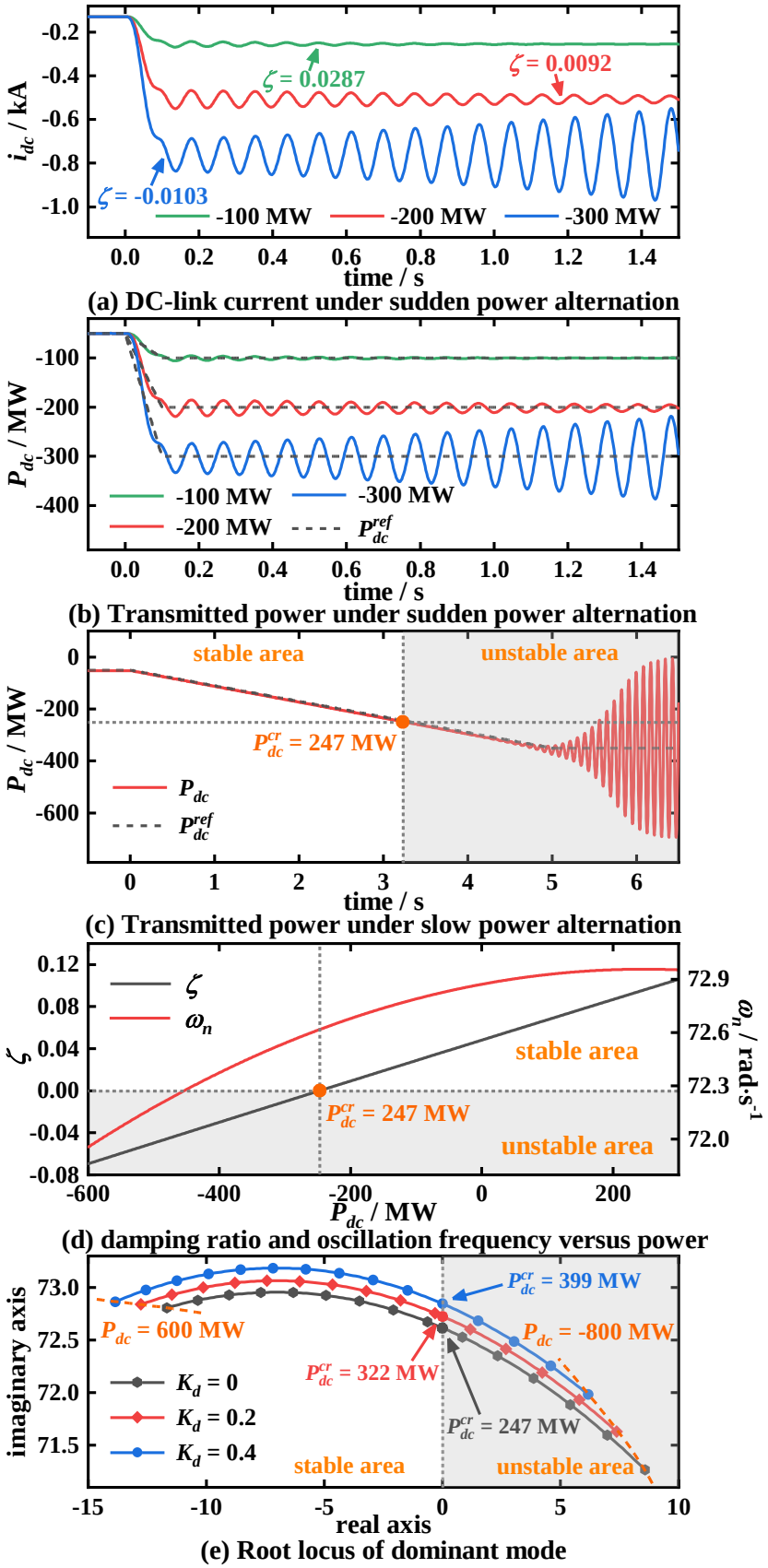


Fig. 5-7 Dynamic properties of the single VSC to an ideal DC source system under power alternations.

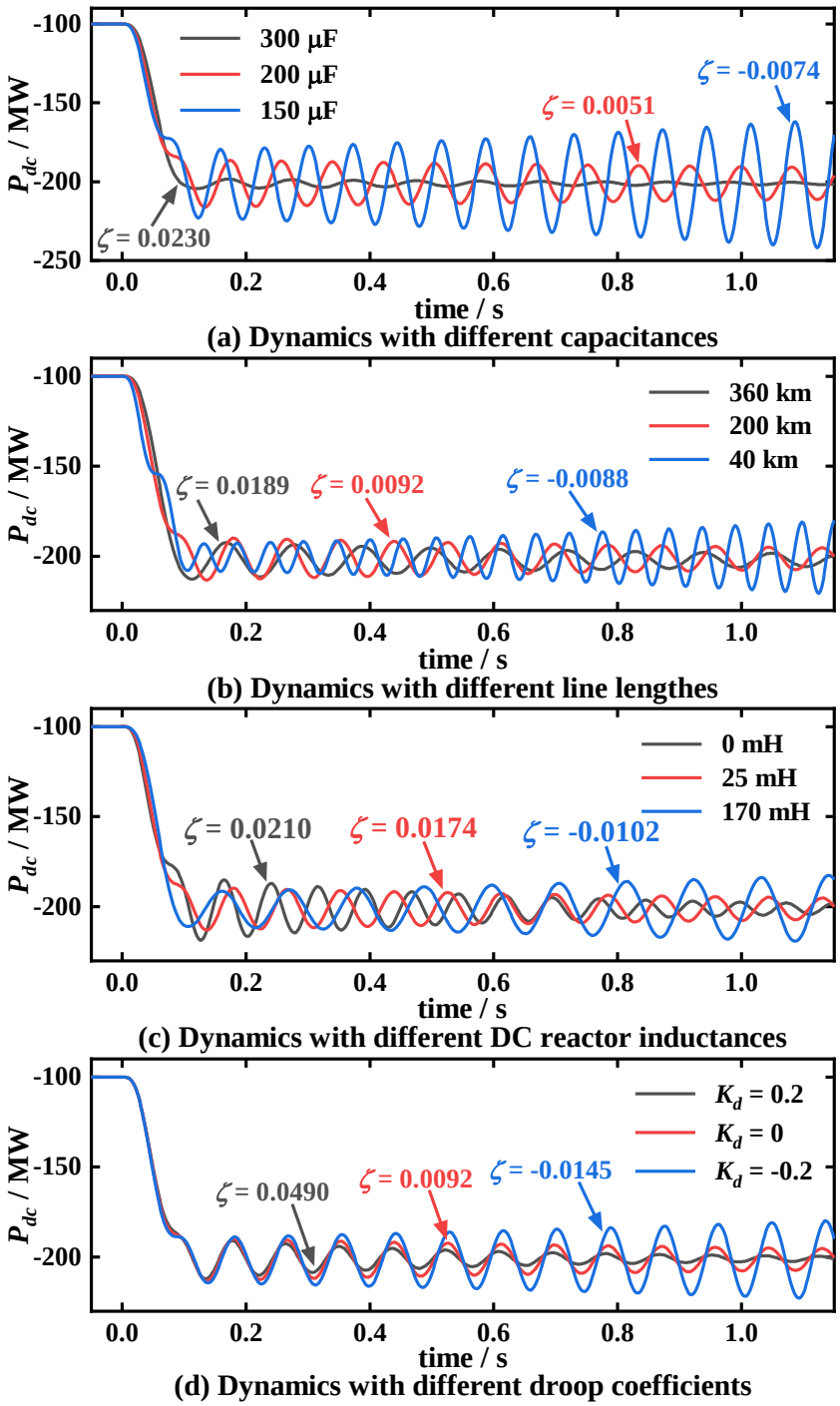


Fig. 5-8 Impacts of system parameters on the dynamics of the single VSC to an ideal DC source system.

### 5.5.2 Two-Terminal VSC-HVDC System

A two-terminal MMC-based DC transmission system illustrated by Fig. 5-5 is built in PSCAD/EMTDC to validate the stabilising condition of the two-terminal DC link. The nominal DC-link voltage and the base capacity of the test system are ±200 kV and 400 MW, respectively. The length of the DC line is 100 km, which is represented by the frequency-dependent (phase) model. The MMCs have 201 levels, which are represented by the detailed

switching model. The time constant of the inner loop is 2 ms for fast-tracking. The proportional and integral gains of the CPC-based $MMC_1$ are 1 and 10, respectively. The proportional and integral gains of the CDVC-based $MMC_2$ are 3 and 50, respectively. The main parameters of the test HVDC system are provided in Table 5-2.

Table 5-2 Main parameters of the test two-terminal VSC-HVDC system

| Symbol | Item | Value |
|---|---|---|
| $u_n$ | Nominal DC-link voltage of the test system | ±200 kV |
| $u_s$ | Nominal voltage of VSC-tied AC source | 220 kV |
| $P_{dc}^{cap}$ | Transmission capacity of the DC link | 400 MW |
| $N_{sm}$ | Number of SMs of MMC in one arm | 200 |
| $C_{sm}$ | SM capacitance | 6000 μF |
| $R_{on}$ | On-state resistance of a diode or IGBT | 5.44 mΩ |
| $L_a$ | Bridge arm inductance | 29 mH |
| $\sigma_i$ | Time constant of the inner loop | 2 ms |
| ($K_{Po}$, $K_{Io}$) | Proportional and integral gains of the CPC | (1, 10) |
| ($K_{Pv}$, $K_{Iv}$) | Proportional and integral gains of the CDVC | (3, 15) |
| $R_0$ | Per-kilometre resistance of DC line | 0.015 Ω |
| $L_0$ | Per-kilometre inductance of DC line | 1.7 mH |
| $l$ | Length of the DC line | 100 km |

Fig. 5-9 compares the dynamics properties of the point-to-point VSC-HVDC link with different models, namely, the EMTP simulation model, the analytical model expressed by (5-27), and the reduced model based on DFA. Fig. 5-9 (a) and (b) show the system dynamics under the power alternation from 100 MW to 300 MW and -400 MW, respectively. With all three models, the DC-link current vibrates roughly at the dominated frequency after the perturbance, which is 125.39 rad/s based on (5-36). Although some very slight high-frequency fluctuations may exist with the EMTP simulation model because of the switching process of MMCs, they are neglectable on the whole, and the dynamics under the three models are quite approximate to each other. Besides, it is verified that the DC system could exhibit divergent oscillations once the transferred power from the CDVC-based VSC to the CPC-based VSC exceeds the critical transfer power.

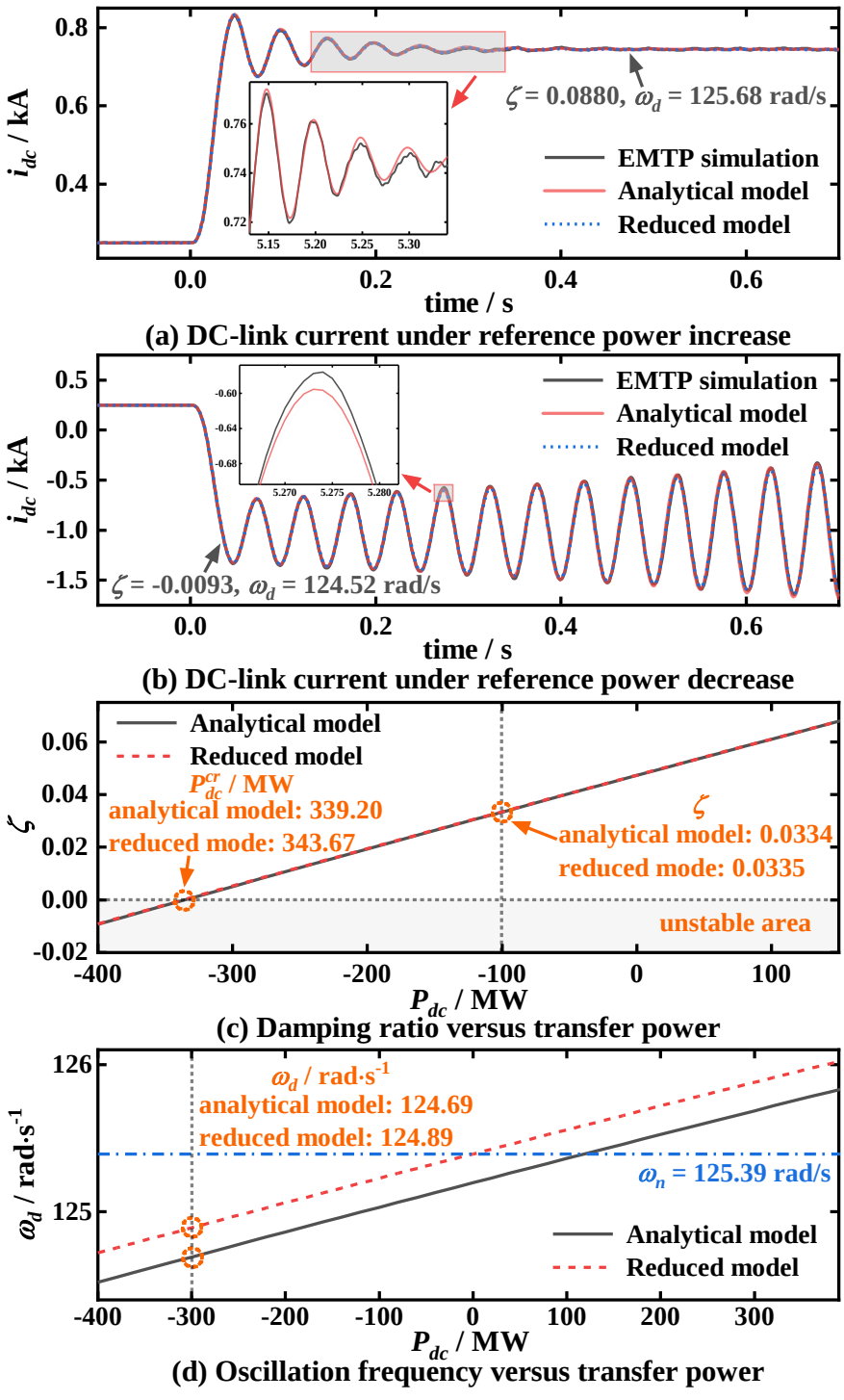


Fig. 5-9 Dynamic properties of the two-terminal VSC-HVDC system with different models.

Fig. 5-9 (c) and (d) further depict the change in the damping ratio and the dominant oscillation frequency versus the transfer power. It is observed that the calculation results by the analytical and reduced models are almost the same. With the analytical model, the critical transfer power is 339.20 MW, which is determined by finding the minimal transfer power making the damping ratio of the dominant mode negative. As for the reduced model, the

critical transfer power is calculated as 343.67 MW based on (5-39). Under any transfer power, the damping ratio of the reduced model is quite near to that of the analytical model obtained via eigenvalue calculation, manifesting the accuracy of DFA for stability analysis. Moreover, the oscillation frequency remains rather close to the natural oscillation frequency marked as the blue dot-dash line no matter the transfer power, indicating the variation of the operating point mainly impacts the system damping but not the oscillatory frequency. The numerical results manifest the accuracy of the proposed analytical and reduced models for DC-side stability analysis.

Fig. 5-10 shows the influences of physical system parameters on the DC-side stability. Fig. 5-10 (a) indicates that the critical transfer power dramatically drops with the increase in the transmission inductance. When the transmission inductance is 0.2 H, the critical transfer power is around 600 MW. When the transmission inductance increases to 1.0 H, the critical transfer power reduces to around 120 MW. In addition, it is shown that the critical transfer power with the analytical model is closely approximated to that with the reduced model in a wide range of the transmission inductance, which verifies the accuracy of the proposed DFA for small-signal stability analysis. Fig. 10 (b) depicts the DC-link current dynamics under a sudden power variation from -100 MW to -300 MW with different transmission inductances. The damping ratio decreases with the increase in the transmission inductance. When the transmission inductance exceeds 0.4 H, the damping ratio becomes negative and divergent oscillations appear in the DC-link current. Additionally, it is observed that the oscillation frequency reduces with the increase in the transmission inductance. Fig. 5-10 (c) presents the impacts of the converter capacitance on the dynamics. The critical transfer power rises rapidly as the converter capacitance increases. Besides, the critical transfer power with the analytical and the reduced models are quite close, indicating making approximations in the neighbourhood of the dominant frequency brings very limited error to the stability properties. Fig. 5-10 (d) depicts the DC-link current dynamics with different converter capacitances under a sudden power variation from -100 MW to -300 MW. The transient simulation results indicate that the system damping gradually decreases as the converter capacitance decreases. Particularly, the system damping will be negative once the transferred power is larger than the critical transferred power, leading to divergent oscillations depicted in Fig. 5-10 (d). Meanwhile, it is also manifested that the increase in the converter capacitance can result in a reduction in the oscillatory frequency.

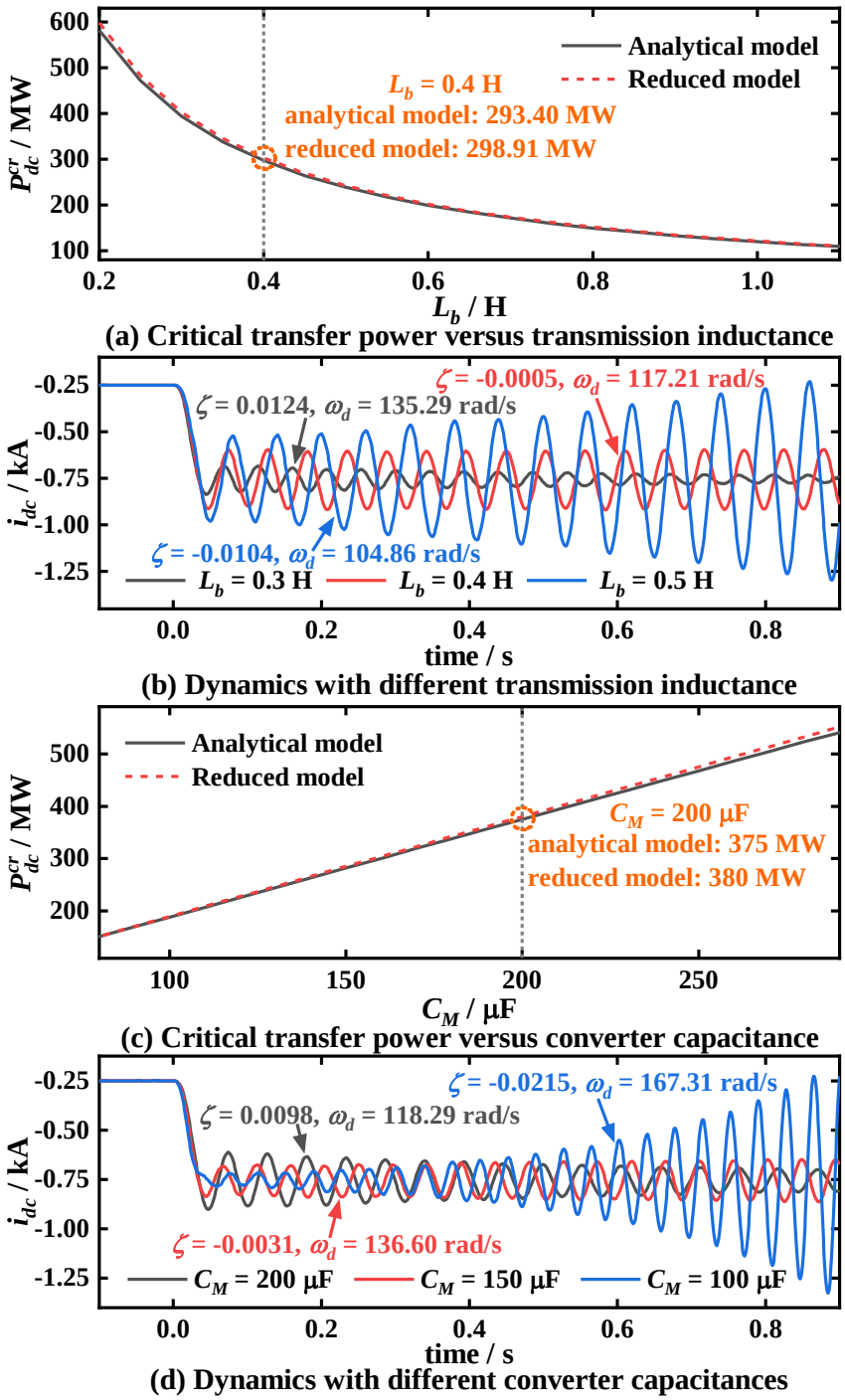


Fig. 5-10 Impacts of the physical system parameters on the DC-side stability.

Fig. 5-11 shows the impacts of the proportional gain of CDVC on the DC-side stability. Fig. 5-11 (a) presents that the critical transfer power dramatically descends as the proportional gain of CDVC increases when it is small. In contrast, there exists a clear saturation trend when further increasing the proportional gain, and the critical transfer power converges to a constant value. This is because the effect of the CDVC-based converter on the system stability is inversely proportional to the proportional gain as expressed by (5-38) so that the dynamic

properties of the two-terminal DC link with a sufficiently large proportional gain become approximate to those of a single CPC-based VSC to an ideal DC source system. Fig. 5-11 (b) shows the change in stability margin with different proportional gains when the transfer power reaches the capacity of the DC link. It is manifest that the system stability margin can be significantly improved by reducing the proportional gain since, in this way, the CDVC-based converter can provide larger system damping based on (5-37). Provided that the allowable minimal stability margin is 0.1, the maximum proportional gain of CDVC to ensure DC-side stability is 0.8004 and 0.8207 with the analytical and reduced models, respectively. Fig. 5-11 (c) shows the dynamic of the studied system under the power alternation from -100 MW to -400 MW. It is observed that divergent oscillations will occur when the proportional gain exceeds 2, which corresponds to the region of the negative stability margin shown in Fig. 5-11 (b). However, by setting the proportional gain to no more than the maximum value expressed by (5-41), the DC-side oscillation can be effectively damped.

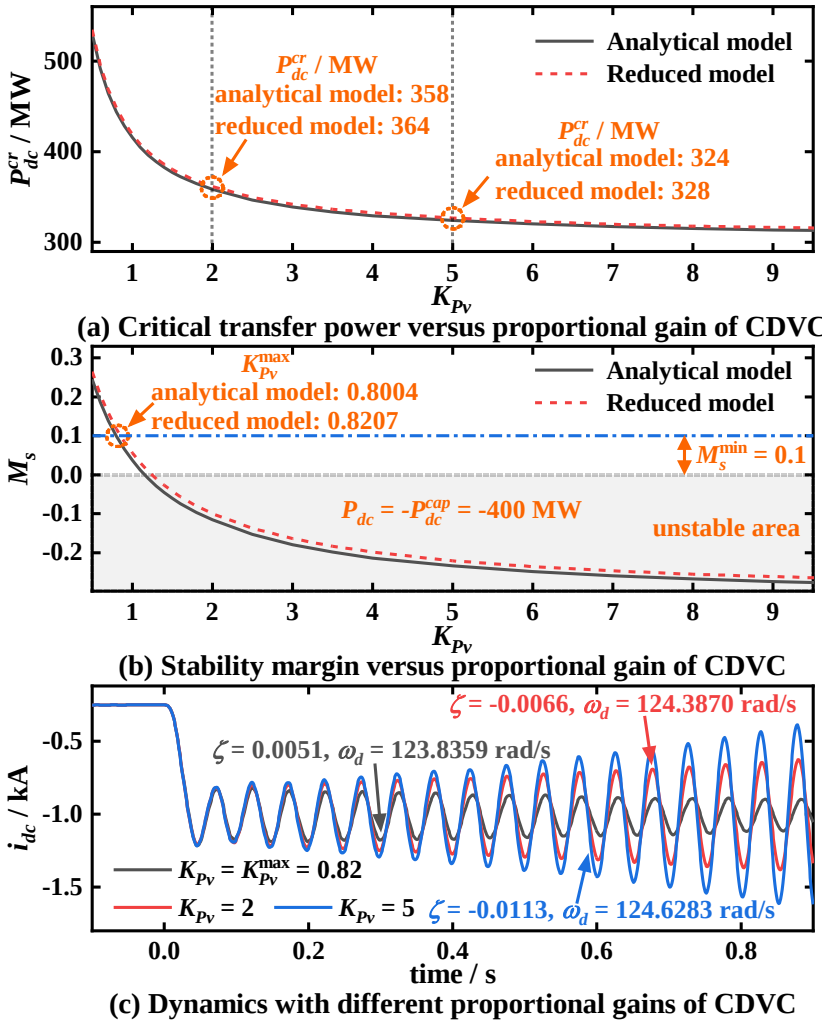


Fig. 5-11 Impacts of CDVC parameters on system stability.

## 5.6 Summary

This chapter develops insight into the oscillations originating from the resonances between the DC-link transmission inductors and the DC-link grounded capacitors. The damping properties of different converters are first investigated. The LCC always provides positive damping to the DC link, and its damping can be enlarged by increasing the proportional gain or reducing the integral gain of the constant current controller. As for the VSC, its damping properties are closely associated with the control mode. The CPC-based VSC provides positive damping when it serves as a rectifier and vice versa. More importantly, the damping is related to the operating point (i.e., the transfer power) but is irrespective of the control parameters. By using DFA to reduce the order of the characteristic function, it is found that the CDVC-based VSC can always generate positive damping to the DC link, provided that the proportional gain of CDVC is not too small. Similarly, the damping of the droop-based VSC is relevant to the droop gain, and the increase in the droop gain will significantly improve the damping properties. Furthermore, the stabilising condition of the two-terminal DC link is derived to figure out how different converters jointly influence the DC-side stability. Based on DFA, it is revealed that when the negative damping induced by the CPC-based inverter cannot be compensated by the positive damping provided by the CDVC-based rectifier and the DC transmission line, divergent oscillations will appear in the DC link. Finally, simulation studies have verified the analysis of converter damping properties and the derived stabilising condition of the two-terminal DC link.

# 6 DC-Side Stability Analysis of Generic MTDC Systems Based on Dominant Frequency Analysis

## 6.1 Introduction

The DC-side damping properties of various converters are studied in the last chapter. As the number of converters increases, the small-signal stability analysis of an MTDC system becomes more difficult. On the one hand, the order of the studied system could be rather high, which significantly increases the computational burden. On the other hand, there might exist various oscillation frequencies in the DC network, and the interactions between converters and the DC network becomes more complicated.

So far, the small-signal stability of MTDC systems has been investigated based on modal analysis and the impedance-based method. The state-space model of the combined AC-MTDC system is formulated in [77]. Based on the participation factor analysis, it is revealed that some oscillation modes in the combined AC-MTDC system are merely relevant to the DC-side state variables. Actually, the stability issue arising from these variables is called the DC-side stability in this thesis. The interaction modes between converters are evaluated in [78] by calculating the aggregated participation factors. It is indicated that the interactions between converters are closely relevant to the DC-link voltage. However, these methods possess high computational complexity due to the high-order modelling. The order of each TLVSC reaches 18 in [78], while the order of the test system in [77] containing 4 TLVSCs and 6 SGs reaches 246. To address this issue, the DC-side impedance of the MMC is derived in [88], and the interactions between the converter and the DC network are accessed by using the impedance-based method. Nevertheless, this method cannot offer an analytical stability boundary of the MTDC system.

Existing works on the stability of MTDC systems fail to provide clear mathematical relationships between system parameters and system stability. In this chapter, the frequency domain model of the MTDC system is first built up. Subsequently, model reduction is conducted nearby each dominant frequency based on DFA to derive the analytical stabilising conditions of MTDC systems. Accordingly, the contribution of each converter on the system damping and the influences of control parameters on the DC-side stability of the entire MTDC system are clearly revealed.

## 6.2 Frequency Domain Model of Converters

The frequency domain model of various converters is formulated based on the derived DC-side equivalent models in Chapter 2. For the convenience of introducing perturbations, the control reference value is no longer assumed to be constant.

Based on (2-3) and (2-6), the small-signal model of the LCC-based rectifier is written as,

$$\Delta i_{dc} = -G_c(s)\Delta u_d + G_u(s)\Delta i_{dc}^{ref} \tag{6-1}$$

where,

$$\begin{cases} G_c(s) = \dfrac{1}{R_{eq}^{LCC} + 1/sC_{eq}^{LCC}} = \dfrac{1}{d_\gamma + V_o \sin\alpha_0 K_{Pc} + V_o \sin\alpha_0 K_{Ic}/s} \\ G_u(s) = \dfrac{R_{eq}^{LCC} - d_\gamma + 1/sC_{eq}^{LCC}}{R_{eq}^{LCC} + 1/sC_{eq}^{LCC}} = \dfrac{V_o \sin\alpha_0 K_{Pc} + V_o \sin\alpha_0 K_{Ic}/s}{d_\gamma + V_o \sin\alpha_0 K_{Pc} + V_o \sin\alpha_0 K_{Ic}/s} \end{cases} \tag{6-2}$$

Similarly, the frequency domain model of the CPC-based VSC is expressed as follows based on (2-25) and (2-35).

$$\Delta i_{dc} = -G_c(s)\Delta u_d + G_u(s)\Delta P_{ac}^{ref} \tag{6-3}$$

where,

$$\begin{cases} G_c(s) = sC_c + i_{d0}/u_{d0} = sC_c + g_{d0} \\ G_u(s) = \dfrac{3u_s^d\left(K_{Po} + K_{Io}/s\right)}{2u_{d0}\left(\sigma_i s + 1 + 3u_s^d\left(K_{Po} + K_{Io}/s\right)/2\right)} \approx \dfrac{1}{u_{d0}} \end{cases} \tag{6-4}$$

In (6-4), $G_u(s)$ is simplified within the range of oscillation frequency in the DC link.

Considering the droop coefficient, the frequency model of the droop-based VSC is expressed as,

$$\Delta i_{dc} = -G_c(s)\Delta u_d + G_u(s)\Delta P_{ac}^{ref} \tag{6-5}$$

where,

$$\begin{cases} G_c(s) = sC_c + g_{d0} + \dfrac{3u_s^d K_d\left(K_{Po} + K_{Io}/s\right)}{2u_{d0}\left(\sigma_i s + 1 + 3u_s^d\left(K_{Po} + K_{Io}/s\right)/2\right)} \approx sC_c + g_{d0} + \dfrac{K_d}{u_{d0}} \\ G_u(s) = \dfrac{3u_s^d\left(K_{Po} + K_{Io}/s\right)}{2u_{d0}\left(\sigma_i s + 1 + 3u_s^d\left(K_{Po} + K_{Io}/s\right)/2\right)} \approx \dfrac{1}{u_{d0}} \end{cases} \tag{6-6}$$

As for the CDVC-based VSC, its frequency domain model is written as,

$$\Delta i_{dc} = -G_c(s)\Delta u_d + G_u(s)\Delta u_{dc}^{ref} \tag{6-7}$$

where,

$$\begin{cases} G_c(s) = sC_c + g_{d0} + \dfrac{3u_s^d\left(K_{Pv} + K_{Iv}/s\right)}{2u_{d0}\left(\sigma_i s + 1\right)} \approx \dfrac{3u_s^d K_{Pv}}{2u_{d0}} \\ G_u(s) = sC_c + g_{d0} + \dfrac{3u_s^d\left(K_{Pv} + K_{Iv}/s\right)}{2u_{d0}\left(\sigma_i s + 1\right)} \approx \dfrac{3u_s^d K_{Pv}}{2u_{d0}} \end{cases} \tag{6-8}$$

## 6.3 DC-Side Stability Analysis of the Three-Terminal VSC-HVDC System

A typical three-terminal VSC-based HVDC system illustrated by Fig. 6-1 is under study. Three TLVSCs are interconnected through DC transmission lines represented by the RL model. $VSC_1$ and $VSC_2$ are the CPC-based rectifier and inverter, respectively. $VSC_3$ adopts the CDVC to regulate the DC-link voltage of the system.

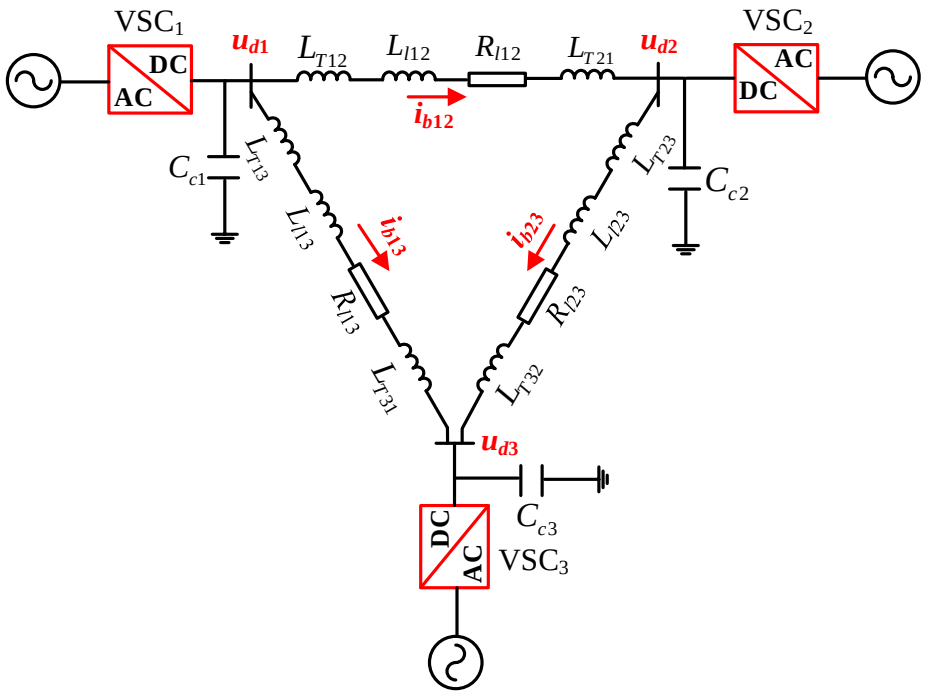


Fig. 6-1 Schematic of the three-terminal VSC-based HVDC system.

### 6.3.1 Frequency Domain Model of the Three-Terminal VSC-HVDC System

According to the converter model and KCL, the following equations hold.

$$\begin{cases} G_{c1}(s)\Delta u_{d1} = -\Delta i_{b12} - \Delta i_{b13} \\ G_{c2}(s)\Delta u_{d2} = -\Delta i_{b12} + \Delta i_{b23} \\ G_{c3}(s)\Delta u_{d3} = \Delta i_{b13} + \Delta i_{b23} \end{cases} \tag{6-9}$$

Based on KVL, it yields that,

$$\begin{cases} Z_{b12}(s)\Delta i_{b12} = (sL_{b12} + R_{b12})\Delta i_{b12} = \Delta u_{d1} - \Delta u_{d2} \\ Z_{b13}(s)\Delta i_{b13} = (sL_{b13} + R_{b13})\Delta i_{b13} = \Delta u_{d1} - \Delta u_{d3} \\ Z_{b23}(s)\Delta i_{b23} = (sL_{b23} + R_{b23})\Delta i_{b23} = \Delta u_{d2} - \Delta u_{d3} \end{cases} \tag{6-10}$$

Combined with (6-9) and (6-10), the frequency domain model of the studied system is deduced as,

$$\begin{cases} \left(G_{c1}(s) + \dfrac{1}{Z_{b12}(s)} + \dfrac{1}{Z_{b13}(s)}\right)\Delta u_{d1} = \dfrac{\Delta u_{d2}}{Z_{b12}(s)} + \dfrac{\Delta u_{d3}}{Z_{b13}(s)} + \dfrac{\Delta P_{ac1}^{ref}}{u_{d1(0)}} \\ \left(G_{c2}(s) + \dfrac{1}{Z_{b12}(s)} + \dfrac{1}{Z_{b23}(s)}\right)\Delta u_{d2} = \dfrac{\Delta u_{d1}}{Z_{b12}(s)} + \dfrac{\Delta u_{d3}}{Z_{b23}(s)} + \dfrac{\Delta P_{ac2}^{ref}}{u_{d2(0)}} \\ \left(G_{c3}(s) + \dfrac{1}{Z_{b13}(s)} + \dfrac{1}{Z_{b23}(s)}\right)\Delta u_{d3} = \dfrac{\Delta u_{d1}}{Z_{b13}(s)} + \dfrac{\Delta u_{d2}}{Z_{b23}(s)} \end{cases} \tag{6-11}$$

where,

$$G_{c1}(s) = sC_{c1} + g_{d1(0)}, \quad G_{c2}(s) = sC_{c2} + g_{d2(0)}, \quad G_{c3}(s) = 3u_{s3}^{d}K_{Pv}/2u_{d3(0)} = k_g \tag{6-12}$$

(6-11) and (6-12) lay the foundation for the DC-side small-signal stability of the three-terminal VSC-HVDC system. However, it is difficult to derive an analytical stability criterion directly due to the relatively high order of the system equations expressed by (6-11) and (6-12). To address this issue, the DFA is adopted in this thesis to simplify the analysis.

### 6.3.2 Natural Oscillation Frequencies of the Three-Terminal VSC-HVDC System

Since the DC-side instability originates from the resonance between the inductance and capacitance components in the DC network, the resistance components in the network are omitted to determine the natural oscillation frequencies in the DC link. In addition, it is assumed that the terminal voltage of $VSC_3$ keeps constant with the CDVC. Accordingly, the original network is simplified to a pure reactance network, as illustrated by Fig. 6-2.

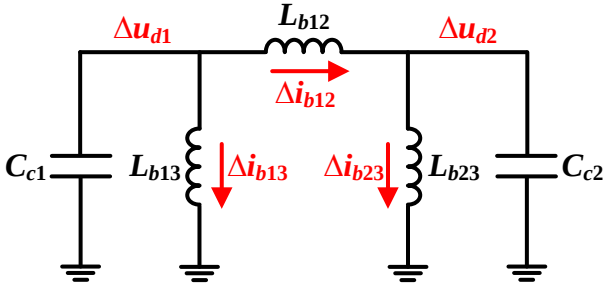


Fig. 6-2 Simplified pure reactance network of the three-terminal VSC-HVDC system.

As per (6-11) and (6-12), the transfer function between $\Delta u_{d2}$ and $\Delta P_{ac2}^{ref}$ are reduced according to the simplified pure reactance network as,

$$\frac{\Delta u_{d2}}{\Delta P_{ac2}^{ref}} = \frac{sL_{b12}}{u_{d1(0)}\left(sL_{b12}\left(sC_{c1}+\frac{1}{sL_{b12}}+\frac{1}{sL_{b13}}\right)sL_{b12}\left(sC_{c2}+\frac{1}{sL_{b12}}+\frac{1}{sL_{b23}}\right)-1\right)} \tag{6-13}$$

Based on (6-13), the characteristic function of the simplified network is obtained as,

$$\begin{aligned} D_n(s) &= sL_{b12}\left(sC_{c1}+\frac{1}{sL_{b12}}+\frac{1}{sL_{b13}}\right)sL_{b12}\left(sC_{c2}+\frac{1}{sL_{b12}}+\frac{1}{sL_{b23}}\right)-1 \\ &= \left(s^2L_{b12}C_{c1}+\frac{L_{b12}}{L_{b13}}+1\right)\left(s^2L_{b12}C_{c2}+\frac{L_{b12}}{L_{b23}}+1\right)-1 \\ &= \left(s^2L_{b12}C_{c1}+\frac{L_{b12}}{L_{b13}}\right)\left(s^2L_{b12}C_{c2}+\frac{L_{b12}}{L_{b23}}\right)+s^2L_{b12}C_{c1}+\frac{L_{b12}}{L_{b13}}+s^2L_{b12}C_{c2}+\frac{L_{b12}}{L_{b23}} \\ &\approx \left(s^2L_{b12}C_{c2}+\frac{L_{b12}}{L_{b23}}\right)\left(s^2L_{b12}C_{c1}+\frac{L_{b12}}{L_{b13}}+1+\frac{C_{c1}}{C_{c2}}\right) \end{aligned} \tag{6-14}$$

(6-14) indicates that there exist two natural oscillation frequencies in the studied system, which is different from the two-terminal DC link that only possesses a single resonance oscillation frequency. By setting the characteristic function expressed by (6-14) as zero, the expressions of the natural frequencies can be written as,

$$\begin{cases} \omega_{n1} = \dfrac{1}{\sqrt{L_{b23}C_{c2}}} \\ \omega_{n2} = \sqrt{\dfrac{1}{L_{b12}C_{c1}}+\dfrac{1}{L_{b12}C_{c2}}+\dfrac{1}{L_{b13}C_{c1}}} \end{cases} \tag{6-15}$$

Compared with (5-29) and (6-15), it is found that one natural oscillation frequency of the three-terminal DC network is similar to that of the two-terminal DC link. The other one is associated with the topology of the network, which ascends with the increase in the number of converters.

### 6.3.3 DFA-Based Model Reduction of the Three-Terminal VSC-HVDC System

After determining the natural oscillation frequencies in the DC network, the model reduction can be conducted on (6-11) nearby the dominant frequencies.

Rearranging the third equation in (6-11), it yields that,

$$\Delta u_{d3} = \frac{\Delta u_{d1}}{Z_{b13}(s)G_{c3}(s) + Z_{b13}(s)/Z_{b23}(s) + 1} + \frac{\Delta u_{d2}}{Z_{b23}(s)G_{c3}(s) + Z_{b23}(s)/Z_{b13}(s) + 1} \quad (6\text{-}16)$$

In the neighbourhood of the natural oscillation frequencies, the transmission resistance is far less than the transmission reactance, and thus,

$$\frac{Z_{b13}(s)}{Z_{b23}(s)} = \frac{sL_{b13} + R_{b13}}{sL_{b23} + R_{b23}} \approx \frac{L_{b13}}{L_{b23}} \quad (6\text{-}17)$$

Based on (6-17), (6-16) can be further simplified in the vicinity of the natural oscillation frequencies as follows.

$$\Delta u_{d3} \approx \frac{\Delta u_{d1}}{(sL_{b13} + R_{b13})k_g + L_{b13}/L_{b23} + 1} + \frac{\Delta u_{d2}}{(sL_{b23} + R_{b23})k_g + L_{b23}/L_{b13} + 1} \quad (6\text{-}18)$$

Substitution of $s = j\omega_n$ into (6-18) provides,

$$\begin{aligned} \Delta u_{d3} &\approx \frac{\Delta u_{d1}}{R_{b13}k_g + L_{b13}/L_{b23} + 1 + j\omega_n L_{b13}k_g} + \frac{\Delta u_{d2}}{R_{b23}k_g + L_{b23}/L_{b13} + 1 + j\omega_n L_{b23}k_g} \\ &\approx \frac{\Delta u_{d1}}{j\omega_n L_{b13}k_g} + \frac{\Delta u_{d2}}{j\omega_n L_{b23}k_g} \end{aligned} \quad (6\text{-}19)$$

The relationships expressed by (6-19) hold because the imaginary parts are far larger than the real parts in the vicinity of the natural oscillation frequencies.

Multiplying $Z_{b13}(s)$ on both sides of the first equation in (6-11) yields,

$$\left(Z_{b13}(s)G_{c1}(s) + \frac{Z_{b13}(s)}{Z_{b12}(s)} + 1\right)\Delta u_{d1} = \frac{Z_{b13}(s)}{Z_{b12}(s)}\Delta u_{d2} + \Delta u_{d3} + \frac{Z_{b13}(s)\Delta P_{ac1}^{ref}}{u_{d1(0)}} \quad (6\text{-}20)$$

Similarly, (6-20) can be simplified as,

$$\left(Z_{b13}(s)G_{c1}(s) + \frac{L_{b13}}{L_{b12}} + 1\right)\Delta u_{d1} = \frac{L_{b13}}{L_{b12}}\Delta u_{d2} + \Delta u_{d3} + \frac{Z_{b13}(s)\Delta P_{ac1}^{ref}}{u_{d1(0)}} \quad (6\text{-}21)$$

Substitution of (6-19) into (6-21), the following relations hold in the vicinity of the natural oscillation frequencies.

$$\begin{aligned} \Delta u_{d1} &= \frac{\left(L_{b13}/L_{b12} + 1/j\omega_n L_{b13}k_g\right)\Delta u_{d2} + \left(Z_{b13}(s)/u_{d1(0)}\right)\Delta P_{ac1}^{ref}}{Z_{b13}(s)G_{c1}(s) + L_{b13}/L_{b12} + 1 - 1/j\omega_n L_{b13}k_g} \\ &\approx \left(\frac{L_{b13}}{L_{b12}c_1} - \frac{j\omega_n c_2}{c_1^2}\right)\Delta u_{d2} + \frac{Z_{b13}(s)\Delta P_{ac1}^{ref}}{u_{d1(0)}\left(Z_{b13}(s)G_{c1}(s) + L_{b13}/L_{b12} + 1 - 1/j\omega_n L_{b13}k_g\right)} \end{aligned} \quad (6\text{-}22)$$

where,

$$\begin{cases} c_1 = L_{b13}/L_{b12} + 1 - \omega_n^2 L_{b13} C_{c1} \\ c_2 = \dfrac{L_{b13}^2 g_{d1(0)}}{L_{b12}} + \dfrac{L_{b13} R_{b13} C_{c1}}{L_{b12}} + \dfrac{1}{\omega_n^2 k_g}\left(\dfrac{L_{b12}+L_{b13}+L_{b23}}{L_{b12}L_{b23}}\right) - \dfrac{L_{b13}C_{c1}}{L_{b23}k_g} \end{cases} \tag{6-23}$$

Multiplying $Z_{b12}(s)$ on both sides of the second equation in (6-11) yields,

$$\left(G_{c2}(s)Z_{b12}(s) + \frac{Z_{b12}(s)}{Z_{b23}(s)} + 1\right)\Delta u_{d2} = \Delta u_{d1} + \frac{Z_{b12}(s)}{Z_{b23}(s)}\Delta u_{d3} + \frac{Z_{b12}(s)}{u_{d2(0)}}\Delta P_{ac2}^{ref} \tag{6-24}$$

Substituting (6-17) and (6-19) into (6-24), it provides that,

$$\left(G_{c2}(s)Z_{b12}(s) + 1 + \frac{L_{b12}}{L_{b23}}\left(1 - \frac{1}{j\omega_n L_{b23} k_g}\right)\right)\Delta u_{d2} = \left(1 + \frac{L_{b12}}{j\omega_n L_{b13} L_{b23} k_g}\right)\Delta u_{d1} + \frac{Z_{b12}(s)}{u_{d2(0)}}\Delta P_{ac2}^{ref} \tag{6-25}$$

Combined with (6-22) and (6-25) yields the following equation.

$$\begin{aligned} &\left(s^2 L_{b12}C_{c2} + s\left(L_{b12}g_{d2(0)} + R_{b12}C_{c2} + \frac{L_{b12}}{\omega_n^2 L_{b23}^2 k_g}\right) + 1 + \frac{L_{b12}}{L_{b23}} - \frac{L_{b13}}{L_{b12}c_1} + j\omega_n\left(\frac{c_2}{c_1^2} + \frac{1}{\omega_n^2 c_1 k_g L_{b23}}\right)\right)\Delta u_{d2} \\ &= \frac{\left(1 + L_{b12}/j\omega_n L_{b13} L_{b23} k_g\right)Z_{b13}(s)}{u_{d1(0)}\left(Z_{b13}(s)G_{c1}(s) + L_{b13}/L_{b12} + 1 - 1/j\omega_n L_{b13} k_g\right)}\Delta P_{ac1}^{ref} + \frac{Z_{b12}(s)}{u_{d2(0)}}\Delta P_{ac2}^{ref} \end{aligned} \tag{6-26}$$

Based on (6-26), the transfer function between $\Delta u_{d2}$ and $\Delta P_{ac1}^{ref}$ can be obtained as,

$$\frac{\Delta u_{d2}}{\Delta P_{ac2}^{ref}} = \frac{N(s)}{D_1(s)D_2(s)} \tag{6-27}$$

where,

$$\begin{cases} N(s) = \dfrac{sL_{b13}L_{b23}k_g + L_{b12}}{u_{d1(0)}L_{b23}k_g} \\ D_1(s) = s^2 L_{b12}C_{c2} + s\left(L_{b12}g_{d2(0)} + R_{b12}C_{c2} + \dfrac{L_{b12}}{\omega_n^2 L_{b23}^2 k_g} + \dfrac{c_2}{c_1^2} + \dfrac{1}{\omega_n^2 c_1 k_g L_{b23}}\right) + 1 + \dfrac{L_{b12}}{L_{b23}} - \dfrac{L_{b13}}{L_{b12}c_1} \\ D_2(s) = s^2 L_{b13}C_{c1} + s\left(L_{b13}g_{d1(0)} + R_{b13}C_{c1} + \dfrac{1}{\omega_n^2 L_{b13} k_g}\right) + \dfrac{L_{b13}}{L_{b12}} + 1 \end{cases} \tag{6-28}$$

(6-27) and (6-28) constitute the reduced-order model of the three-terminal VSC-HVDC system. As a result, the small-signal stability of the system is determined by analysing the zeros of the denominators $D_1(s)$ and $D_2(s)$.

### 6.3.4 Analytical DC-Side Stabilising Condition of the Three-Terminal VSC-HVDC System

Since $VSC_1$ serves as a rectifier, the equivalent DC-side conductance $g_{d1(0)}$ is positive, and the following inequality holds.

$$L_{b13}g_{d1(0)}+R_{b13}C_{c1}+\frac{1}{\omega_n^2 L_{b13}k_g}>0 \tag{6-29}$$

Based on (6-29), $D_2(s)$ has two negative roots so that the corresponding modes will not cause instability. Consequently, the DC-side stability of the system is determined by the roots of $D_1(s)$. Based on (6-23) and (6-28), the stability criterion of the three-terminal VSC-HVDC system is derived as,

$$a_1=L_{b12}g_{d2(0)}+\frac{L_{b13}^2 g_{d1(0)}}{c_1^2 L_{b12}}+R_{b12}C_{c2}+\frac{L_{b13}R_{b13}C_{c1}}{c_1^2 L_{b12}}+\frac{L_{b12}}{\omega_n^2 L_{b23}k_g}+\frac{L_{b12}+L_{b13}+L_{b23}}{c_1^2\omega_n^2 L_{b12}L_{b13}k_g}-\frac{L_{b13}C_{c1}}{c_1^2 L_{b23}k_g}>0 \tag{6-30}$$

(6-30) indicates that the system damping is related to all three converters. Once the positive damping brought by the CPC-based rectifier, the CDVC-based VSC, and the transmission resistance cannot overset the negative damping introduced by the CPC-based inverter, DC-side instability will occur in the DC system. In addition, the operating point is influential to the stability properties. The system damping can be enhanced by increasing the transferred power of the CPC-based rectifier or decreasing the transfer power of the CDVC-based inverter.

Taking the derivative of (6-30) with respect to $K_{Pv}$ yields,

$$\frac{\partial a_1}{\partial K_{Pv}}=-\frac{2u_{d3(0)}}{3u_{s3}^d K_{Pv}^2}\left(\frac{L_{b12}}{\omega_n^2 L_{b23}}+\frac{L_{b12}+L_{b13}+L_{b23}}{c_1^2\omega_n^2 L_{b12}L_{b13}}-\frac{L_{b13}C_{c1}}{c_1^2 L_{b23}}\right)<0 \tag{6-31}$$

Based on (6-31), increasing the proportional gain of the CDVC will degrade the stability properties. This is because the positive damping of the CDVC-based VSC decreases as the proportional gain increases.

## 6.4 DC-Side Stability Analysis of Generic MTDC Systems

The above analysis is based on a three-terminal VSC-HVDC system as an example. Notably, the DFA can be extended to the stability analysis of generic MTDC systems, which is introduced as follows.

### 6.4.1 Frequency Domain Model of Generic MTDC Systems

For the convenience of analysis, the nodes connected to the LCC are numbered from 1 to $M_1$, the nodes connected to the CPC-based VSC are numbered from ($M_1$+1) to ($M_1$+$M_2$), the nodes connected to the droop-based VSC are numbered from ($M_1$+$M_2$+1) to ($M_1$+$M_2$+ $M_3$), while the nodes connected to the CDVC-based VSC are numbered from ($M_1$+$M_2$+ $M_3$+1) to $M$ ($M$ = $M_1$+ $M_2$+$M_3$+$M_4$). Based on (6-1), (6-3), (6-5), and (6-7), the dynamics of all

converters in the MTDC system are expressed in a compact form as,

$$\Delta \boldsymbol{i}_{\boldsymbol{dc}} = -\boldsymbol{G}_{\boldsymbol{c}}(s)\Delta \boldsymbol{u}_{\boldsymbol{d}} + \boldsymbol{G}_{\boldsymbol{u}}(s)\Delta \boldsymbol{u} \tag{6-32}$$

where,

$$\Delta \boldsymbol{i}_{\boldsymbol{dc}} = \left[\Delta i_{dc1}, \Delta i_{dc2}, \cdots, \Delta i_{dcM}\right]^T,$$

$$\Delta \boldsymbol{u}_{\boldsymbol{d}} = \left[\Delta u_{d1}, \Delta u_{d2}, \cdots, \Delta u_{dM}\right]^T,$$

$$\Delta \boldsymbol{u} = \left[\Delta i_{dc1}^{ref}, \cdots, \Delta i_{dcM_1}^{ref}, \Delta P_{ac(M_1+1)}^{ref}, \cdots, \Delta P_{ac(M_1+M_2+M_3)}^{ref}, \Delta u_{d(M_1+M_2+M_3+1)}^{ref}, \cdots, \Delta u_{dM}^{ref}\right]^T,$$

$$\boldsymbol{G}_{\boldsymbol{c}}(s) = \mathrm{diag}\left\{G_{c1}(s), \cdots, G_{cM_1}(s), G_{c(M_1+1)}(s), \cdots, G_{c(M_1+M_2)}(s), G_{c(M_1+M_2+1)}(s), \cdots, G_{c(M_1+M_2+M_3)}(s), G_{c(M_1+M_2+M_3+1)}(s), \cdots, G_{cM}(s)\right\},$$

$$\boldsymbol{G}_{\boldsymbol{u}}(s) = \mathrm{diag}\left\{G_{u1}(s), \cdots, G_{uM_1}(s), G_{u(M_1+1)}(s), \cdots, G_{u(M_1+M_2+M_3)}(s), G_{u(M_1+M_2+M_3+1)}(s), \cdots, G_{uM}(s)\right\}.$$

The frequency domain model of the DC network is written as,

$$\Delta \boldsymbol{i}_{\boldsymbol{dc}} = \boldsymbol{Y}(s)\Delta \boldsymbol{u}_{\boldsymbol{d}} \tag{6-33}$$

where $\boldsymbol{Y}(s)$ is the transfer function matrix of the network admittance.

Combined with (6-32) and (6-33), the transfer function matrix between the node voltage and the perturbation of the reference value of converter control can be obtained as follows.

$$\frac{\Delta \boldsymbol{u}_{\boldsymbol{d}}}{\Delta \boldsymbol{u}} = \frac{\boldsymbol{G}_{\boldsymbol{u}}(s)}{\boldsymbol{G}_{\boldsymbol{c}}(s) + \boldsymbol{Y}(s)} \tag{6-34}$$

(6-34) is the frequency domain model of generic MTDC systems, which lays a foundation for the small-signal stability analysis.

### 6.4.2 DC-Side Stabilising Condition of Generic MTDC Systems Based on DFA

Based on (6-34), the dynamic equation of $\Delta u_{di}$ under a specified perturbation of $\Delta u_j$ is expressed as,

$$D(s)\Delta u_{di} = G_{uj}(s)\Delta u_j \tag{6-35}$$

Since $G_{uj}(s)$ has no positive root, the small-signal stability of the MTDC system is merely determined by the roots of the following equation based on (6-35).

$$D(s) = 0 \tag{6-36}$$

The DFA is utilised to reduce the order of $D(s)$ in the neighbourhood of the dominant frequency. As shown in Fig. 6-3, the frequency sweeping method is adopted to determine the dominant oscillation frequencies of the DC network. The basic procedures of the method are

introduced as follows. Firstly, calculate the absolute value of $D(j\omega)$ for all $\omega$ in the range of $[\omega^{\min}, \omega^{\max}]$ with a step of $\Delta\omega$. Secondly, find all the local minimum points of $D(j\omega)$. Thirdly, save the frequencies corresponding to all the local minimum points as the approximated dominant frequencies of the system. Denote the dominant frequencies as $\omega_{d1}$, $\omega_{d2}$, ⋯, $\omega_{dK}$. Obviously, any dominant frequency is the root of the following equation.

$$h(s) = s^2 + \omega_{di}^2 = 0, \quad i = 1, 2, \cdots, K \tag{6-37}$$

The characteristic function $D(s)$ can be rewritten as,

$$D(s) = s^2 + \omega_{di}^2 + H(s) = 0, \quad H(s) = D(s) - s^2 - \omega_{di}^2 \tag{6-38}$$

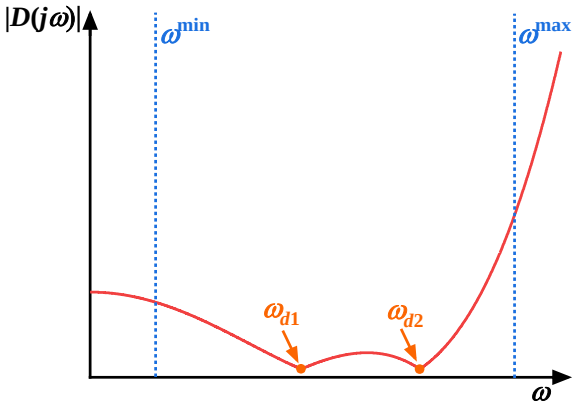


Fig. 6-3 Diagram of the frequency sweeping method.

In the vicinity of the dominant frequency, (6-38) can be approximated as,

$$s^2 + \omega_{di}^2 + \mathrm{Re}\left(H(j\omega_{di})\right) + j\,\mathrm{Im}\left(H(j\omega_{di})\right) \approx s^2 + s\frac{\mathrm{Im}\left(H(j\omega_{di})\right)}{\omega_{di}} + \omega_{di}^2 + \mathrm{Re}\left(H(j\omega_{di})\right) = 0 \tag{6-39}$$

The system damping under the dominant frequencies much be positive to ensure stability. Therefore, the DC-side stabilising condition of the system can be expressed as follows based on (6-39).

$$\left.\frac{\mathrm{Im}\left(H(s)\right)}{\omega_{di}}\right|_{s=j\omega_{di}} > 0 \quad \Rightarrow \quad \mathrm{Im}\left(D(j\omega_{di})\right) > 0, \quad i = 1, \cdots, K \tag{6-40}$$

(6-40) indicates that the small-signal stability determination can be achieved by examining the damping nearby by the dominant frequencies. In this way, the order of the system model can be reduced. Traditionally, the control parameters are chosen to improve the dynamic properties. Meanwhile, the parameters cannot make the system unstable, which is checked via modal analysis. The DFA-based method can reduce the model complexity without losing principal stability properties, thus providing a clear relationship between system

parameters and stability. As a result, system stability can be ensured by serving the analytical stabilizing condition as an inequality constraint during control design, which gets rid of the repeated time-consuming eigenvalue calculations.

## 6.5 Case Studies

A three-terminal VSC-HVDC system illustrated by Fig. 6-1 is established based on PSCAD/EMTDC to validate the correctness of the DFA-based model reduction and the proposed stabilising condition. The nominal voltage of the AC and that of the DC system are 220 kV and ±200 kV, respectively. Three converters are represented by the detailed switching model with the master-slave control strategy, i.e., $VSC_1$ serves as a rectifier with the CPC, $VSC_2$ serves as an inverter with the CPC, while $VSC_3$ regulates the voltage of the DC network. The reference active power of $VSC_1$ and $VSC_2$ are set as 300 MW and -250 MW, individually. The reference DC-link voltage is configured as 400 kV. The time constant of each VSC is 2 ms. The DC-link capacitor of each VSC is 200 μF. The DC transmission lines connecting the VSCs adopt the frequency-dependent model. The lengths of Line 12, Line 13, and Line 23 are 200 km, 150 km, and 100 km, individually. To restrict the capacitor discharging current, DC supplementary reactors of 50 mH are deployed at the terminal of each transmission line. The main parameters of the test system are summarized in Table 6-1.

Table 6-1 Main parameters of the test three-terminal VSC-HVDC system

| Symbol | Item | Value |
|---|---|---|
| $u_n$ | Nominal DC-link voltage of the test system | ±200 kV |
| $u_s$ | Nominal voltage of VSC-tied AC source | 220 kV |
| $C_c$ | DC-link capacitance of TLVSCs | 200 μF |
| $L_T$ | Inductance of DC reactors | 50 μH |
| $\sigma_i$ | Time constant of the inner loop | 2 ms |
| ($K_{Po}$, $K_{Io}$) | Proportional and integral gains of the CPC | (1, 10) |
| ($K_{Pv}$, $K_{Iv}$) | Proportional and integral gains of the CDVC | (1, 10) |
| $P_{ac1}^{ref}$ , $P_{ac2}^{ref}$ | Reference active power of $VSC_1$ and $VSC_2$ | 300 MW, -250 MW |
| $u_d^{ref}$ | Reference DC-link voltage | 400 kV |
| $R_0$ | Per-kilometre resistance of DC line | 0.015 Ω |
| $L_0$ | Per-kilometre inductance of DC line | 1.7 mH |
| $l_{12}$, $l_{13}$, $l_{23}$ | Lengths of Line 12, Line 13, and Line 23 | 200 km, 150 km, 100 km |

Fig. 6-4 shows the dynamic responses of the test system with different system parameters

under a sudden change of the reference active power of $VSC_2$ from -250 MW to -300 MW. As depicted in Fig. 6-4 (a), there are oscillations in the DC-link current after the power alternation. Based on (6-15), the dominant frequency of the system is calculated as 135.67 rad/s. By applying the DFA, the damping ratio and the oscillation frequency of the perturbed system are calculated as 0.0088 and 137.58 rad/s based on (6-28). It can be found that the dominant frequency estimation based on (6-15) is very close to the actual frequency, indicating that the dominant oscillation frequency in the MTDC system is mainly determined by the inductance and capacitance components in the DC network. Fig. 6-4 (b) illustrates the dynamics of the DC-link current under the power alternation when the DC supplementary reactors $L_{T12}$ and $L_{T21}$ increase to 300 mH. It is shown that apparent divergent oscillations appear after the disturbance. This is because the increase of the branch inductance can amplify the negative damping brought by $VSC_2$ based on (6-30). In this situation, the system damping ratio reduces to -0.0059, implying that the studied system losses the DC-side stability. Besides, the estimated and the actual oscillation frequency are 111.18 rad/s and 112.36 rad/s, which decrease with the increase of the branch inductance. Fig. 6-4 (c) illustrates that the studied system can be stabilised by scaling up the DC-link capacitor of $VSC_2$ to 250 μF. Based on (6-30), the positive damping effects induced by the transmission resistance can be amplified by increasing the DC-link capacitance. The system damping ratio changes to 0.0244 in this situation, which indicates that the positive damping offsets the negative damping in the DC system so that the DC-side stability of the MTDC system can be ensured. It is noted that the estimated and the actual oscillation frequency reduce to 108.76 rad/s and 108.73 rad/s, implying that the increase of the DC-link capacitance can also increase the oscillation frequency in the DC link. Moreover, it is observed that the DFA-based analysis results align with the simulation results under various system parameters, which manifests the accuracy of the DFA in small-signal stability analysis of the MTDC system.

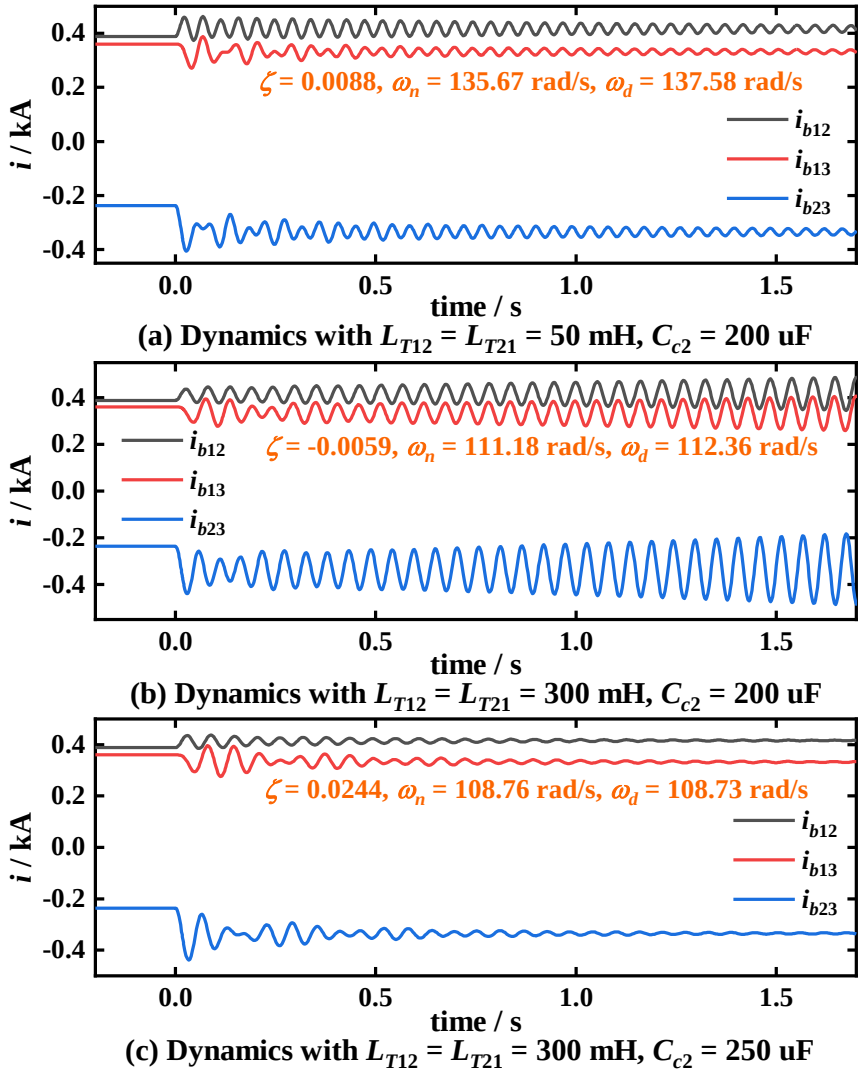


Fig. 6-4 Dynamic responses with different system parameters under a sudden power alternation.

Fig. 6-5 presents the dynamics of the DC-link current under different power alternation disturbances. Fig. 6-5 (a) shows the dynamic responses of the system when the active power of $VSC_1$ suddenly increases to 500 MW. After the perturbation, oscillations appear in the DC link and get damped faster than those shown in Fig. 6-4 (a). This can be explained by the fact that the positive damping of the CPC-based rectifier enlarges as the transfer power increases based on (6-30). Based on (6-28), the system damping ratio is calculated as 0.0258. In addition, the oscillation frequency is calculated as 137.35 rad/s, which is close to the estimated value of 135.67 rad/s. This indicates the transfer power of the VSC has negligible influences on the oscillation frequency. Fig. 6-5 (b) depicts the system dynamics when the reference active power of $VSC_1$ suddenly decreases to 0 MW. It is observed that the branch current of every transmission line exhibits divergent oscillations. The reason is that $VSC_1$ no longer provides positive damping to the DC link with 0 power transfer, and the system damping

decreases to -0.0064. Similarly, Fig. 6-5 (c) and (d) depict the system dynamics when the power alternation of $VSC_2$ occurs. As illustrated by Fig. 6-5 (c), the DC-side stability deteriorates when the reference active power of $VSC_2$ changes from -250 MW to -500 MW, which implies $VSC_2$ brings about larger negative damping to the DC-link. Accordingly, the system damping ratio decreases to -0.0105, and intense oscillations appear in the branch current. In constrast, when the reference active power of $VSC_2$ alters to 0 MW, $VSC_2$ does not induce negative damping to the DC network. In this situation, the damping ratio increases to 0.0332, and the DC-side oscillation can be damped. The simulation results under various operating points again verify the effectiveness of the DFA-based model reduction and the proposed stabilising condition as expressed by (6-30).

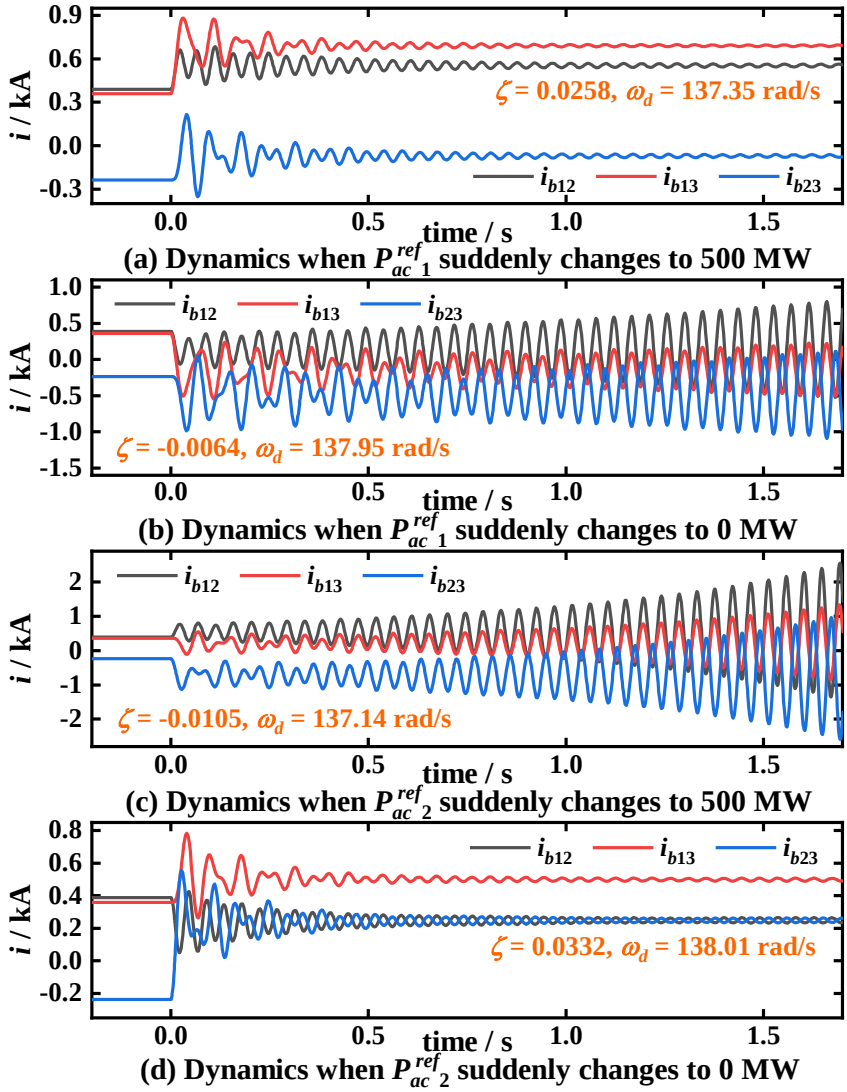


Fig. 6-5 Dynamic responses with different power alternations.

Fig. 6-6 presents the dynamic responses of the studied MTDC system when the reference

active power of $VSC_1$ suddenly descends from 300 MW to 0 MW with different control parameters. As shown in Fig. 6-6 (a), apparent divergent oscillations appear in the DC network when the proportional gain of the CDVC increases to 5. This is because the positive damping provided by the CDVC-based VSC is inversely proportional to the proportional gain based on (6-30). In this situation, $VSC_1$ does not provide damping to the DC system, while the positive damping provided by the CDVC-based VSC and the transmission resistance cannot overwhelm the negative damping induced by the CPC-based inverter. As a result, the system damping ratio decreases to -0.0079, and the MTDC system is destabilised. In contrast, when the proportional gain of the CDVC drops to 0.05, the damping ratio increases to 0.0031. Accordingly, DC-side oscillations gradually decay, and the MTDC system keeps stable under the perturbation. In addition, it is observed that the change in the oscillation frequency is rather small with different proportional gains, indicating that the control parameters have negligible impacts on the oscillation frequency of the DC network. Consequently, the dominant frequency estimation based on (6-15) is accurate. The DFA-based analysis results are in line with the numerical simulation results under various control parameters, which again validates the correctness of the proposed method.

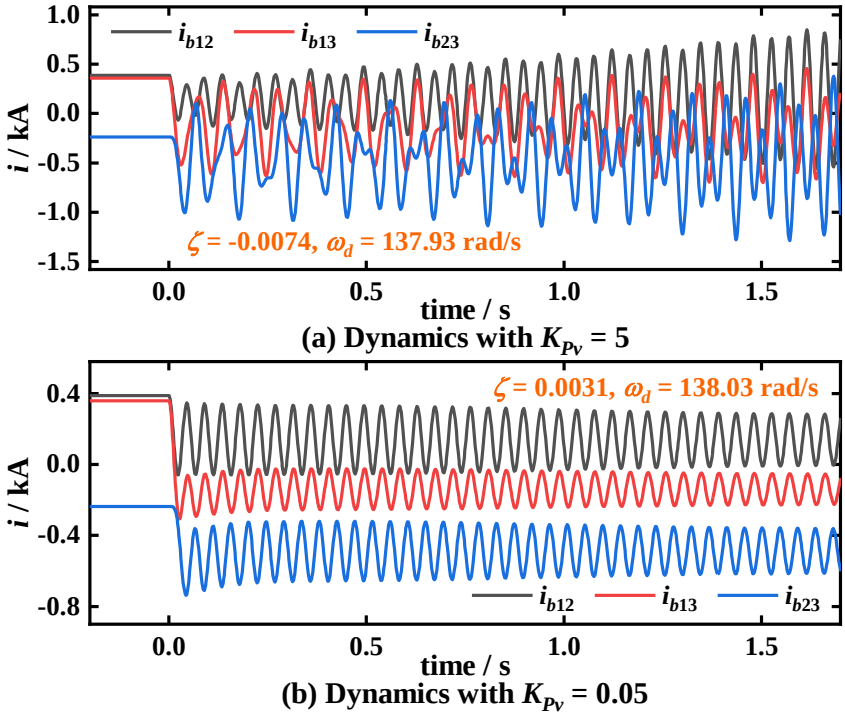


Fig. 6-6 Dynamic responses with different control parameters under a sudden power alternation.

## 6.6 Summary

This chapter investigates the DC-side stability of the MTDC system based on DFA. The frequency domain model of the MTDC system is first established, which lays a foundation for the stability analysis. Considering the dominant frequency of the system is mainly determined by the inductance and capacitance components in the DC network, the pure reactance network of the MTDC system is used to estimate the dominant frequencies. In addition, the dominant frequencies of the MTDC system can also be determined by applying the frequency sweeping method on the characteristic equation of the system. By using DFA, the original system model can be significantly reduced in the vicinity of the dominant frequencies. As a result, the analytical stabilising condition of the MTDC system can be derived. It is indicated the DC-side instability mechanism of MTDC systems is that when the positive damping provided by the CPC-based rectifier, the CDVC-based converter, and the transmission reactance cannot offset the negative damping generated from the CPC-based inverter, DC-side instability will appear in the MTDC system. In other words, the MTDC system keeps stable only if the system damping nearby every dominant frequency is positive. Moreover, it is found that the DC-side stability can be enhanced by decreasing the transmission inductance and the proportional gain of the CDVC or scaling up the DC-link capacitors. Numerical simulation studies validate the accuracy of the DFA-based model reduction and the derived stabilising condition of the MTDC system.

# 7 Conclusion and Future Work

## 7.1 Conclusion

MTDC systems enable multi-point power supply and reception, which maximise the economic and flexible advantages of DC transmission. Consequently, MTDC systems have wide application foreground in large-bark long-distance power transmission. As one of the most critical components in MTDC systems, the converter takes a vital role in the systems' dynamic responses. The flexible and diversified control systems make the dynamic properties of MTDC systems rather complicated. Under server DC faults, intensive current surges will appear in the DC network due to the natural discharging of the DC-link capacitor, which may injure the vulnerable converters. Under more general small perturbations, there exists the risk of divergent oscillations in the DC-link current with poor control parameters, which may result in the blocking of converters and even the interruption of the entire system. Therefore, exploring the dynamic properties of MTDC systems to guide the protection and control design for such systems is urgent.

This thesis mainly focuses on the DC-side dynamic behaviours of MTDC systems, including the converter modelling, fault analysis, and stability analysis of MTDC systems. The conclusion of this thesis is summarized as follows.

1. The linear models of three types of converters for DC-side dynamic analysis. Depending on the DC-link voltage derivations of the converter, the small-signal analysis and the least squares approximation can be utilised to deduce the linear model of the LCC, TLVSC, and MMC. It is indicated that the effects of the constant current control of the LCC can be equivalent to an RC series circuit. In contrast, the control effects of the TLVSC can be equivalent to an RL series circuit. The control mode, such as the CPC, CDVC, and droop control, will influence the equivalent parameters of the circuit. As for the MMC, its external characteristics are similar to those of the TLVSC, and thus the equivalent model of the MMC is analogous to that of the TLVSC. It is concluded that the three converters (the LCC, TLVSC, and MMC), considering the control effects, can be equivalent to simple RLC circuits from the DC side.

2. A state-space-based fault calculation method for generic MTDC systems. Since converters and the DC network can be represented by linear models, the superposition principle is applicable to facilitate the fault analysis of generic MTDC systems. The state-

space equation of the fault component network is derived so that the analytical expression of the fault current in the whole network can be obtained by solving the initial value problem of ordinary differential equations. The proposed method has wide applicability to various MTDC systems with different network topologies, converters types, and control modes. It also achieves relatively high accuracy without the numerical solution of DAEs.

3. A simple fault calculation method for VSC-MTDC systems by using the HFE. According to the HFE, the low-frequency components of the fault component network can be omitted to simplify the initial fault analysis because only the high-frequency electrical quantities dominate the Laplace circuit within the first milliseconds after faults. It is found that the parallel connected branches with the grounded capacitor can be overlooked when calculating the fault component current of the fault line, while the fault component current of the healthy line equals that of the fault line times a second-order low-pass LC filter. In addition, the fault component current of the fault line grows linearly, while that of the healthy line rises cubically within several milliseconds after the DC fault. By using the HFE, the proposed method achieves a more straightforward DC fault analysis of VSC-MTDC systems with simple calculations and little loss of accuracy.

4. The DC-side damping properties and small-signal stability analysis of converters. The single converter to an ideal DC source system is utilised to investigate the DC-side damping properties of different converters. It is revealed that the LCC always exhibits positive damping, which increases when enlarging the proportional gain or reducing the integral gain of the constant current controller. The damping properties of the VSC is relevant to the control mode. For the CPC-based VSC, its damping is irrespective of the control parameters. It provides positive damping when serving as a rectifier, while it induces negative damping when operating as an inverter. In contrast, the damping of the CDVC-based VSC has less sensitivity to the power transfer, which is usually positive with typical control parameters. As for the droop-based VSC, both the control parameters and the transfer power will influence its damping, and increasing the droop gain can significantly enhance the damping properties. In addition, it is found that different converters can jointly determine the DC-side stability of the DC link by studying the two-terminal VSC-HVDC system. DC-side instability occurs when the positive damping provided by the CDVC-based rectifier and the transmission resistance cannot offset the negative damping brought by the CPC-based inverter.

5. DC-side stability analysis of generic MTDC systems by using DFA. An MTDC system may have several dominant frequencies, which can be estimated via the frequency sweeping

method. Since the system stability is determined by the dominant modes with small damping ratios, the model reduction can be conducted nearby the dominant frequencies without losing principal stability properties. Accordingly, the stability judgement is converted to check the damping under every dominant frequency. Based on the DFA, the analytical stabilising condition of the MTDC system is derived, which reveals that DC-side instability appears once the positive damping of the CPC-based rectifier, the CDVC-based inverter, and the transmission resistance cannot offset the negative damping of the CPC-based inverter. In addition, it is found that the DC-side stability can be enhanced by decreasing the transmission inductance and the proportional gain of the CDVC or scaling up the DC-link capacitors.

## 7.2 Future Work

This thesis proposes the linear model and investigates the dynamic behaviours of MTDC systems. To improve this study, the following work will be studied in the future.

1. For the converter modelling, the converter-connected AC system is assumed to be ideal for deriving the DC-side equivalent model of the converter. This makes the proposed model in this thesis inapplicable to analyze the dynamic process from AC-side disturbances. Therefore, how to form a simple converter model taking account of the dynamics of the AC system and the PLL will be the future work.

2. For the fault calculation, the travelling wave process is neglected to derive the analytical expressions of the fault current in the thesis. Although the travelling wave process can be represented by the distributed line model, it will introduce partial differential equations and hinder the analytical solution of the fault network. Consequently, a simple fault calculation method for MTDC systems considering the travelling wave process still needs further investigation.

3. For the stability analysis, this thesis mainly focuses on the DC-side stability originating from the resonance between inductance and capacitance components in the DC network. How to propose analytical stabilising conditions accounting for both AC- and DC-side stability remains to be investigated.

4. This thesis concentrates on the dynamic analysis of MTDC systems. How to design effective protection and control schemes of MTDC systems based on the analysis will be the future work.

# References


[1] Pulazza G, Zhang N, Kang C, et al. Transmission planning with battery-based energy storage transportation for power systems with high penetration of renewable energy[J]. IEEE Transactions on Power Systems, 2021, 36(6): 4928-4940.

[2] Wang W, Li G, Guo J. Large-scale renewable energy transmission by HVDC: Challenges and proposals[J]. Engineering, 2022, 19: 252-267.

[3] Li Y, Liu H, Fan X, et al. Engineering practices for the integration of large-scale renewable energy VSC-HVDC systems[J]. Global Energy Interconnection, 2020, 3(2): 149-157.

[4] Li S, Chen W, Yin X, et al. A novel integrated protection for VSC-HVDC transmission line based on current limiting reactor power[J]. IEEE Transactions on Power Delivery, 2020, 35(1): 226-233.

[5] Mathew E C, Sharma R, Das A. A fault tolerant scheme for integration of remote renewable energy sources with HVDC system[J]. IEEE Transactions on Power Delivery, 2020, 35(6): 2876-2884.

[6] Cardesin J, Alonso J M, Lopez-Corominas E, et al. Small-signal analysis of a low-cost power control for LCC series-parallel inverters with resonant current mode control for HID lamps[J]. IEEE Transactions on Power Electronics, 2005, 20(5): 1205-1212.

[7] Xiao H, Ren S, Li Y. Novel disturbance blocking criterion for reliable current differential protection of LCC-HVDC lines[J]. IEEE Transactions on Power Delivery, 2020, 36(1): 477-480.

[8] Wang SC, Gao S, Chen Z, et al. Analysis of the operating margin evaluation of multi-infeed LCC-HVDC systems based on the equivalent impedance[J]. IEEE Access, 2021, 9: 66268-66281.

[9] Li JP, Li YJ, Wang MH, et al. DC fault detection in hybrid MTDC systems using transient average of DC reactor voltage[J]. International Journal of Electrical Power & Energy Systems, 2023, 150(109093): 1-10.

[10] Li JP, Li YJ, Wang MH, et al. Analytical DC-side stabilizing conditions for hybrid HVDC links based on dominant frequency model reduction[J]. Energy Reports, 2023, 9: 806-818.

[11] Xue Y, Zhang XP, Yang C. Series capacitor compensated AC filterless flexible LCC HVDC with enhanced power transfer under unbalanced faults[J]. IEEE Transactions on Power Systems, 2019, 34(4): 3069-3080.

[12] Li JP, Li YJ, Yuan XT, et al. DC fault analysis and detection for offshore wind farms integration via MTDC[J]. Electric Power Automation Equipment, 2020, 40(12): 119-128.

[13] Li JP, Song GB, Yan JF, et al. Data-driven fault detection and classification for MTDC systems by integrating HCTSA and softmax regression[J]. IEEE Transactions on Power Delivery, 2022, 37(2): 893-904.

[14] Li JP, Li YJ, Du ZC, et al. Damping turning rule of virtual synchronous generator for global stability[J]. IEEE Transactions on Power Delivery, doi: 10.1109/TPWRD.2023.3250769.

[15] Li JP, Li YJ, Zhang Xu, et al. Fault analysis of converter interfaced generator embedded power system considering control mode switching[J]. IET Generation Transmission & Distribution, 2023, 17(7): 1525-1537.

[16] Cheng F, Yao L Z, Xu J, et al. A comprehensive AC fault ride-through strategy for HVDC link with serial-connected LCC-VSC hybrid inverter[J]. CSEE Journal of Power and Energy Systems, 2022, 8(1): 175-187.

[17] Renedo J, Garcia-Cerrada A, Rouco L, et al. Coordinated design of supplementary controllers in VSC-HVDC multi-terminal systems to damp electromechanical oscillations[J]. IEEE Transactions on Power Systems, 2021, 36(1): 712-721.

[18] Sun K, Liu Y, Xiao H, et al. Cross-seam hybrid MTDC system for integration and delivery of large-scale renewable energy[J]. Journal of Modern Power Systems and Clean Energy, 2021, 9(6): 1352-1362.

[19] Gonzalez-Torres J C, Damm G, Costan V, et al. A novel distributed supplementary control of multi-terminal VSC-HVDC grids for rotor angle stability enhancement of AC/DC systems[J]. IEEE Transactions on Power Systems, 2021, 36(1): 623-634.

[20] Zhang Q, McCalley J D, Ajjarapu V, et al. Primary frequency support through North American continental HVDC interconnections with VSC-MTDC systems[J]. IEEE Transactions on Power Systems, 2020, 36(1): 806-817.

[21] Li Z, Zhang T, Wang Y, et al. Fault self-recovering control strategy of bipolar VSC-MTDC for large-scale renewable energy integration[J]. IEEE Transactions on Power Systems, 2022, 37(4): 3036-3047.

[22] Cheng F, Wang Z, Yao L, et al. Coordinated control strategy for serial LCC-VSC hybrid MTdc with Islanded wind farms[C]. The 16th IET International Conference on AC and DC Power Transmission (ACDC 2020), Online, 2020.

[23] Li Z, He Y, Li Y Z, et al. Hybrid control strategy for AC voltage stabilization in bipolar VSC-MTDC[J]. IEEE Transactions on Power Systems, 2019, 34(1): 129-139.

[24] Song S, McCann R A, Jang G. Cost-based adaptive droop control strategy for VSC-MTDC system[J]. IEEE Transactions on Power Systems, 2021, 36(1): 659-669.

[25] Freytes J, Akkari S, Rault P, et al. Dynamic analysis of MMC-based MTDC grids: use of MMC energy to improve voltage behavior[J]. IEEE Transactions on Power Delivery, 2018, 34(1): 137-148.

[26] Li JP, Li YJ, Xiong LS, et al. DC fault analysis and transient average current based fault detection for radial MTDC system[C]. 2021 IEEE Power & Energy Society General Meeting (PESGM 2021), Washington DC, USA, Jul. 2021.

[27] Zhang C, Song G, Meliopoulos A P S, et al. Setting-less nonunit protection method for DC line faults in VSC-MTdc systems[J]. IEEE Transactions on Industrial Electronics, 2022, 69(1): 495-505.

[28] Li C, Li Y, Cao Y, et al. Virtual synchronous generator control for damping DC-side resonance of VSC-MTDC system[J]. IEEE Journal of Emerging and Selected Topics in Power Electronics, 2018, 6(3): 1054-1064.

[29] Li Y F, Tang G F, Wu Y N, et al. Modeling, analysis and damping control of DC grid[J]. Proceeding

of the CSEE, 2017, 37(12): 3372-3382 (in Chinese).

[30] Shu D, Ouyang Z, Yan Z. Multirate and mixed solver based cosimulation of combined transient stability, shifted-frequency phasor, and electromagnetic models: a practical LCC HVDC simulation study[J]. IEEE Transactions on Industrial Electronics, 2021, 68(6): 4954-4965.

[31] Gao S, Song Y, Chen Y, et al. Fast simulation model of voltage source converters with arbitrary topology using switch-state prediction[J]. IEEE Transactions on Power Electronics, 2022, 37(10): 12167-12181.

[32] Esparza M, Segundo-Ramírez J, Kwon J B, et al. Modeling of VSC-based power systems in the extended harmonic domain[J]. IEEE Transactions on Power Electronics, 2017, 32(8): 5907-5916.

[33] Liu S, Xu Z, Hua W, et al. Electromechanical transient modeling of modular multilevel converter based multi-terminal HVDC systems[J]. IEEE Transactions on Power Systems, 2014, 29(1): 72-83.

[34] Herath N, Filizadeh S. Improved Average-Value and Detailed Equivalent Models for Modular Multilevel Converters With Embedded Storage[J]. IEEE Transactions on Energy Conversion, 2022, 37(3): 1998-2008.

[35] Yang J, Fletcher J E, O'Reilly J. Short-circuit and ground fault analyses and location in VSC-based DC network cables[J]. IEEE Transactions on Industrial Electronics, 2012, 59(10): 3827-3837.

[36] Zhang Z, Xu Z. Short-circuit current calculation and performance requirement of HVDC breakers for MMC-MTDC systems[J]. IEEJ Transactions on Electrical and Electronic Engineering, 2016, 11(2): 168-177.

[37] Dong Y, Ma J, Wang S, et al. An accurate small signal dynamic model for LCC-HVDC[J]. IEEE Transactions on Applied Superconductivity, 2021, 31(8): 1-6.

[38] Lu J, Yuan X, Hu J, et al. Motion equation modeling of LCC-HVDC stations for analyzing DC and AC network interactions[J]. IEEE Transactions on Power Delivery, 2020, 35(3): 1563-1574.

[39] Li Y, Liu K, Zhu S, et al. DC side impedance modeling and stability analysis of VSC-MTDC system[J]. High Voltage Engineering, 2021, 47(2): 627-638 (in Chinese).

[40] Hao Q, Li Z, Gao F, et al. Reduced-order small-signal models of modular multilevel converter and MMC-based HVDC grid[J]. IEEE Transactions on Industrial Electronics, 2018, 66(3): 2257-2268.

[41] Daryabak M, Filizadeh S, Jatskevich J, et al. Modeling of LCC-HVDC systems using dynamic phasors[J]. IEEE Transactions on Power Delivery, 2014, 29(4): 1989-1998.

[42] Gao B, Wang Y, Xu W. An improved model of voltage source converters for power system harmonic studies[J]. IEEE Transactions on Power Delivery, 2021, 37(4): 3051-3061.

[43] Lyu J, Zhang X, Cai X, et al. Harmonic state-space based small-signal impedance modeling of a modular multilevel converter with consideration of internal harmonic dynamics[J]. IEEE Transactions on Power Electronics, 2018, 34(3): 2134-2148.

[44] Beddard A, Sheridan C E, Barnes M, et al. Improved accuracy average value models of modular multilevel converters[J]. IEEE Transactions on Power Delivery, 2016, 31(5): 2260-2269.

[45] Beig A R, Asghar M S J. Performance evaluation and reliability of flexible asynchronous AC link and LCC-HVDC link under fault conditions[J]. IEEE Access, 2020, 8: 120562-120574.

[46] Rafferty J, Xu L, Morrow D J. DC fault analysis of VSC based multi-terminal HVDC systems[C]. Proc. IET Int. Conf. AC DC Power Transmiss., Birmingham, U.K., 2012: 1-6.

[47] Nian H, Kong L. Transient modeling and analysis of VSC based DC microgrid during short circuit fault[J]. IEEE Access, 2019, 7: 170604-170614.

[48] Davari M, Aghazadeh A, Gao W, et al. Detailed dynamic DC models of VSC considering controls for DC-fault simulations in modernized microgrid protection[J]. IEEE Journal of Emerging and Selected Topics in Power Electronics, 2020, 9(4): 4514-4532.

[49] Bahirat H J, Høidalen H K, Mork B A. Thévenin equivalent of voltage-source converters for DC fault studies[J]. IEEE Transactions on Power Delivery, 2015, 31(2): 503-512.

[50] Belda N A, Plet C A, Smeets R P P. Analysis of faults in multiterminal hvdc grid for definition of test requirements of hvdc circuit breakers[J]. IEEE Transactions on Power Delivery, 2018, 33(1): 403-411.

[51] Gao S, Ye H, Liu Y. Accurate and efficient estimation of short-circuit current for MTDC grids considering MMC control[J]. IEEE Transactions on Power Delivery, 2019, 35(3): 1541-1552.

[52] Ye H, Gao S, Li G, et al. Efficient estimation and characteristic analysis of short-circuit currents for MMC-MTDC grids[J]. IEEE Transactions on Industrial Electronics, 2021, 68(1): 258-269.

[53] Li Y, Cao R, Huang W, et al. Design and simulation for the control and protection of hybrid LCC-VSC MTDC system[C]. 2019 IEEE 3rd International Electrical and Energy Conference (CIEEC), Beijing, China, 2019: 281-286.

[54] Rao H, Zou C, Xu S, et al. The On-site Verification of Key Technologies for Kunbei-Liuzhou-Longmen Hybrid Multi-terminal Ultra HVDC Project[J]. CSEE Journal of Power and Energy Systems, 2022, 8(5): 1281-1289.

[55] Mao X, Wen Y, Wu L, et al. Simulation of LCC-MMC HVDC systems using dynamic phasors[J]. IEEE Access, 2021, 9: 122819-122828.

[56] Lee S Y, Son Y K, Cho H J, et al. Normalization of Capacitor-Discharge I2t by Short-Circuit Fault in VSC-Based DC System[J]. IEEE Transactions on Power Electronics, 2021, 37(1): 843-854.

[57] Xiang W, Yang S, Adam G P, et al. DC fault protection algorithms of MMC-HVDC grids: fault analysis, methodologies, experimental validations, and future trends[J]. IEEE Transactions on Power Electronics, 2021, 36(10): 11245-11264.

[58] Ma Y, Li H, Wang G, et al. Fault analysis and traveling-wave-based protection scheme for double-circuit LCC-HVDC transmission lines with shared towers[J]. IEEE Transactions on Power Delivery, 2018, 33(3): 1479-1488.

[59] Shuai Z, He D, Xiong Z, et al. Comparative study of short-circuit fault characteristics for VSC-based DC distribution networks with different distributed generators[J]. IEEE Journal of Emerging and Selected Topics in Power Electronics, 2018, 7(1): 528-540.

[60] Li B, Liao K, Yang J, et al. Transient fault analysis method for VSC-based DC distribution networks with multi-DGs[J]. IEEE Transactions on Industrial Informatics, 2022, 18(11): 7628-7638.

[61] Lacerda V A, Monaro R M, Campos-Gaona D, et al. An approximated analytical model for pole-to-ground faults in symmetrical monopole MMC-HVDC systems[J]. IEEE Journal of Emerging and

Selected Topics in Power Electronics, 2020, 9(6): 7009-7017.

[62] Daryabak M, Filizadeh S, Vandaei A B. Dynamic phasor modeling of LCC-HVDC systems: Unbalanced operation and commutation failure[J]. Canadian Journal of Electrical and Computer Engineering, 2019, 42(2): 121-131.

[63] Li C. Zhao J, Xu, Y, et al. A pole-to-pole short-circuit fault current calculation method for DC grids[J]. IEEE Transactions on Power Systems, 2017, 32(6): 4943-4953.

[64] Yu J, Zhang Z, Xu Z. Fault Current and Voltage Estimation Method in Symmetrical Monopolar MMC-based DC Grids[J]. Journal of Modern Power Systems and Clean Energy, 2021, 10(5): 1401-1412.

[65] Yu J, Zhang Z, Xu Z, et al. An equivalent calculation method for pole-to-ground fault transient characteristics of symmetrical monopolar MMC based DC grid[J]. IEEE Access, 2020, 8: 123952-123965.

[66] Langwasser M, Carne G D, Liserre M, et al. Fault current estimation in multi-terminal HVdc grids considering MMC control[J]. IEEE Transactions on Power Systems, 2019, 34(3): 2179-2189.

[67] van der Meer A A, Gibescu M, van der Meijden M A M M, et al. Advanced hybrid transient stability and EMT simulation for VSC-HVDC systems[J]. IEEE Transactions on Power Delivery, 2014, 30(3): 1057-1066.

[68] Zheng A, Guo C, Cui P, et al. Comparative study on small-signal stability of LCC-HVDC system with different control strategies at the inverter station[J]. IEEE Access, 2017, 7: 34946-34953.

[69] Wu G, Du Z, Li C, et al. VSC-MTDC operation adjustments for damping inter-area oscillations[J]. IEEE Transactions on Power Systems, 2018, 34(2): 1373-1382.

[70] Vennelaganti S G, Chaudhuri N R. Stability criterion for inertial and primary frequency droop control in MTDC grids with implications on ratio-based frequency support[J]. IEEE Transactions on Power Systems, 2020, 35(5): 3541-3551.

[71] Du W, Fu Q, Wang H. Small-signal stability of an AC/MTDC power system as affected by open-loop modal coupling between the VSCs[J]. IEEE Transactions on Power Systems 2017, 33(3): 3143-3152.

[72] Du W, Fu Q, Wang H. Open-loop modal coupling analysis for a multi-input multi-output interconnected MTDC/AC power system[J]. *IEEE Transactions on Power Systems*, 2018, 34(1): 246-256.

[73] Che, Y, Jia J, Zhu J, et al. Stability evaluation on the droop controller parameters of multi-terminal DC transmission systems using small-signal model[J]. IEEE Access, 2019, 7: 103948-103960.

[74] Yogarathinam A, Chaudhuri N R. Stability-constrained adaptive droop for power sharing in AC-MTDC grids[J]. IEEE Transactions on Power Systems, 2019, 34(3): 1955-1965.

[75] Wang W, Barnes M, Marjanovic O. Stability limitation and analytical evaluation of voltage droop controllers for VSC MTDC[J]. CSEE Journal of Power and Energy Systems, 2018, 4(2): 238-249.

[76] Wen B, Boroyevich D, Burgos R, et al. Analysis of D-Q small-signal impedance of grid-tied inverters[J]. IEEE Transactions on Power Electronics, 2016, 31(1): 675–687.

[77] Chaudhuri N R, Majumder R, Chaudhuri B, et al. Stability analysis of VSC MTDC grids connected to multimachine AC systems[J]. IEEE Transactions on Power Delivery, 2011, 26(4): 2774-2784.

[78] Beerten J, D'Arco S, Suul J A. Identification and small-signal analysis of interaction modes in VSC MTDC systems[J]. IEEE Transactions on Power Delivery, 2016, 31(2): 888-897.

[79] Li T, Gole A M, Zhao C. Harmonic instability in MMC-HVDC converters resulting from internal dynamics[J]. IEEE Transactions on Power Delivery, 2016, 31(4): 1738-1747.

[80] Dadjo Tavakoli S, Prieto-Araujo E, Sánchez-Sánchez E, et al. Interaction assessment and stability analysis of the MMC-based VSC-HVDC link[J]. Energies, 2020, 13(8): 1-19.

[81] Zou Y, Qin J, Zhang L, et al. Inequality constraints based method for fast estimation of droop slope stability regions for MMC-based MTDC systems[J]. *IEEE Transactions on Power Delivery*, 2020, 36(6): 3689-3700.

[82] Wang M, Chen Y, Dong, X, et al. Impedance modeling and stability analysis of DFIG wind farm with LCC-HVDC transmission[J]. *IEEE Journal on Emerging and Selected Topics in Circuits and Systems*, 2022, *12*(1): 7-19.

[83] Xu L, Fan L. Impedance-based resonance analysis in a VSC-HVDC systems[J]. IEEE Transactions on Power Delivery, 2013, 28(4): 2209-2216.

[84] Xu L, Fan L, Miao Z. DC impedance-model-based resonance analysis of a VSC-HVDC system[J]. IEEE Transactions on Power Delivery, 2015, 30(3): 1221-1230.

[85] Deng W, Pei W, Zhuang Y, et al. Interaction behavior and stability analysis of low-voltage multi-terminal DC system[J]. IEEE Transactions on Power Delivery, 2021, 37(5): 3555-3566.

[86] Stamatiou G, Bongiorno M. Stability analysis of two-terminal VSC-HVDC systems using the net-damping criterion[J]. IEEE Transactions on Power Delivery, 2016, 31(4): 1748-1756.

[87] Pinares G, Bongiorno M. Analysis and mitigation of instabilities originated from DC-side resonances in VSC-HVDC systems[J]. IEEE Transactions on Industry Applications, 2016, 52(4): 2807-2815.

[88] Roose T, Lekić A, Alam M M, et al. Stability analysis of high-frequency interactions between a converter and HVDC grid resonances[J]. IEEE Transactions on Power Delivery, 2021, 36(6): 3414-3425.

[89] Ji K, Tang G, Yang J, et al. Harmonic stability analysis of MMC-based DC system using DC impedance model[J]. IEEE Journal of Emerging and Selected Topics on Power Electronics, 2020, 8(2): 1152-1163.

[90] Zhang H, Wang X, Mehrabankhomartash M, et al. Harmonic stability assessment of multiterminal DC (MTDC) systems based on the hybrid AC/DC admittance model and determinant-based GNC[J]. IEEE Transactions on Power Electronics, 2021, 37(2): 1653-1665.

[91] Harnefors L, Yepes A G, Vidal A, et al. Passivity-based controller design of grid-connected VSCs for prevention of electrical resonance instability[J]. IEEE Transactions on Industrial Electronics, 2015, 62(2): 702-710.

[92] Pinares G, Bongiorno M. Modeling and analysis of VSC-based HVDC systems for DC network stability studies[J]. IEEE Transactions on Power Delivery, 2016, 31(2): 848-856.

[93] Guo L, Li P, Li X, et al. Reduced-order modeling and dynamic stability analysis of MTDC systems in DC voltage control timescale[J]. CSEE Journal of Power and Energy Systems, 2020, 6(3): 591-600.

[94] Fu Q, Du W, Wang H, et al. Small-signal stability analysis of a VSC-MTDC system for investigating DC voltage oscillation[J]. IEEE Transactions on Power Systems, 2021, 36(6), 5081-5091.

[95] Fu Q, Du W, Wang H, et al. Effect of the dynamics of the MTDC power system on DC voltage oscillation stability[J]. IEEE Transactions on Power Systems, 2022, 37(5): 3482-3494.

[96] Fu Q, Du W, Wang H F, et al. Analysis of small-signal power oscillations in MTDC power transmission system[J]. IEEE Transactions on Power Systems, 2020, 36(4): 3248-3259.

[97] Du W, Fu Q, Wang H. Damping torque analysis of DC voltage stability of an MTDC network for the wind power delivery[J]. IEEE Transactions on Power Delivery, 2019, 35(1): 324-338.

[98] Fu Q, Du W, Wang H, et al. Impact of the differences in VSC average model parameters on the DC voltage critical stability of an MTDC power system[J]. IEEE Transactions on Power Systems, 2023, 38(3): 2805-2819.

[99] Fu Q, Du W, Wang H, et al. DC voltage oscillation stability analysis of DC-voltage-droop-controlled multiterminal DC distribution system using reduced-order modal calculation[J]. IEEE Transactions on Smart Grid, 2022, 13(6): 4327-4339.

[100] Yazdani A, Iravani R. Voltage-sourced converters in power systems[M]. Hoboken, NJ, USA: John Wiley & Sons, 2010.

[101] Harnefors L, Bongiorno M, Lundberg S. Input-admittance calculation and shaping for controlled voltage-source converters[J]. IEEE Transactions on Industrial Electronics, 2007, 54(6): 3323-3334.

[102] Stamatiou G, Bongiorno M. Stability analysis of two-terminal VSC-HVDC systems using the net-damping criterion[J]. IEEE Transactions on Power Delivery, 2016, 31(4): 1748-1756.

[103] Xu Z. VSC-HVDC Transmission System[M]. Beijing, China: China Machine Press, 2013.

[104] Li J, Li Y, Zhang X, et al. Design-oriented DC-side stability analysis of VSC-HVDC systems based on dominant frequency analysis[J]. International Journal of Electrical Power & Energy Systems, 2023, 149(109060): 1-10.